where $\boldsymbol{\nu}$ is the surface normal in the reference configuration, u_j are the components of the displacement vector on base vectors in the reference configuration and $()_{,i}$ denotes covariant differentiation in the reference frame.

The matrix material is characterized as an elastic-viscoplastic isotropically hardening solid. The total rate of deformation, $\mathbf{D}$, is written as the sum of an elastic part, $\mathbf{D}^{\mathrm{e}}$, and a plastic part $\mathbf{D}^{\mathrm{p}}$, with

$$\mathbf{D}^{\mathrm{e}} = \frac{1+\nu}{E}\hat{\boldsymbol{\tau}} - \frac{\nu}{E}(\hat{\boldsymbol{\tau}} : \mathbf{I})\mathbf{I} \tag{3.4}$$

$$\mathbf{D}^{\mathrm{p}} = \frac{3\dot{\bar{\epsilon}}}{2\bar{\sigma}}\boldsymbol{\tau}' \tag{3.5}$$

where $\hat{\boldsymbol{\tau}}$ is the Jaumann rate of Kirchhoff stress, $\mathbf{I}$ is the identity tensor, $\hat{\boldsymbol{\tau}} : \mathbf{I}$ is the trace of $\hat{\boldsymbol{\tau}}$, $\dot{\bar{\epsilon}}$ is the effective plastic strain rate, E is Young's modulus, ν is Poisson's ratio and

$$\boldsymbol{\tau}' = \boldsymbol{\tau} - \frac{1}{3}(\boldsymbol{\tau} : \mathbf{I})\mathbf{I} \ , \ \bar{\sigma}^2 = \frac{3}{2}\boldsymbol{\tau}' : \boldsymbol{\tau}' \tag{3.6}$$

$$\dot{\bar{\epsilon}} = \dot{\epsilon}_0[\bar{\sigma}/g(\bar{\epsilon})]^{1/m} \ , \ g(\bar{\epsilon}) = \sigma_0(\bar{\epsilon}/\epsilon_0 + 1)^N \ , \ \epsilon_0 = \sigma_0/E \tag{3.7}$$

Here, $\bar{\epsilon} = \int \dot{\bar{\epsilon}} dt$ and the function $g(\bar{\epsilon})$ represents the effective stress versus effective strain response in a tensile test carried out at a strain-rate such that $\dot{\bar{\epsilon}} = \dot{\epsilon}_0$. Also, σ_0 is a reference strength and N and m are the strain hardening exponent and strain rate hardening exponent, respectively.

Senior et al. (1) studied void nucleation and growth in uniaxial tension specimens, using both normalized and tempered (N+T) specimens and specimens that were subsequently aged (N+T+A). The work hardening properties in these two cases differ somewhat; the 0.2% proof stress, the ultimate tensile stress, and the strain at the ultimate tensile stress for the N+T material are 637 MPa, 761 MPa and 0.083, respectively. Corresponding values for the N+T+A material are 630 MPa, 770 MPa, and 0.073. This small difference in work hardening behavior is not describable by the power law relation (3.7); for example, the higher ultimate tensile stress to 0.2% proof stress ratio for the N+T+A material implies a higher value of N in (3.7), while the lower strain to maximum load indicates a lower N value. In the calculations, the values $E = 210$ GPa, $\nu = 0.3$, $\sigma_0 = 630$ MPa, N=0.08, and $m = 0.01$ are used. In a

uniaxial tensile test with $\dot{\bar{\epsilon}} = \dot{\epsilon}_0$, these material parameters give an ultimate tensile stress of 758 MPa at a strain of 0.08.

As sketched in Fig. 2, we consider spherical particles of radius r_0 located along the axis of a circular cylinder with an initial spacing of $2b_0$ between particle centers. The cylinder has initial radius R_0 and attention is confined to axisymmetric deformations. Furthermore, the circular cylindrical cell surrounding each particle is required to remain a circular cylinder throughout the deformation history and within each cell symmetry is assumed about the cell center line so that only the shaded region is analyzed numerically. As discussed by Tvergaard (10), this axisymmetric configuration can be considered an approximation to a three dimensional array of hexagonal cylinders.

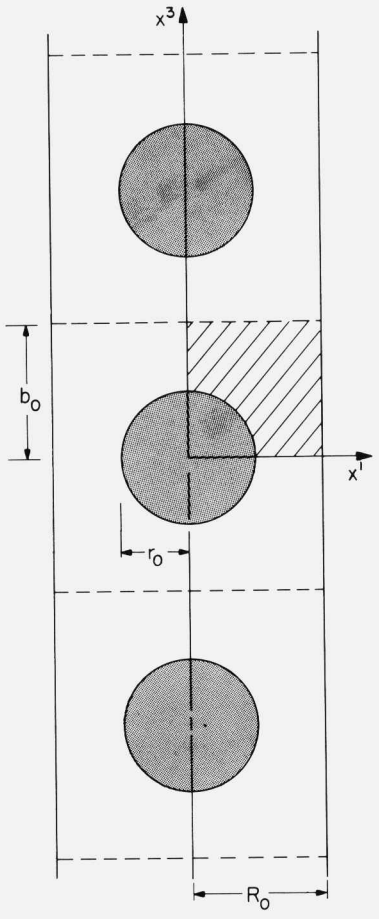

FIGURE 2. Axisymmetric model of a material containing an array of spherical rigid inclusions. Due to the assumed symmetry, only the shaded quadrant is analyzed numerically.

In a cylindrical coordinate system with radial coordinate x^1 and axial coordinate x^3, (the circumferential angle is the x^2-direction) the rate boundary conditions for the axisymmetric region analyzed numerically are

$$\dot{u}^3 = 0 \ , \ \dot{T}^1 = 0 \ , \ \dot{T}^2 = 0 \ , \ \text{on} \ \ x^3 = 0 \tag{3.8}$$

$$\dot{u}^3 = \dot{U}_3 = \dot{\epsilon}_{ave} b \ , \ \dot{T}^1 = 0 \ , \ \dot{T}^2 = 0 \ , \ \text{on} \ \ x^3 = b_0 \tag{3.9}$$

$$\dot{u}^1 = \dot{U}_1 \ , \ \dot{T}^3 = 0 \ , \ \dot{T}^2 = 0 \ , \ \text{on} \ \ x^1 = R_0 \tag{3.10}$$

where $(\dot{}) = \partial()/\partial t$, $\dot{\epsilon}_{ave}$ is a prescribed constant and $\dot{U}_1$ is determined by the analysis. With these boundary conditions, the deformed circular cylindrical cell has radius $R = R_0 + U_1$, and height $2b = 2b_0 + 2U_3$.

The lateral displacement rate, $\dot{U}_1$ is determined from the condition that the average macroscopic true stress increments acting on the cell satisfy

$$\dot{\Sigma}_1 = \rho \dot{\Sigma}_3 \tag{3.11}$$

with

$$\Sigma_1 = \frac{R_0 b_0}{Rb} \left\{ \frac{1}{b_0} \int_0^{b_0} [T^1]_{x^1 = R_0} dx^3 \right\} \tag{3.12}$$

$$\Sigma_3 = \frac{R_0^2}{R^2} \left\{ \frac{2}{R_0^2} \int_0^{R_0} [T^3]_{x^3 = b_0} x^1 dx^1 \right\} \tag{3.13}$$

The ratio ρ is taken to give a history of stress triaxiality representative of that in the neck of a tensile bar. Bridgman's (11) relation for the stress state at the center of a necked tensile bar takes the form $\Sigma_1 = \rho(\bar{\epsilon})\Sigma_3$. Becker (12) uses a relationship of this form, but derived from a numerical analysis of neck development. However, the implementation, Becker (12), leads to an incremental relation that differs somewhat from (3.11). Here, (3.11) is employed with ρ taken to be the following function of ϵ_{ave},

$$\rho = \begin{cases} 0 & \text{for } \epsilon_{ave} < N \\ 10(\epsilon_{ave} - N) & \text{for } \epsilon_{ave} \geq N \text{ and } \rho < 0.70 \\ 0.70 & \text{otherwise} \end{cases} \tag{3.14}$$

For the material properties used in this investigation, (3.14) gives a triaxiality history quite close to that given by Bridgman's (11) formulas, as shown in Fig. 3. For the axisymmetric configuration analyzed here, the effective stress, Σ_e, and the hydrostatic stress, Σ_h are given by

$$\Sigma_e = |\Sigma_3 - \Sigma_1| \ , \ \Sigma_h = \frac{1}{3}(\Sigma_3 + 2\Sigma_1) \tag{3.15}$$

and the triaxiality is Σ_h/Σ_e.

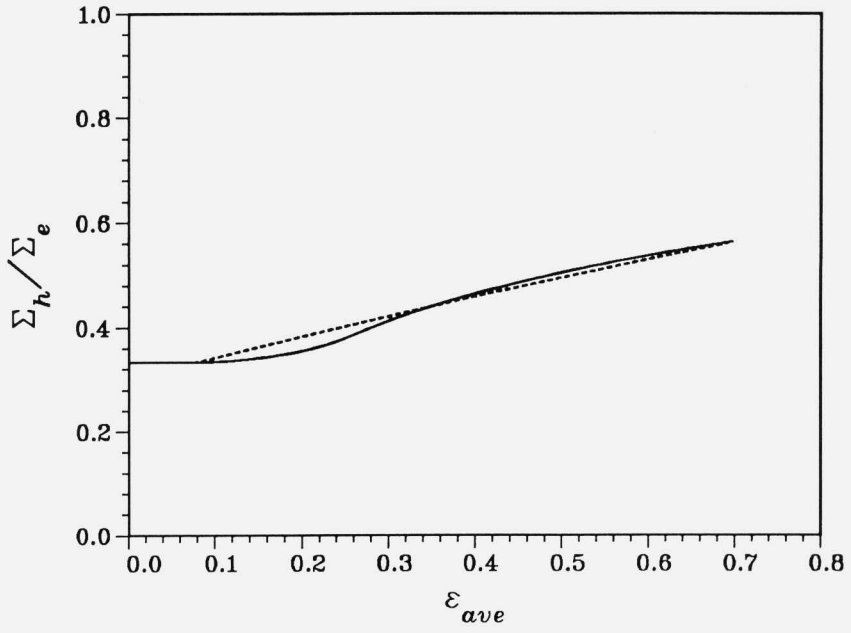

FIGURE 3. Stress triaxiality, Σ_h/Σ_e calculated from (3.11) for the material properties used here and with increasing normal traction across the interface. The dashed curve is the triaxiality history obtained from Bridgman's (11) formulas.

The triaxiality history in Fig. 3 based on (3.11) is representative of the stress state given by Bridgman's (11) formulas only while the normal traction across the interface is still increasing. When the normal traction is on the descending branch of the curve in Fig. 1, Σ_3 decreases and (3.11) overestimates the accompanying drop in triaxiality. Hence, (3.11) is not well suited for an investigation of the complete debonding process but, as Fig. 3 shows, is adequate for the initial debonding study carried out here.

The governing equations are solved using a finite element procedure described in (8). At each time step, the finite element stiffness matrix is formulated from an incremental principal of virtual work obtained by expanding (3.1). The deformation history is calculated in a linear incremental manner and, in order to increase the stable time step, the rate tangent modulus method of Peirce et al. (13) is used. This is a forward gradient method based on an estimate of the plastic strain rate in the interval between t and $t + \Delta t$. The incremental boundary value problem is solved using a combined finite element Rayleigh-Ritz method, Tvergaard (14). The finite element method is a displacement based finite-strain formulation that incorporates an additional contribution to the global stiffness matrix from the interface integral. Finite element meshes with 20 quadrilaterals around the inclusion and 17 in the radial direction and with 24 quadrilaterals around the inclusion and 12 in the radial direction were used; the former in calculations with $r_0/R_0 = 0.3$ and the latter with $r_0/R_0 = 0.6$. Each quadrilateral consists of four linear displacement "crossed" triangular elements. A more complete description of the numerical procedure as well as additional references are given in (8).

RESULTS

The numerical calculations illustrate effects of particle size and spacing and interface strength on void nucleation. The matrix material properties are as specified previously and the cell geometry is kept fixed with $b_0/R_0 = 1.0$. Furthermore, the interface shear stiffness ratio α is taken as $\alpha = 1.0$ in all cases. In (8), the value $\alpha = 10.0$ was mainly used, but numerical results in (8) showed little sensitivity to the value of α. The dimensionless groups varied are a particle spacing parameter, r_0/R_0, a particle size parameter, δ/r_0, and the ratio of interface strength to reference matrix flow strength σ_{max}/σ_0.

As discussed in (8), void nucleation is a process that occurs over a range of strain and the appropriate definition of a void nucleation strain depends on the context in which it is to be used. The focus here is in relation to the data of Senior et al. (1) where the fraction of particles with visible voids is reported. Hence, the strain at which debonding initiates along the particle-matrix interface is of interest. By way of contrast, in (8) the nucleation strain is defined in a manner that is appropriate for relating the results to Gurson's (15,16) constitutive relation for progressively cavitating solids. To emphasize that the quantity reported is the initial debonding strain, it is denoted by ϵ_{dbnd}. Computed results for the dependence of the initial debonding strain on interface strength, particle size and particle spacing are shown in Table I. As discussed in (8), for certain interface characterizations equilibrium solutions only exist if ϵ_{ave} decreases during decohesion. In Table I, such cases are marked with a superscript * and the maximum value of ϵ_{ave} is reported.

TABLE I

DEPENDENCE OF INITIAL DEBONDING STRAIN ON INTERFACE STRENGTH AND PARTICLE GEOMETRY

r_0/R_0	σ_{max}/σ_0	δ/r_0	ϵ_{dbnd}
0.3	2.4	0.00333	0.40*
0.3	2.4	0.01	0.44
0.3	2.4	0.03	0.49
0.6	2.4	0.01	0.21
0.3	3.0	0.01	0.75
0.6	3.0	0.01	0.42
0.6	3.6	0.01	0.52*

The entries marked by * correspond to local strain maxima for cases where equilibrium solutions for continued debonding have decreasing strain.

The particle spacing $r_0/R_0 = 0.3$ represents a volume fraction of 0.018. For the N+T and N+T+A materials Senior et al. (1) report precipitate volume fractions of 0.0149 and 0.0217, respectively. With $r_0/R_0 = 0.6$, the volume fraction is increased to 0.144. This high volume fraction is used here as a simple means of modelling the interaction effects that occur in a particle cluster. With $\sigma_0 = 630$ MPa, the values of $\sigma_{max}/\sigma_0 = 2.4$, 3.0 and 3.6 in Table I correspond to interfacial strengths of 1512 MPa, 1890 MPa and 2268 MPa, respectively. If r_0 is taken as 36×10^{-9} m, which is a value near the mean particle radii of 34×10^{-9} m for the N+T material and 40×10^{-9} m for the N+T+A material and, if the characteristic interface length δ is regarded as fixed at 36×10^{-11} m, then the three particle sizes in Table I are 12×10^{-9} m, 36×10^{-9} m and 108×10^{-9} m. The values of the work of separation, $\phi_{sep} = 9\sigma_{max}\delta/16$, corresponding to the three interfacial strengths are then 0.306 J/m^2, 0.383 J/m^2 and 0.459 J/m^2. In the following discussion, unless otherwise stated, δ will be regarded as fixed at 36×10^{-11} m, with r_0 and R_0 being varied to obtain the values of r_0/R_0 and δ/r_0 shown in Table I. Other interpretations can be made. For example, if, for the first three entries in Table I, the particle size is regarded as fixed at 36×10^{-9} m, the variations in δ/r_0 correspond to values of the work of separation, ϕ_{sep}, of 0.102 J/m^2, 0.306 J/m^2, and 0.918 J/m^2.

With δ regarded as fixed, the first three entries in Table I nearly span the range of carbide particle sizes in (1) and show a definite size effect, but the initial debonding strain, ϵ_{dbnd}, only varies between 0.40 and 0.49 as the particle size varies by nearly an order of magnitude. At fixed particle size and spacing,

there is a strong effect of interfacial strength on initial debonding strain. With $r_0/R_0 = 0.3$ increasing the interfacial strength by 25%, from 1512 MPa to 1890 MPa, increases the initial debonding strain from 0.44 to 0.75; similarly with $r_0/R_0 = 0.6$ the initial debonding strains are 0.21, 0.42 and 0.52, for the three interfacial strengths considered here. Particle spacing plays an important role in setting the debonding strain. Decreasing the particle spacing by a factor of two, decreases the initial debonding strain from 0.44 to 0.21 with an interface strength of 1512 MPa and from 0.75 to 0.42 with an interface strength of 1890 MPa.

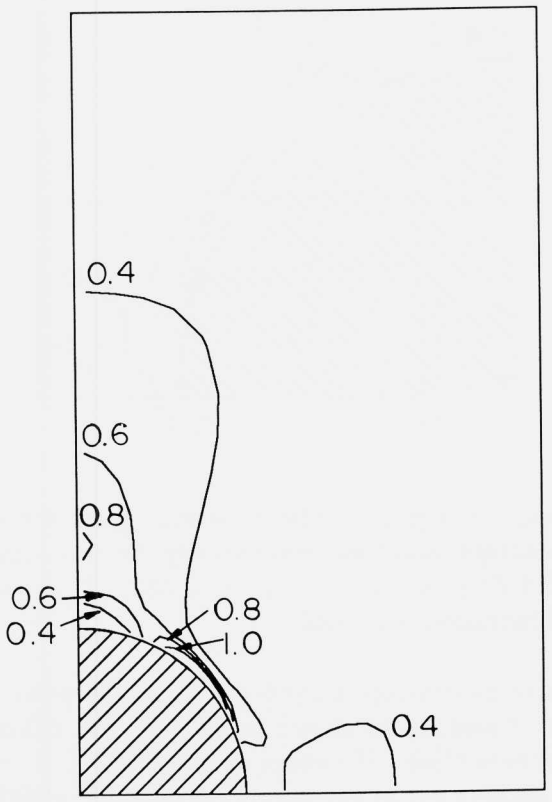

FIGURE 4. Contours of constant plastic strain, $\bar{\epsilon}$, in the deformed configuration of the quadrant analyzed numerically for the case $r_0/R_0 = 0.3$, $\sigma_{max}/\sigma_0 = 2.4$ and $\delta/r_0 = 0.01$ at $\epsilon_{ave} = 0.344$. The tension axis is vertical and the rigid inclusion is shaded.

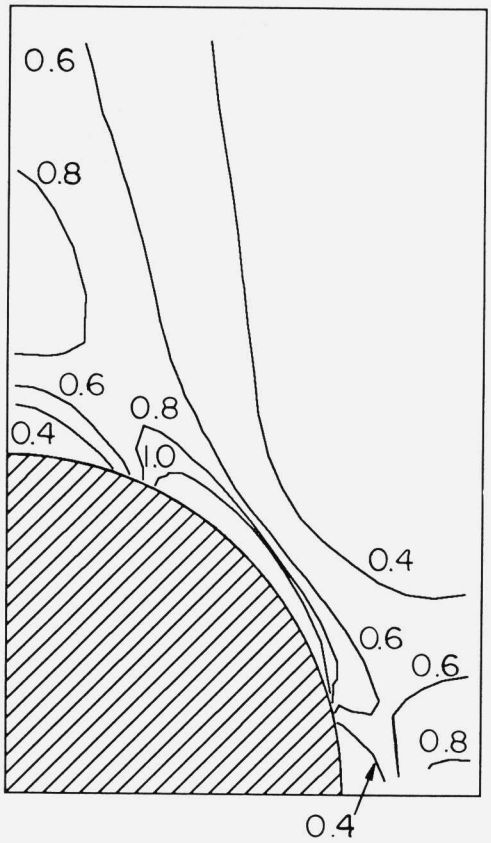

FIGURE 5. Contours of constant plastic strain, $\bar{\epsilon}$, in the deformed configuration of the quadrant analyzed numerically for the case $r_0/R_0 = 0.6$, $\sigma_{max}/\sigma_0 = 3.0$ and $\delta/r_0 = 0.01$ at $\epsilon_{ave} = 0.334$. The tension axis is vertical and the rigid inclusion is shaded.

Very large strains develop around the particles prior to debonding as illustrated in Figs. 4 and 5. As shown in Table I, the debonding strains for these two cases are very close. The stage of deformation shown in Figs. 4 and 5 is a bit prior to attainment of the maximum interfacial normal traction. In Fig. 4 $u_n/\delta = 0.26$ and in Fig. 5 $u_n/\delta = 0.23$. With $r_0/R_0 = 0.6$, Fig. 5, the region of high strain concentration occupies a greater part of the unit cell, but both figures exhibit the high strain concentration that develops at 45° from the tensile axis. The Mises effective stress, $\bar{\sigma}$, is highest where the strain concentration is highest, while the hydrostatic tension is highest near the axis of symmetry. The combined effect is that debonding begins near the end of the strain concentration closest to the axis of symmetry. However, typically,

as discussed in (8), the crack rapidly propagates to the axis of symmetry and a spherical cap void develops with the maximum normal displacement at the axis of symmetry.

The cases shown in Figs. 4 and 5 were each calculated using two meshes. For the case shown in Fig. 4, one mesh was the 20 x 17 element mesh used in all other calculations with $r_0/R_0 = 0.3$. The second mesh was a much cruder 12 x 11 element mesh. For the crude mesh calculation $\epsilon_{dbnd} = 0.42$ as compared with the finer mesh value of $\epsilon_{dbnd} = 0.44$. For the case shown in Fig. 5 where $r_0/R_0 = 0.6$, the two meshes were a 20 x 12 element mesh and a 24 x 12 mesh, but with the increased number of elements concentrated around the strain concentration to resolve it more accurately. In these calculations, the coarser mesh gives $\epsilon_{dbnd} = 0.44$ and the fine mesh gives $\epsilon_{dbnd} = 0.42$. The variation of ϵ_{dbnd} with increasing numbers of elements is not monotonic, as these two examples illustrate. This is not unexpected since, for example, the uniformity of the element distribution around the particle was changed with the change in number of elements. These results are merely meant to give some indication of the mesh dependence of the reported values of ϵ_{dbnd}. For each of these calculations, the values reported in Table I and the contours in Figs. 4 and 5 are based on the finer mesh.

DISCUSSION

Senior et al. (1) present results for the fraction of carbides nucleating voids as a function of plastic strain for normalized and tempered specimens (N+T) and specimens that were subsequently aged (N+T+A). For the N+T+A material 10% of the carbides have nucleated voids at an accumulated plastic strain of ≈ 0.45, while for the N+T material the 10% voided fraction is not reached until a plastic strain of ≈ 0.64. The 20% level is reached at strains of ≈ 0.6 and ≈ 0.8 for the N+T+A and N+T materials, respectively. For the N+T+A material the number fraction of carbides nucleating voids is 44% at the fracture strain of 0.88 and for the N+T material this number fraction reaches 56% at the fracture strain of 1.19. At a strain of 0.75, about 32% of the carbides have nucleated voids in the N+T+A material, while at this strain approximately 15% of the carbides have nucleated voids in the N+T material. This can be compared with the calculated nucleation strain of 0.75 in Table I, based on a uniform particle distribution, at 0.018 particle volume fraction, with an interface strength of 1890 MPa.

There are several factors that lead to preferential void nucleation at certain carbide particles. Senior et al. (1) state that precipitate nucleated voids formed exclusively at carbides on microstructural boundaries and that clusters of carbides at these locations were the sites at which nucleation occurred pref-

erentially. Preferential nucleation at clusters of carbides is consistent with the numerical results here which exhibit a large effect of particle spacing on the strain for initial debonding. The influence of microstructural boundaries has not been incorporated into the formulation, although this is possible in principle. In the present context, the significance of such boundaries most likely lies in the stress concentration they induce. In this regard, it is important to note that in the analyses here the matrix material is represented as an isotropic and isotropically hardening solid. For the particle sizes of interest, $\approx 10 \times 10^{-9}$ m to $\approx 100 \times 10^{-9}$ m, material anisotropy may be significant in determining the stress concentration around particles. Furthermore, at this size scale discrete dislocation effects, which are not accounted for in the model, may play a role.

Senior et al. (1) discuss the possibility that the difference in ductility between the N+T material and the N+T+A material may be due to particle size effects; the mean particle radius being 34×10^{-9} m for the N+T material and 40×10^{-9} m for the N+T+A material. The calculations carried out here indicate that the difference in particle size would not account for the observed difference in void nucleation characteristics.

Senior et al. (1) also estimate the interfacial strengths as 2050 MPa for the N+T material and as 1430 MPa for the N+T+A material. Since we obtain nucleation strains in the range 0.40 to 0.49 presuming a uniform distribution with an interface strength of 1512 MPa, it seems probable that the estimate for the interface strength given in (1) for the N+T+A material is too low. Assuming that the spacing $r_0/R_0 = 0.6$ corresponds to a rather highly concentrated cluster, that nucleates voids rather early, the results here suggest that an interface strength in the range between 1890 MPa and 2268 MPa is reasonable for the N+T material. This is consistent with the estimate in (1). Since the present results indicate that particle spacing plays an important role in setting the debonding strain, data on spacing at void nucleating carbides is needed to make a more quantitative comparison between model predictions and experiments.

The imposed history in the analyses does not involve a high degree of stress triaxiality, see Fig. 3. Bridgman's (11) formulas are known to underestimate somewhat the stress triaxiality in the neck of a tensile bar, see e.g. (17), but still the triaxiality that develops in the neck of a tensile specimen is significantly less severe than at a notch root or in front of a sharp crack. Data on void nucleation at carbides at various stress triaxialities representative of those in front of notches and sharp cracks, say Σ_h/Σ_e in the range between 1 and 3, could play an important role in quantifying the dependence of void nucleation on particle distribution and interface properties. Finally, it is noted that the focus in this investigation has been on initial debonding. However, calculations carried out within the framework used here can, as in (8), be

continued through complete debonding and subsequent void growth.

ACKNOWLEDGEMENTS

The support of the National Science Foundation (Solid Mechanics Program) through grant MSM-8618007 is gratefully acknowledged. The computations reported on here were carried out at the Pittsburgh Supercomputer Center. I am grateful to Dr. R. Becker of Alcoa and to Dr. G.B. Olson of MIT for helpful comments. I am also indebted to Dr. Olson for bringing reference (1) to my attention.

REFERENCES

1. B.A. Senior, F.W. Noble and B.L. Eyre, Acta Metall., 34, 1986, 1321-1327.

2. L.M. Brown and W.M. Stobbs, Phil. Mag., 23, 1971, 1201-1233.

3. A.S. Argon, J. Im and R. Safoglu, Met. Trans., 6A, 1975, 825-837.

4. Y.W. Chang and R.J. Asaro, Metal Science, 12, 1978, 277-284.

5. S.H. Goods and L.M. Brown, Acta. Metall., 27, 1979, 1-15.

6. J.R. Fisher and J. Gurland, Metal Science, 15, 1981, 193-202.

7. J.W. Hutchinson and V. Tvergaard, Harvard University Report Mech-99, June 1987.

8. A. Needleman, J. Appl. Mech., in press.

9. S.R. Nutt and A. Needleman, Scripta Metall., 21, 1987, 705-710.

10. V. Tvergaard, Int. J. Fract., 18, 1982, 237-252.

11. P.W. Bridgman, Studies in Large Plastic Flow and Fracture, McGraw-Hill, New York, 1952.

12. R. Becker, J. Mech. Phys. Solids, in press.

13. D. Peirce, C.F. Shih and A. Needleman, Comp. Struct., 18, 1984 875-887.

14. V. Tvergaard, J. Mech. Phys. Solids, 24, 1976, 291-304.

15. A.L. Gurson, Plastic Flow and Fracture Behavior of Ductile Materials Incorporating Void Nucleation, Growth and Interaction, Ph.D Thesis, Brown University, 1975.

16. A.L. Gurson, J. Engr. Mat. Tech., 99, 1977, 2-15.

17. A. Needleman, J. Mech. Phys. Solids, 20, 1972, 111-120.

EFFECT OF PARTICLE-VOID INTERACTION ON VOID GROWTH IN TENSION AND SHEAR

JOHN W. HUTCHINSON[1], VIGGO TVERGAARD[2]
(1) Division of Applied Sciences, Harvard University, Cambridge, MA. 02138; (2) Department of Solid Mechanics, Technical University of Denmark, Lyngby, Denmark.

INTRODUCTION

Most results on void growth in plastically deforming solids assume that the particle from which a void is nucleated does not interfere with the subsequent growth of the void even when the void shrinks in size in one or more directions. In effect it has been assumed either that the void exists from the start of straining with no particle present or that the particle mysteriously dissolves once nucleation occurs. Here we present two sets of results taken from work in progress which give some indication of the effect of the particle when it interacts with the void. First we present results for the initial growth of a void nucleated from a spherical particle in an elastic-perfectly plastic solid undergoing axisymmetric straining in the presence of hydrostatic tension or pressure. When the ratio of the mean stress to the tensile flow stress is less than about 0.6, the void remains in partial contact with the particle and has a volume rate of increase which is substantially greater than an unconstrained void. The second set of results are for a void nucleated at a spherical particle in a linearly viscous solid when the remote deformation is one of simple shear. Interaction between the particle and void is modeled in an approximate way and deformation of the void to large shear strains is tracked. The interaction significantly affects the growth of the void and its contribution to void softening.

SPHERICAL VOID IN AN ELASTIC-PERFECTLY PLASTIC SOLID UNDER AXISYMMETRIC STRAINING

Consider a spherical void of volume V in an infinite elastic-perfectly plastic solid with tensile flow stress σ_o and with a Mises yield

surface. The stresses remote to the void are axisymmetric with

$$\sigma_{11} = \sigma_{22} = T \quad \text{and} \quad \sigma_{33} = S \tag{1}$$

with S > T such that remote yielding requires S-T = σ_o. Denote the remote axisymmetric strain rates by

$$\dot{\varepsilon}_{11} = \dot{\varepsilon}_{22} = -\frac{1}{2}\dot{\varepsilon} \quad \text{and} \quad \dot{\varepsilon}_{33} = \dot{\varepsilon} \tag{2}$$

where $\dot{\varepsilon} > 0$ when S > T.

The normalized dilatation rate of the void, $\dot{V}/(\dot{\varepsilon}V)$, as a function of the stress triaxiality was determined by Rice and Tracey (1) under the assumption that the void is unconstrained. Further studies of the same problem were included in the work of Budiansky et al. (2). The lower of the two curves in Fig. 1 gives the normalized dilatation rate of the unconstrained void as a function of the triaxiality ratio

$$\sigma_m/\sigma_o = (S + 2T)/(3\sigma_o) \tag{3}$$

for T in the range $-\infty < T < S$. The dilatation rate $\dot{V}$ is negative ($\dot{\varepsilon}$ is always positive in this range) for σ_m/σ_o below about -0.05.

For σ_m/σ_o below about 0.6 the equatorial radius of the unconstrained void shrinks as it deforms. Thus, if the void has been nucleated by debonding at a spherical particle it will maintain contact with the particle in the vicinity of the particle's equator. To model the interaction of the particle with the deforming void we have used the same computational procedure as in references (1) and (2), but we have constrained the radial

velocity of material elements at the equator of the void to be nonnegative. Thus, for σ_m/σ_o below about 0.6 the particle props open the particle such that it maintains a constant equatorial radius. The resulting normalized dilatation rate for the constrained void is shown as the upper curve in Fig. 1. The dilatation rate is significant even when $\sigma_m = 0$ and it does not become zero until $\sigma_m/\sigma_o \cong -0.6$.

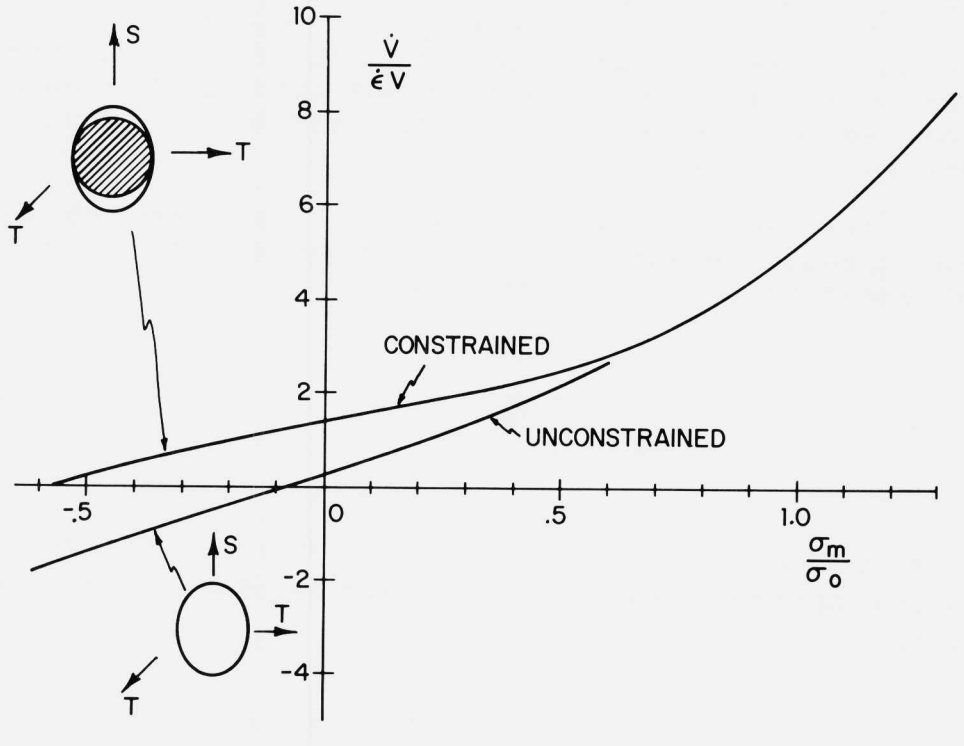

FIGURE 1. Normalized dilatation rate for a spherical void with and without particle interaction.

EVOLUTION OF AN INITIALLY SPHERICAL VOID IN A LINEARLY VISCOUS SOLID UNDER SIMPLE SHEAR WITH AND WITHOUT PARTICLE CONSTRAINT

The interaction between particle and void in axisymmetric straining when the mean stress σ_m is zero is expected to be somewhat similar to that in simple shear. The shear problem is inherently 3-dimensional and the plasticity problem analogous to that described above has not been analyzed. The behavior of an initially spherical void in simple shear in a linearly viscous solid can be analyzed exactly using Eshelby's solution, and a selection of such results was given by Fleck and Hutchinson (3). It is possible to modify the procedure in (3) so as to approximate the interaction between the particle and the void. Such a modification has been carried out (work in progress) and a few results are shown below.

The infinite matrix material is taken to be incompressible with the relation betwen deviatoric strain-rate and stress given by

$$\dot{\varepsilon}_{ij} = \frac{1}{2\mu} s_{ij} \quad . \tag{4}$$

The remote state is one of simple shear with superimposed hydrostatic stress σ_m such that far from the void

$$\begin{aligned} &\sigma_{11} = \sigma_{22} = \sigma_{33} \equiv \sigma_m \ , \quad \sigma_{12} \equiv \tau \\ &v_1 = \dot{\gamma} x_2 \ , \quad v_2 = v_3 = 0 \\ &\dot{\varepsilon}_{12} = \frac{1}{2}\dot{\gamma} \ , \quad \dot{\omega}_{12} = \frac{1}{2}\dot{\gamma} \end{aligned} \tag{5}$$

The remote shear strain γ is defined by the above expression. In each example reported here the void

is imagined to be nucleated at $\gamma = 0$ as a sphere with initial principal axes $a_o = b_o = c_o$.

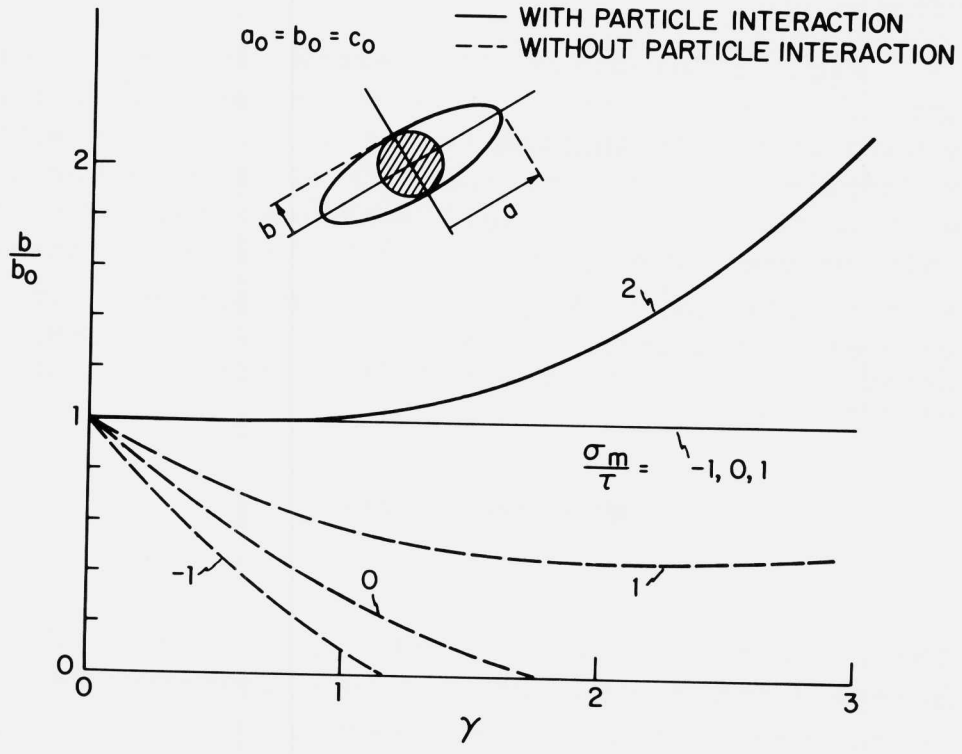

FIGURE 2. Evolution of the minor axis of the void in simple shear with and without particle interaction at four levels of remote triaxiality.

When particle interaction is absent or neglected, the void evolves through a sequence of ellipsoid shapes with major and minor axes a and b in the x_1, x_2 plane (see insert in Fig. 2) and axis c in the x_3 direction -- see reference (3) for full details. The evolution of the minor axis, b, is shown in Fig. 2 for four levels of σ_m/τ. When $\sigma_m = 0$, the void closes (i.e. $b \rightarrow 0$) at a shear strain $\gamma = 1.76$. For σ_m/τ greater than 0.44 the void remains open.

Fig. 3 displays the extra increment of straining per increment of remote strain, $\Delta\dot{\gamma}/\dot{\gamma}$, for a void with unit <u>initial</u> volume as it evolves with γ compared to the same infinite block of material with a fully bonded rigid spherical particle of unit volume. The quantity $\Delta\dot{\gamma}$ is the extra shear strain rate ($\Delta\dot{\gamma} = 2\Delta\dot{\varepsilon}_{12}$) due to the presence of a void of unit initial volume minus the corresponding quantity for a rigid spherical particle of unit volume, i.e.

$$\Delta\dot{\gamma} = (\Delta\dot{\gamma})_{\text{void}} - (\Delta\dot{\gamma})_{\text{particle}} \quad . \tag{6}$$

Thus, a block of material subject to overall shear stress τ and containing a dilute distribution of voids with initial volume fraction ρ will have an overall shear strain rate $\rho\Delta\dot{\gamma}$ over and above the same block containing a volume fraction ρ of bonded rigid spherical particles. Note that in the case $\sigma_m = 0$ the unconstrained void continues to make **essentially the** same extra strain rate contribution $\Delta\dot{\gamma}$ even though it closes up to an ellipsoidal crack as $\gamma \rightarrow 1.76$. (It is important to remember that the results in Fig. 3 are based on a void with unit <u>initial</u> volume not unit current volume.)

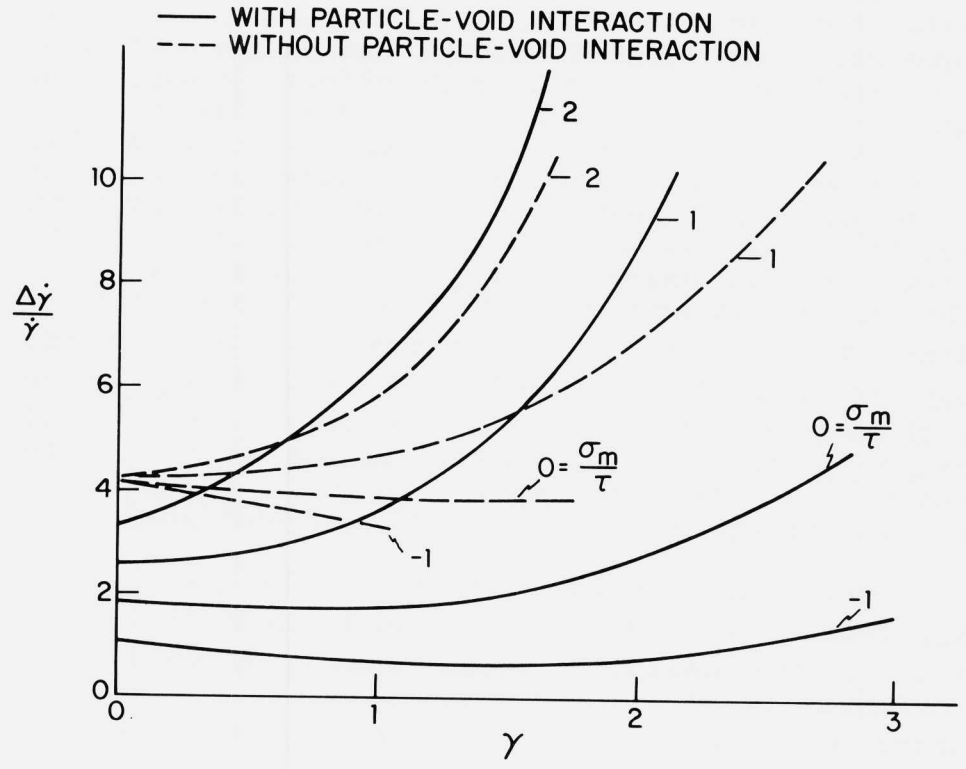

FIGURE 3. Extra increment of shear strain per increment of remote shear strain for a void with initial unit volume relative to a bonded rigid particle of unit volume. Results for constrained and unconstrained voids are shown.

The particle constrains the deformation of the void when one or more of the principal axes of the unconstrained void diminishes below the radius of the particle. The constraining effect is modeled by applying a uniform traction in the direction, or directions, of the principal axis over the surface of the void and by choosing this traction component to enforce the condition (incrementally) that the length of the axis not diminish below that of the particle. For example, if the principal axis b of the unconstrained void in the x_2' direction is diminishing, then a uniform traction derived from σ_{22}' is applied to the void surface with σ_{22}' chosen such that $\dot{b} = 0$. Enforcing the constraint in this manner permits the Eshelby solution to be applied exactly to the model since the void continues to evolve through a sequence of ellipsoidal shapes.

The constraining effect of the particle is significant when $\sigma_m/\tau \leq 1$ as can be seen in Figs. 2 and 3. The particle props open the void which obviously affects the evolution of its volume. Just after nucleation, when γ is small, the constraint reduces the strain rate contribution due to the void, $\Delta\dot{\gamma}$, relative to that of the unconstrained void. However, the constraining effect of the particle tends to enhance the strain rate contribution from the void as γ increases such that the contribution from the constrained void can actually exceed that from the unconstrained void. For example when the mean stress is zero, the contribution to the strain rate due to the void slowly increases as a function of γ as a result of its interaction with the particle. This suggests particle interaction is a possible mechanism for strain softening in shear in the absence of additional void nucleation, although the effect does not appear to be very strong.

ACKNOWLEDGEMENT

The work of J.W. Hutchinson was supported in part by the Materials Research Laboratory under Grant NSF-DMR-83-16979, by Grant NSF-MSM-84-16392, and by the Division of Applied Sciences, Harvard University. The work of V. Tvergaard was supported by the Danish Technical Research Center through Grant 16-4006M.

REFERENCES

1. J.R. Rice and D.M. Tracey. On the ductile enlargement of voids in triaxial stress fields. J. Mechanics and Physics of Solids, Vol. 17, 1969, pp. 201-217.

2. B. Budiansky, J.W. Hutchinson and S. Slutsky. Void growth and collapse in viscous solids. in Mechanics of Solids, Eds. H.G. Hopkins and M.J. Sewell, Pergamon Press, 1982, pp. 13-45.

3. N.A. Fleck and J.W. Hutchinson. Void growth in shear. Proc. Roy. Soc. Lond. A407, 1986, pp. 435-458.

MICROVOID FORMATION DURING SHEAR DEFORMATION OF ULTRAHIGH STRENGTH STEELS

J. G. COWIE*, M. AZRIN
U. S. Army Materials Technology Laboratory
Watertown, Massachusetts 02172

and G. B. OLSON
Massachusetts Institute of Technology
Cambridge, Massachusetts 02139

INTRODUCTION

The phenomenon of plastic shear instability and flow localization is of considerable interest due to its important role in fracture processes in many high-strength steels, especially in the ultrahigh-strength (UHS) range. It is also of special concern in Army applications of these steels because of its role as a principal failure mode in ballistic penetration. The latter case has been traditionally modelled as a continuum plastic instability arising from the thermal softening associated with deformation under adiabatic conditions. Models based on isothermally derived empirical constitutive relations have been used to account for strain localization conditions observed in high strain rate shear tests, but recent experiments have cast doubt on the validity of this approach [1]. We here report further results of shear tests conducted under both quasistatic and dynamic conditions, aimed at elucidating the fundamental mechanisms of shear localization underlying both fracture and ballistic penetration processes.

BACKGROUND

The phenomenon of deformation localization as it occurs in ballistic penetration is illustrated in Figure 1 [2], showing the localized deformation mode of failure, commonly referred to as adiabatic shear. The plastic flow after the onset of shear instability is concentrated in thin shear bands which appear white after metallographic etching. The through-thickness localized flow produces a "shear plugging" failure mode in which the material ahead of the projectile is ejected as a solid piece absorbing relatively little associated energy.

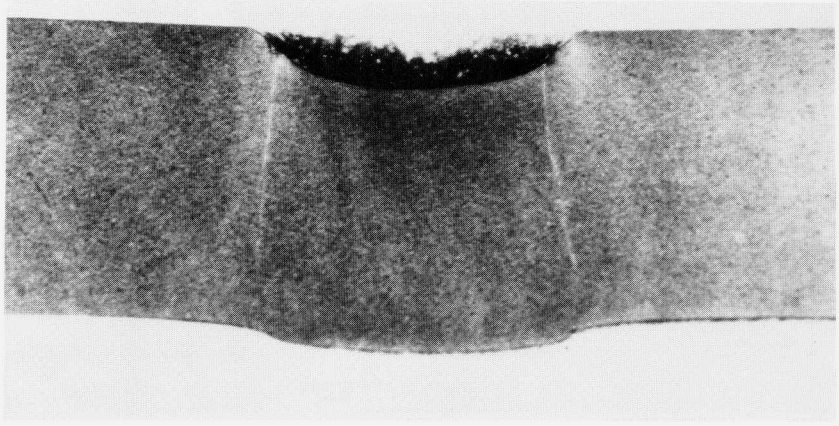

Figure 1. Photomicrograph of a 4340 steel Rc 52 plate (5.6 mm thick) that underwent a localized deformation mode of failure during ballistic impact. Note the white etched shear bands beneath the area of impact.

Much has been written over the past forty years on the subject of shear localization. In a recent review Cowie and Tuler [3] describe the various modeling approaches; flow softening, deformation heating, textural softening, and void nucleation softening. The review also describes the relationship between shear instability and fracture toughness. The reviews of Rogers [4,5] and Bedford et al. [6] give an excellent overview of the general phenomenon including the microstuctures resulting from localized flow. The continuum plasticity theory of adiabatic flow localization is treated by Clifton [7], and a general survey of strain localization is given by Argon [8]. A concise treatment of the specific role of adiabatic shear in armaments and ballistics can be found in the review of Samuels and Lamborn [9]. Olson et al.[10] endeavored to computer model the ballistic penetration of high strength steel using experimentally derived constitutive flow relations, but met with limited success. The authors proposed that the material exhibited a pressure dependence that the conventional thermal softening models could not describe. Experiments were designed to determine how the pressure dependence affects the deformation of UHS steels. More recent research by Azrin et al.[1] showed that the critical strain for shear localization in high strength 4340 steel is nearly identical for both isothermal (quasistatic) and adiabatic (dynamic) loading conditions. While thermal softening undoubtedly provides a contribution to the measured

stress-strain relations, this result of nearly identical instability strains and shear localization behavior in UHS steels at both high and low strain rates indicated that another flow softening phenomenon was equally important. As was reviewed in Ref. 10, observations that the instability strain is strongly influenced by the hydrostatic component of stress, together with metallographic evidence of microvoid nucleation, indicate that fracture related processes can also contribute to the strain softening effects underlying plastic shear localization [11-13]. Such phenomena must also be taken into account for a complete understanding of shear localization and shear banding.

The present study was initiated to obtain experimental evidence of microvoid nucleation preceding localized deformation during simple shear of UHS steels. Experiments were also devised to study both the effect of hydrostatic pressure and austenitizing temperature on the critical strain to localization. Two different simple shear specimen geometries were compared. Because of its influence on fracture related processes of potential importance to shear instability, the role of melt practice was also examined. Stress - strain data and corresponding strain profiles were obtained from each test in order to quantify the flow behavior in addition to accurately determining the instability strain.

MATERIALS AND METHODS

Two specimen geometries, thin wall torsion and double linear shear configurations, were tested under both adiabatic and isothermal conditions. Dynamic torsion tests were performed on a torsional impact apparatus incorporating a flywheel. Torque to the specimen is applied by a steel bar pneumatically engaged to lugs on the rotating flywheel. Flywheel rotational frequency is monitored by a velocimeter, while applied torque is measured by a strain gauge load cell adjacent to the specimen. Wooden dowels were inserted into the specimen to minimize buckling. These dynamic tests were performed at an imposed strain rate of 10^{2} per second to ensure essentially adiabatic deformation conditions in the specimens. Isothermal torsion tests were run on an MTS servo-hydraulic test machine at a strain rate of 10^{-3} per second. Results from the thin wall torsion experiments were reported previously [1].

Double linear shear specimens were also tested under both quasistatic and dynamic conditions. These specimens, shown schematically in Figure 2, have two narrow gauge sections which are displaced simultaneously in simple shear. Dynamic tests were performed in a modified instrumented Charpy impact machine. The Charpy specimen fixture was replaced with one that rigidly holds the ends of the double linear shear specimen. In addition, the pendulum weight was increased by sixty percent. The shear fixture may also apply up to 2250 N normal compressive load to the specimen's end while the specimen is being sheared. The load-time curve generated by the strain gauge instrumented tup is recorded and stored in the memory of a Nicolet high speed digital oscilloscope. These dynamic tests were performed at an imposed strain rate in excess of 10^{4} per second. Quasistatic double linear shear tests were run on a Tinius Olsen hydraulic tension/compression test machine at a strain rate of 10^{-3} per second.

Typical shear stress - shear strain curves generated from these tests are presented in Figures 3 and 4. These represent a rare earth modified (REM) 4130 steel, austenitized at 840°C and tempered 1 hour at 535°C and 200°C to give hardnesses of Rc 33 and 48 respectively.

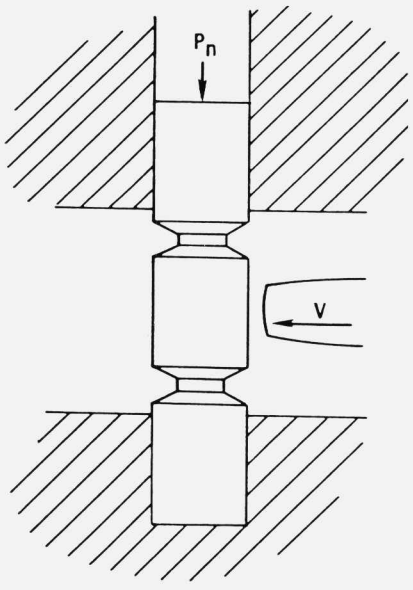

Figure 2. Schematic view of a double linear shear specimen. The specimen is sheared at a preselected speed (V) while an axial load (P_n) is superimposed on one end.

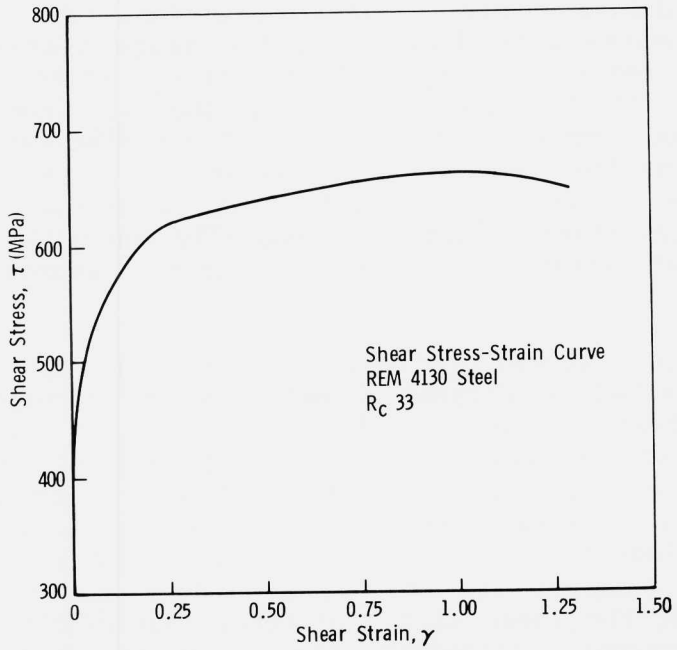

Figure 3. Plastic Shear stress-strain curve obtained from a quasistatic linear shear test of REM 4130 steel at Rc 33 (535°C temper). Shear strain at maximum stress is 110 percent.

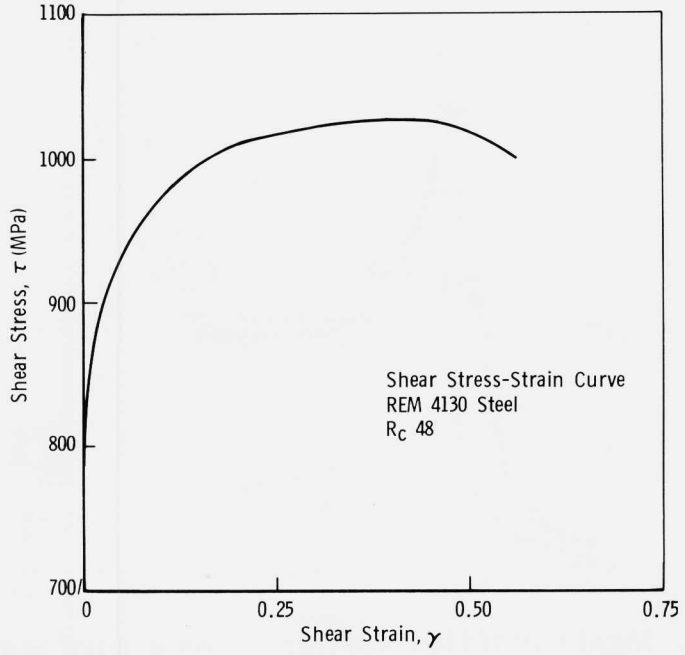

Figure 4. Plastic shear stress-strain curve obtained from a quasistatic linear shear test of REM 4130 steel at Rc 48 (200°C temper). Shear strain at maximum stress is 45 percent.

To determine precise strain profiles, four longitudinal scribe marks were drawn onto the gauge section of each specimen before testing. After testing, shear strain as a function of the position along the specimen axis was determined from the local angle of the scribe marks relative to the specimen centerline as measured in a Leitz universal measuring microscope. Dynamic tests were run to failure, while quasistatic tests were generally run until sufficient flow localization to produce a load drop of approximately ten percent.

Typical strain profiles obtained from isothermal tests are presented in Figures 5 and 6 which correspond to the stress-strain curves in Figures 3 and 4 respectively. Intense strain localization is found adjacent to the gauge section walls. This is consistent with both a computer simulation of simple shear of a rectangular body [10] and a finite element stress analysis of the double linear shear specimen geometry and loading by Tracey and Perrone [14]. Note that the shear strain plateaus (henceforth defined as the macroscopic instability strain) on the strain profiles correspond with the shear strains at peak stress on their

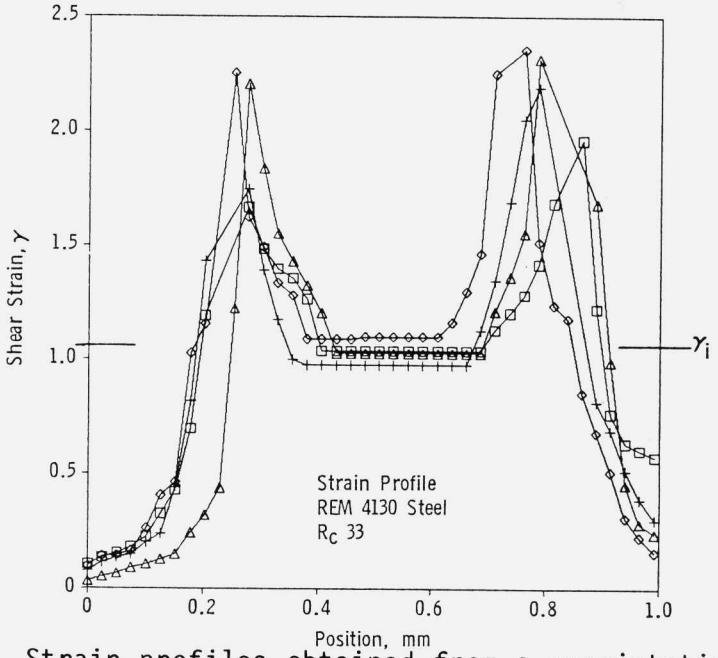

Figure 5. Strain profiles obtained from a quasistatic linear shear test of REM 4130 steel at Rc 33 (535°C temper). The mean plateau strain, defined as the macroscopic instability strain, is 110 percent.

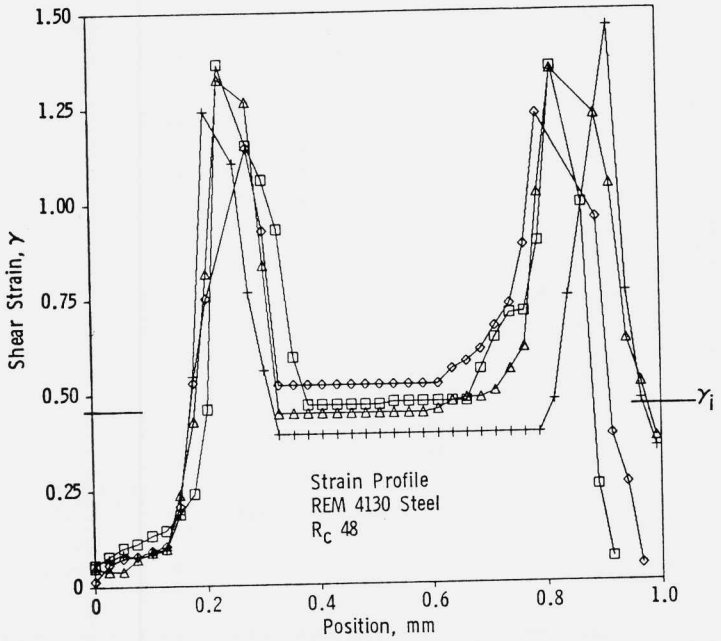

Figure 6. Strain profiles obtained from a quasistatic linear shear test of REM 4130 steel at Rc 48 (200°C temper). The mean plateau strain, defined as the macroscopic instability strain, is 45 percent.

corresponding stress-strain curves. Comparison of the instability strain data for both torsion and linear-shear test specimen geometries (Figures 7 and 8), confirms that the two configurations give nearly identical results.

RESULTS

Effect of Melting Practice

Because of its influence on fracture related processes of potential importance to shear localization, the role of melt practice was also examined. Three commercial heats of 4340 steel processed by air melt (AM), electroslag remelt (ESR), and vacuum arc remelt (VAR) practices were evaluated. The shear specimens were machined from heat treated blanks austenitized at 840°C and tempered 1 hour at 650°C, 535°C, 335°C, and 160°C to give hardness levels of Rc 30, 40, 48, and 56 respectively. Dynamic and quasistatic tests revealed no significant effect of melting practice with one exception. Under isothermal conditions, the air melted material tempered

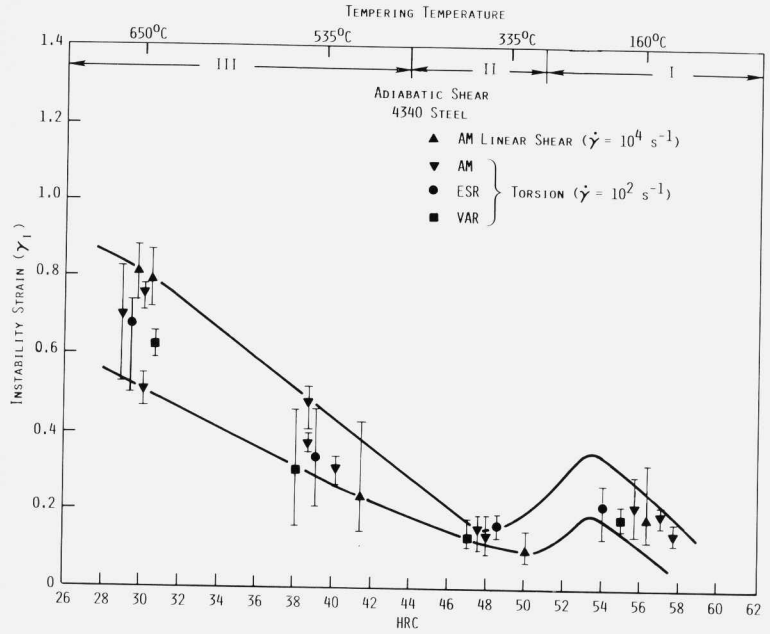

Figure 7. Comparison of instability strains measured in dynamic torsion and linear shear tests of AM, ESR, and VAR 4340 steel.

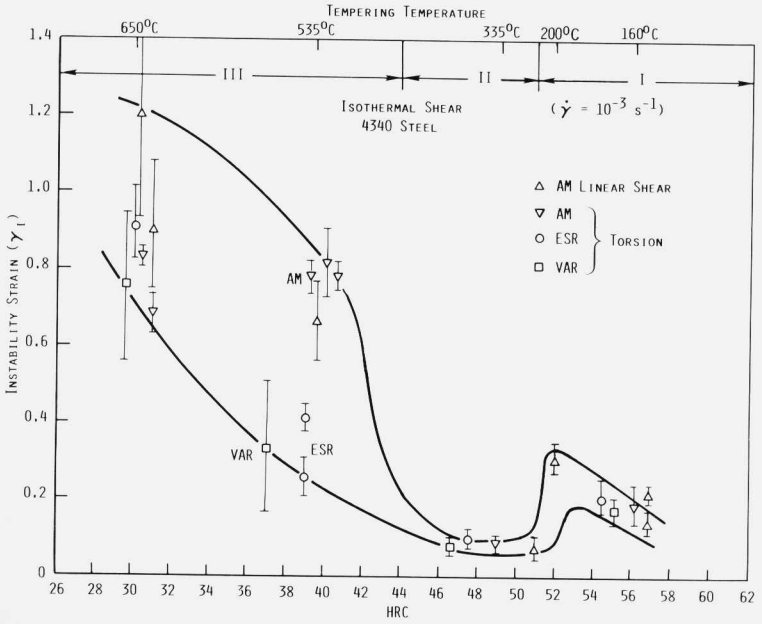

Figure 8. Comparison of instability strains measured in quasistatic torsion and linear shear tests of AM, ESR, and VAR 4340 steel.

at 535°C (Stage III temper) proved consistantly to have a higher instability strain than its VAR and ESR counterparts. Structurally, the only observable difference was the slightly smaller prior austenite grain size for the AM material. The structure of the 4340 steel given this tempering treatment consists of cementite needles running along the martensite laths. It is possible that the shear localization resistance is influenced by the length of void-nucleating cemetite paricles which in turn scales with the martensite packet and prior austenite grain sizes.

Effect of Strain Rate

Plotting all the instability strain data for both adiabatic (Figure 7) and isothermal (Figure 8) test conditions together (Figure 9), we observe little effect of strain rate on the instability strain, particularly at the higher strength levels. The linear shear tests spanned seven orders of magnitude in strain rate from isothermal to adiabatic test conditions. The resulting instability strains for the highest strength material (Rc 56) were nearly identical (Figures 9 and 10). The flow stress increased

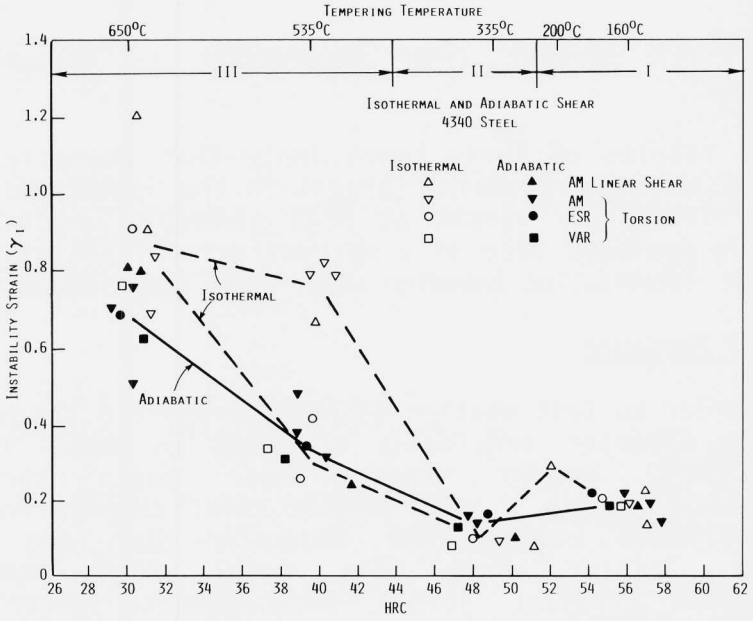

Figure 9. Comparison of instability strains measured in both dynamic and quasistatic shear tests of AM, ESR, and VAR 4340 steel.

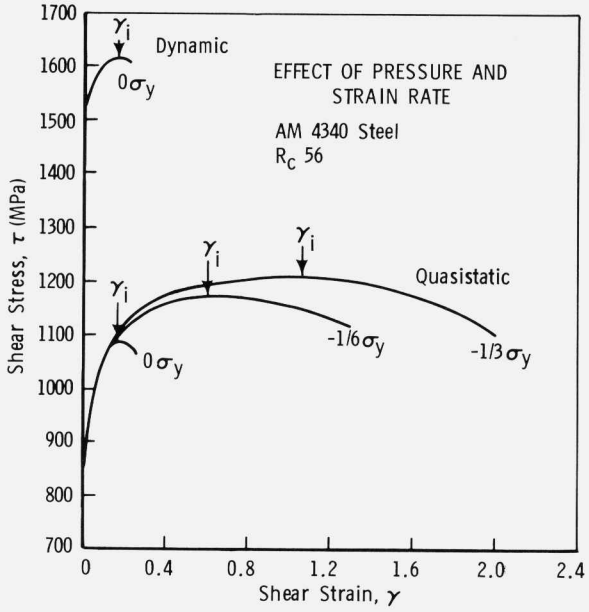

Figure 10. Plastic shear stress-strain curves obtained from both dynamic and quasistatic linear shear tests of an AM 4340 steel at Rc 56, with three different imposed axial compressive stresses: 0, 1/6, and 1/3 the yield strength.

nearly fifty percent from quasistatic to dynamic test conditions.

The results of these tests imply that there is little effect of thermal softening (absent in the isothermal tests) on the instability strain at high strength levels. This implies a dominant role of a microstructural instability in the shear localization behavior under pure shear conditions.

Effect of Pressure

In order to test whether UHS steels exhibit the pressure dependent behavior previously observed in lower strength steels [10], double linear shear tests were run quasistatically with a superimposed axial compressive load. Finite element calculations indicate that the stress component arising from this axial load reasonably approximates uniaxial stress once plastic shearing is underway. Axial compressive stresses of 1/6 and 1/3 the material's tensile yield stress were used. The stress - strain results quite clearly show pressure dependent behavior (Figures 10 and 11). As the axial stress is increased from 0

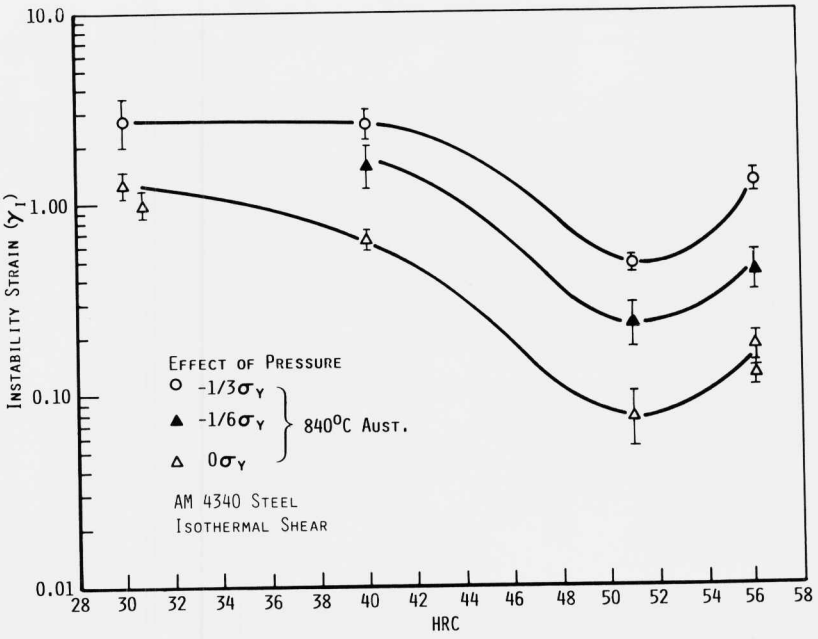

Figure 11. Comparison of instability strains of an AM 4340 steel with three different imposed axial compressive stresses: 0, 1/6, and 1/3 the tensile yield strength.

to 1/3 of the yield stress, the instability strain is increased quite substantially for all four hardness levels investigated.

The microstructure of the highest strength (Stage I tempered) material consists of a martensitic lath matrix with a fine epsilon carbide dispersion. In addition, there are submicron sized second phase particles which act as grain refiners (Figure 12). These second phases (undissolved during austenitizing) have been identified by Gore [15] to be primarilly alloy (Fe,Cr,Mo) carbides of the type $M_{23}C_6$ with a mean diameter of 171 nm and a volume fraction of 0.44 percent when austenitized at 870°C. The carbides, with an interparticle mean free path of 670 nm, are expected to interact during plastic deformation [16] leading to cooperative microvoid nucleation. Figure 13 presents a TEM photomicrograph of sheared material showing a pair of carbides linked by microvoids. The photograph has been deliberately overdeveloped to clearly show the voids, and a schematic representation is also shown for clarity. This thin foil specimen was removed from the gauge section of a linear shear specimen which was strained to instability. The

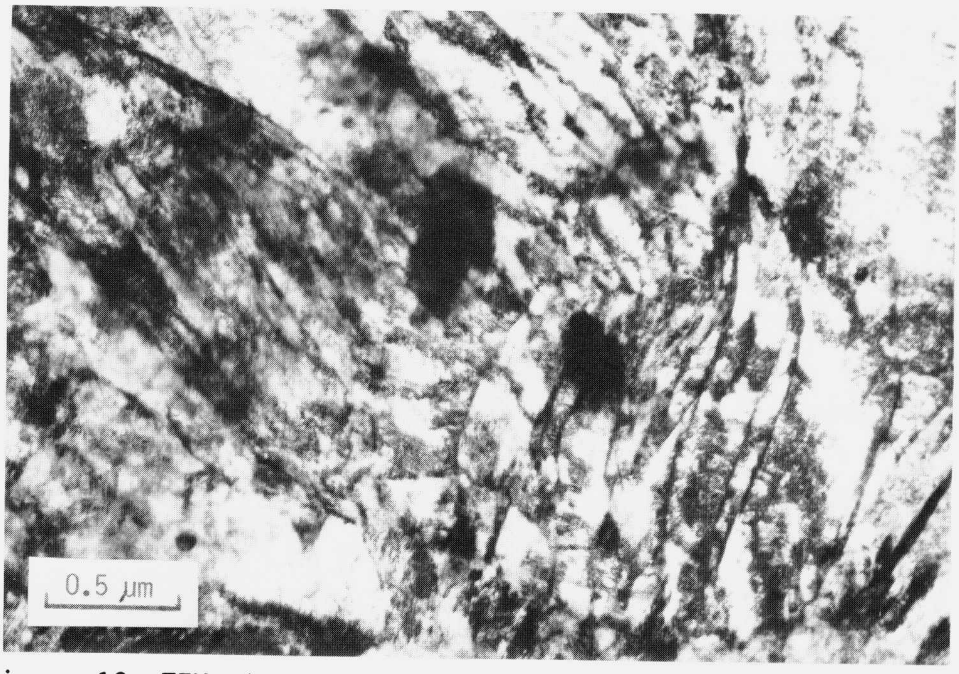

Figure 12. TEM micrograph of the microstructure of 4340 steel at Rc 55, which consisted of undissolved alloy carbides in a matrix of heavilly dislocated lath martensite.

micrograph was taken in the region which received only uniform deformation and had stopped straining once instability occurred. It was observed that many carbides exhibited this type of behavior. The directions of void growth appear aligned in the direction of the principle stress. Shear cracks linked pairs of carbides predominately along the direction of the imposed shear direction, 45 degrees to the principle stress direction. These experimental observations are consistant with the finite element investigation of interacting voids by Tracey and Perrone [16]. Although specimen preparation by electropolishing may have enlarged the voids, no such voids were observed in identically prepared foils taken from the undeformed grip ends of the specimens. We thus conclude that the voids are genuinely produced by the plastic deformation.

Summarizing, the pressure dependent behavior of the instability strain can be attributed to the stress required to debond the second phase particles from the matrix and form microvoids. This interpretation is supported by the recent analysis by Hutchinson and Tvergaard [17] on microvoid nucleation softening as a basis for shear instability.

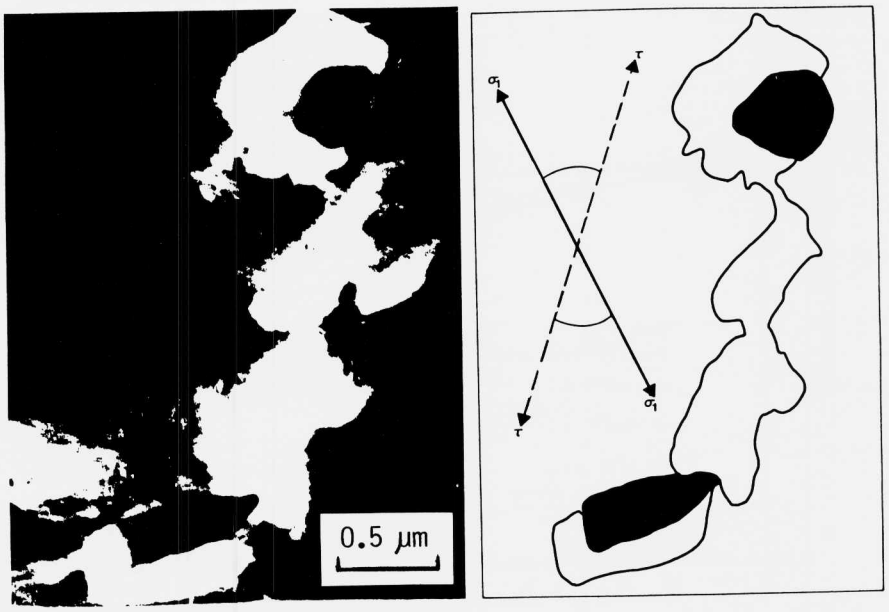

Figure 13. TEM micrograph of microvoid nucleation around a pair of undissolved alloy carbides. The accompanying schematic illustrates the direction of shear and principle stress.

Effect of Austenitizing Temperature

A further test of the role of second phase particles in shear localization can be made by raising the austenitizing temperature to dissolve alloy carbides. Gore [15] has demonstrated that raising the austentizing temperature from 870°C to 1200°C in the same VAR 4340 steel examined here fully dissolves the Cr-Mo alloy carbides leaving primarily fine 80 nm Ti (C, N) particles at a much reduced volume fraction of 0.05 percent. Such a change in the amount and character of undissolved second-phase particles can be expected to significantly alter the critical strain for microvoid nucleation softening. This should be most pronounced in Stage I tempered material where the ultrafine epsilon carbides precipitated during tempering should not contribute to microvoid nucleation, and the role of the undissolved particles would thus be greatest.

A comparison of the shear instability strains measured in linear shear tests on the AM 4340 austentized at 840°C (as in Fig. 8) and 1100°C is presented in Figure 14 using the same four tempering conditions as in Figure 8. Material well

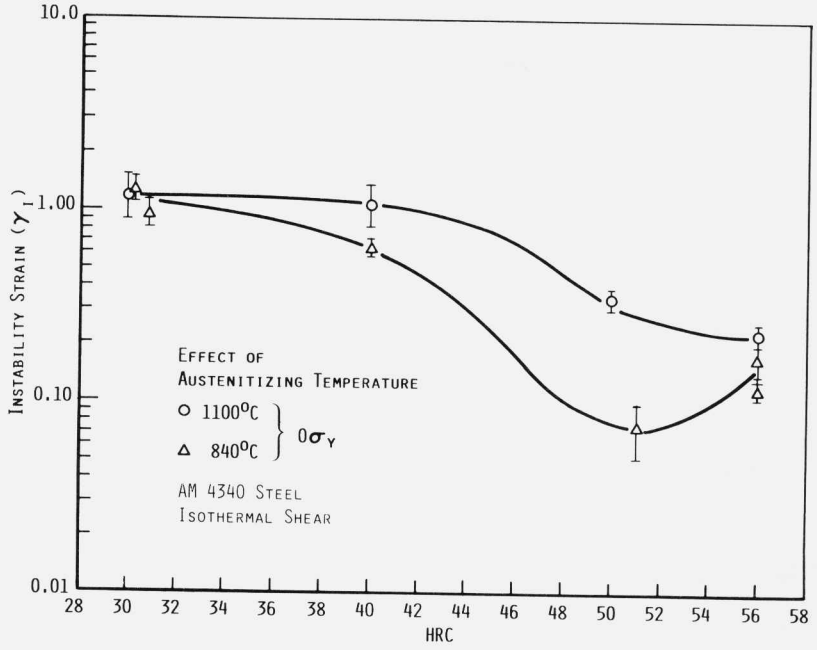

Figure 14. Comparison of instability strains of an AM 4340 steel austenitized at 840°C and 1100°C.

tempered in Stage III to Rc 30 shows no significant increase in instability strain, consistant with a dominant role of the 100 nm cementite particles precipitated during tempering. For lower tempering temperatures (high hardness) where the carbides precipitated on tempering are finer, there is a pronounced increase in instability strain with 1100°C austenitizing, suggestive of an important role of the undissolved alloy carbides in shear localization.

The pressure sensitivity of the shear instability strain in the 1100°C austenitized material is represented in Fig. 15 comparing the behavior without and with a normal compressive stress of 1/6 the yield stress. Though the controlling particles may be changed by austenitizing condition, the persistant pressure sensitivity implies that microvoid softening continues to be the dominant strain softening mechanism. As depicted in Figure 14, the AM 4340 tempered in Stage I at 160°C to Rc 56 hardness shows an increase in the instability strain from the 0.12-0.18 range to 0.23 when the austentizing temperature is raised from 840°C to 1100°C. This is not as large an increase as observed for the Stage II and early Stage III temper conditions (Rc 50 and 40, respectively). A further investigation by Gore [15] of the effect of austentizing temperature in the range of 870°C -

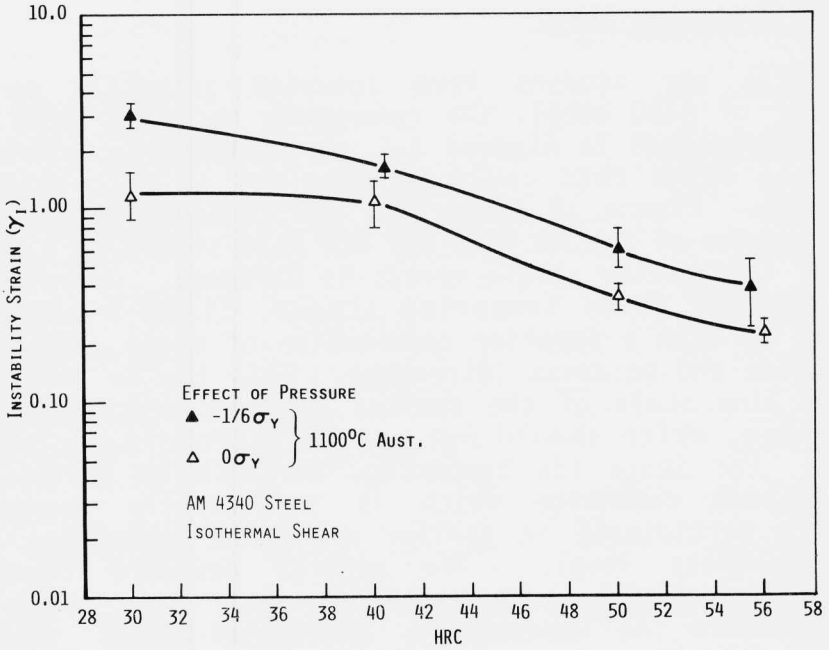

Figure 15. Comparison of instability strains of an AM 4340 steel austenitized at 1100°C with different imposed axial compressive stresses: 0 and 1/6 the yield strength.

1200°C on the instability strain in the VAR 4340 tempered in Stage I at 200°C to Rc 52 has shown a slight monotonic decrease with increasing austenitizing temperature. The effect has been attributed to a contribution of crystal-plasticity-based strain softening mechanisms which may be promoted by grain coarsening. As mentioned previously in discussion of melt practice comparison in Figure 8, the AM 4340 shows greater grain coarsening resistance than the cleaner VAR 4340 and such grain coarsening effects may not have had as strong an influence in the 840°C - 1100°C comparison for the AM material. Pressure sensitivity of the very coarse grained material has not yet been evaluated to test for a change in strain softening mechanism.

The observed increase in the instability strain with particle dissolution in the AM 4340 lends further support for the role of microvoid nucleation softening in shear localization in conventionally treated material. However, the indication that severe grain coarsening can introduce other strain softening contributions limits the practical utility of high temperature austenitizing treatments for enhancement of mechanical properties.

Role of Tempering Stage

While our studies have focussed primarily on the behavior of 4340 steel, the rare-earth modified (REM) 4130 steel represented in Figures 3-6 was included to extend the hardness range that could be examined in each stage of tempering. Figure 16 summarizes the combined linear-shear test results of the AM 4340 and REM 4130 steels in a linear plot of instability strain versus Rc hardness. Grouping the data for the three tempering stages, Stage I tempering appears to show a superior combination of shear instability resistance and hardness (strength). This can be attributed to the fine scale of the epsilon carbides precipitated on tempering, which should not act as microvoid nucleation sites. For Stage III tempering, strength is provided by precipitated cementite which is sufficiently coarse to directly participate in earlier microvoid nucleation at a given hardness level. The general downward trend of instability strain with hardness for each class of microstructure is presumably associated with reaching critical interface stresses at lower strains when the matrix flow stress is increased.

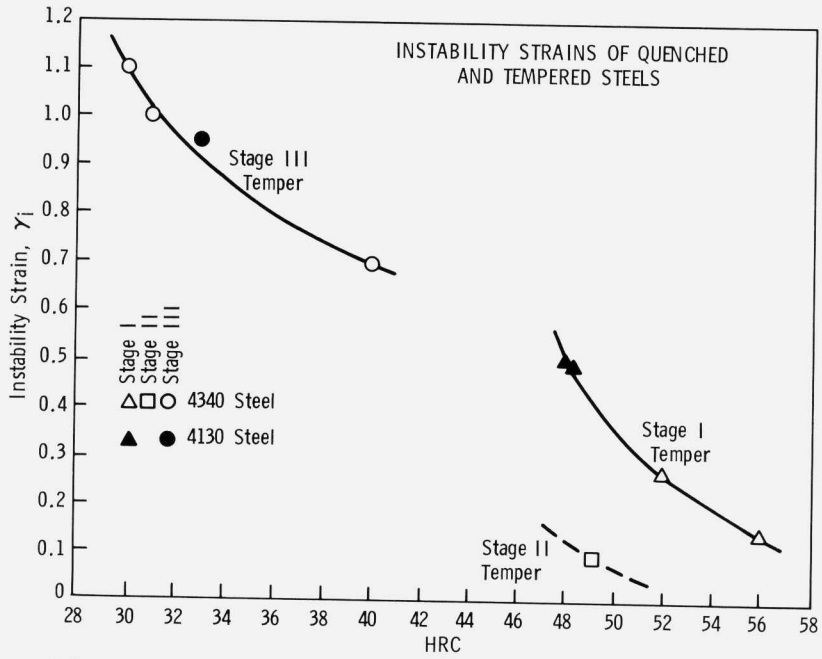

Figure 16. Comparison of instability strain curves of quenched and tempered steels having stage I, stage II, and stage III structures.

The much lower shear instability resistance of the Stage II tempered microstructure correlates with a minimum in the Charpy impact energy commonly known as the tempered martensite embrittlement trough. This implies a connection between low Charpy energy and early shear localization. As the instability strain is still pressure sensitive in this stage (Figure 11), the embrittlement phenomena associated with retained austenite decomposition in Stage II presumably causes earlier microvoid nucleation.

Comparison with Secondary Hardening Steel: Toughness Correlations

Secondary hardening AF 1410 steel achieves high strength from the precipitation of fine M_2C carbides during tempering at 510°C. Optimum strength/toughness combinations are achieved in a 5 hour temper "overaged" condition for which completion of M_2C precipitation causes dissolution of coarser cementite particles which precipitate earlier during tempering. Optimum melt practice generally involves rare-earth treatments for gettering of sulfur. The shear instability resistance in the standard 510°C/5 hr. tempered condition was measured for two heats with and without the rare earth treatment. Also examined was rare earth treated material tempered 5 hr. at 420°C to provide an "underaged" material of comparable hardness but with the cementite particles present.

The results are compared with those of the Stage I and Stage II tempered 4340 and 4130 steels in a semi-log plot vs. hardness in Figure 17. For the standard 510°C/5 hr. temper the AF1410 shows substantially higher shear instability resistance compared to the Stage I tempered steels. The material without rare-earth treatment is shown to contain relatively fine chromium sulfides. Replacement by rare-earth sulfides and oxysulfides in the rare-earth treated material evidently enhances shear instability resistance, in contrast to the 4340 steels relative insensitivity to melt practice. The 420°C tempered material shows a much lower instability strain consistant with the expected role of undissolved cementite in microvoid nucleation.

Fracture toughness of the same three materials measured at Carpenter Steel [18] shows a similar trend vs. hardness. Expressed as critical crack extension force G_{Ic}, the toughness is compared with available data for 4340 steel in

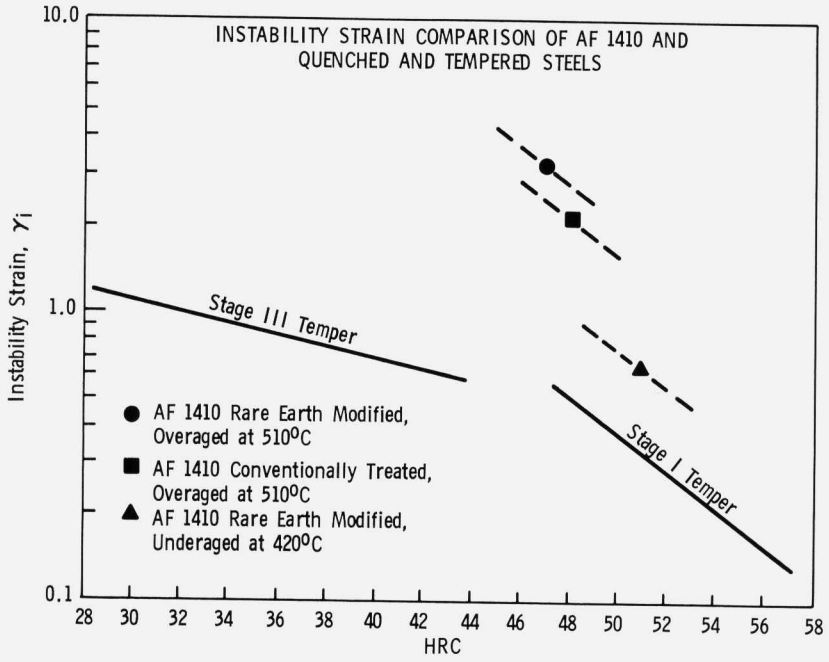

Figure 17. Comparison of instability strains of quenched and tempered steels and three differently processed AF 1410 steels.

Figure 18. A test of the apparent G_{Ic} - instability correlation is plotted in Figure 19, including data for the VAR 4340 austentized at 840°C and tempered 2 hrs. at 200°C to a comparable hardness level of Rc 50. The good correlation observed is in line with the proposed roles of second-phase particles in shear localization and ductile fractures [19, 20].

Further support for the important role of microvoid nucleating partices in the ductile fracture behavior of AF1410 is provided by the solution treatment study of Schmidt and Hemphill [18]. A significant toughness enhancement is obtained on raising the solution treatment temperature from 830°C to 885°C. After conventional treatment at 830°C the microstructure contains chromium rich $M_{23}C_6$ carbides of 900-1800 nm diameter along with smaller 40-80 nm molybdenum rich MC carbides. After 885°C solution treatment the $M_{23}C_6$ carbides are fully dissolved, leaving only the finer MC particles.

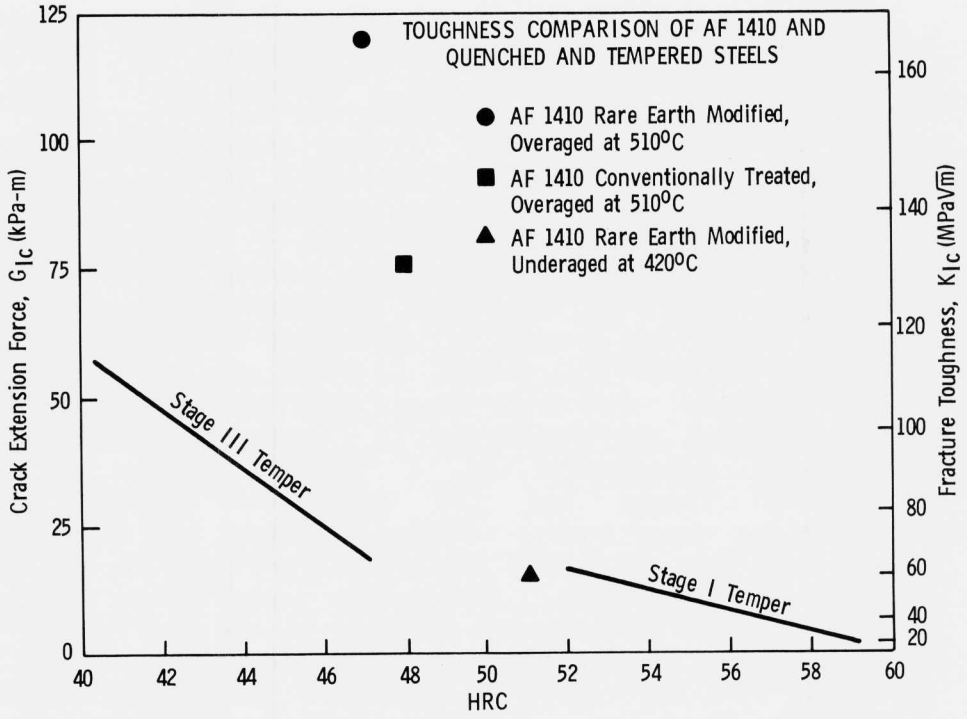

Figure 18. Toughness comparison of AF 1410 and quenched and tempered steels.

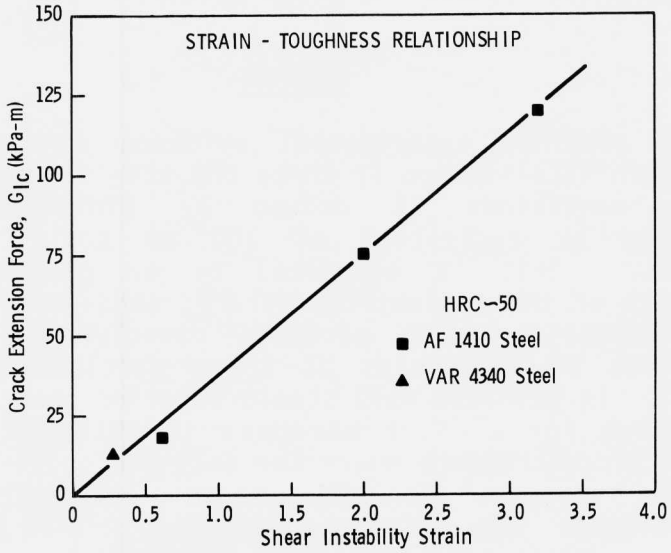

Figure 19. Instability strain - fracture toughness relationship measured on three AF 1410 steels and one VAR 4340 steel.

Microvoid Observations

The fine 100 nm scale of microvoid formation makes microscopy observations difficult compared to the more familiar problem of >100 nm scale "primary" void formation which has been well studied by light metallography. An effort is underway to find further direct evidence for microvoid formation beyond the thin-foil TEM observations of Figure 13, using SEM metallography of lightly etched polished surfaces taken from the gage sections of interrupted shear tests. Referring to the shear stress-strain curve for Rc 55 VAR 4340 in Figure 20, specimens have been examined for the strained conditions denoted by: A) before maximum stress, B) at maximum (instability) stress, C) after maximum stress, and D) near fracture. The shear strain profiles taken from these four specimens are presented in Figure 21, showing the progressive development of a strain plateau at the instability strain and the growth of strain peaks representing shear bands. Figure 22 shows SEM micrographs taken from the uniformly deformed portions of the four specimen gage sections. Microvoids commensurate with the carbide particle size appear abrubtly at the the instability strain (B) with little change in microvoid density within the uniformly strained region as localized deformation proceeds elsewhere. Techniques for enhancing the contrast between microvoids and particles are under investigation. The abrupt appearance of microvoids supports a nucleation-controlled rather than growth-controlled softening mechanism.

SUMMARY

The combined experimental evidence strongly suggests that strain localization in these UHS steels under pure shear loading conditions is driven by microvoid softening controlled by nucleation at 100 nm scale second-phase particles. This is supported by an observed pressure dependence of the instability strain, enhanced resistance to shear instability with particle dissolution, and direct observation of microvoids at these particles in deformed material. In 4340 and 4130 steels superior shear instability resistance for a given hardness is obtained in Stage I tempered microstructure where the only microvoid - nucleating particles appear to be those undissolved during austenitizing. The secondary hardening AF1410 shows a much higher resistance to shear localization when cementite particles are fully dissolved by alloy carbide precipitation.

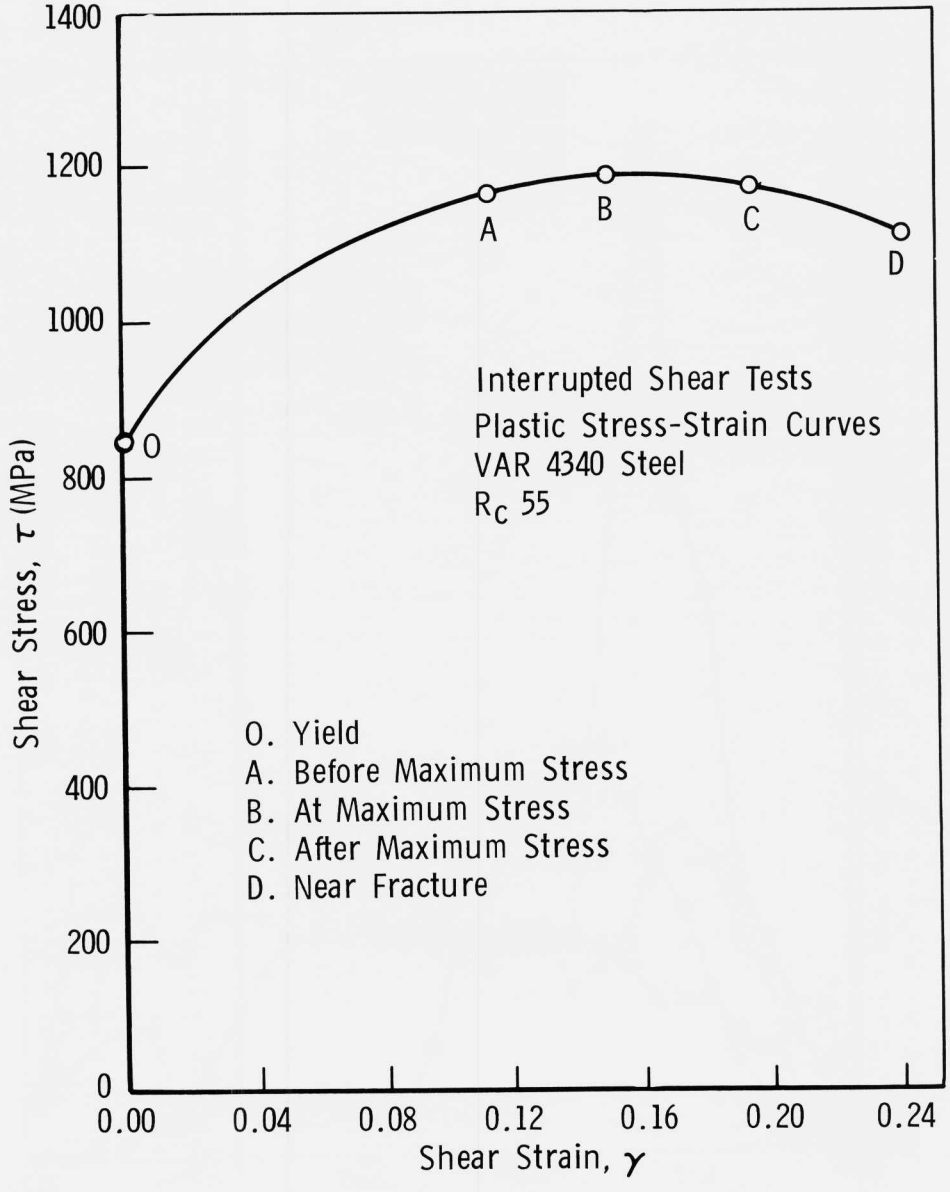

Figure 20. Shear stress-strain curve of a VAR 4340 steel at Rc 55. Interrupted tests were performed to the points indicated (A-D).

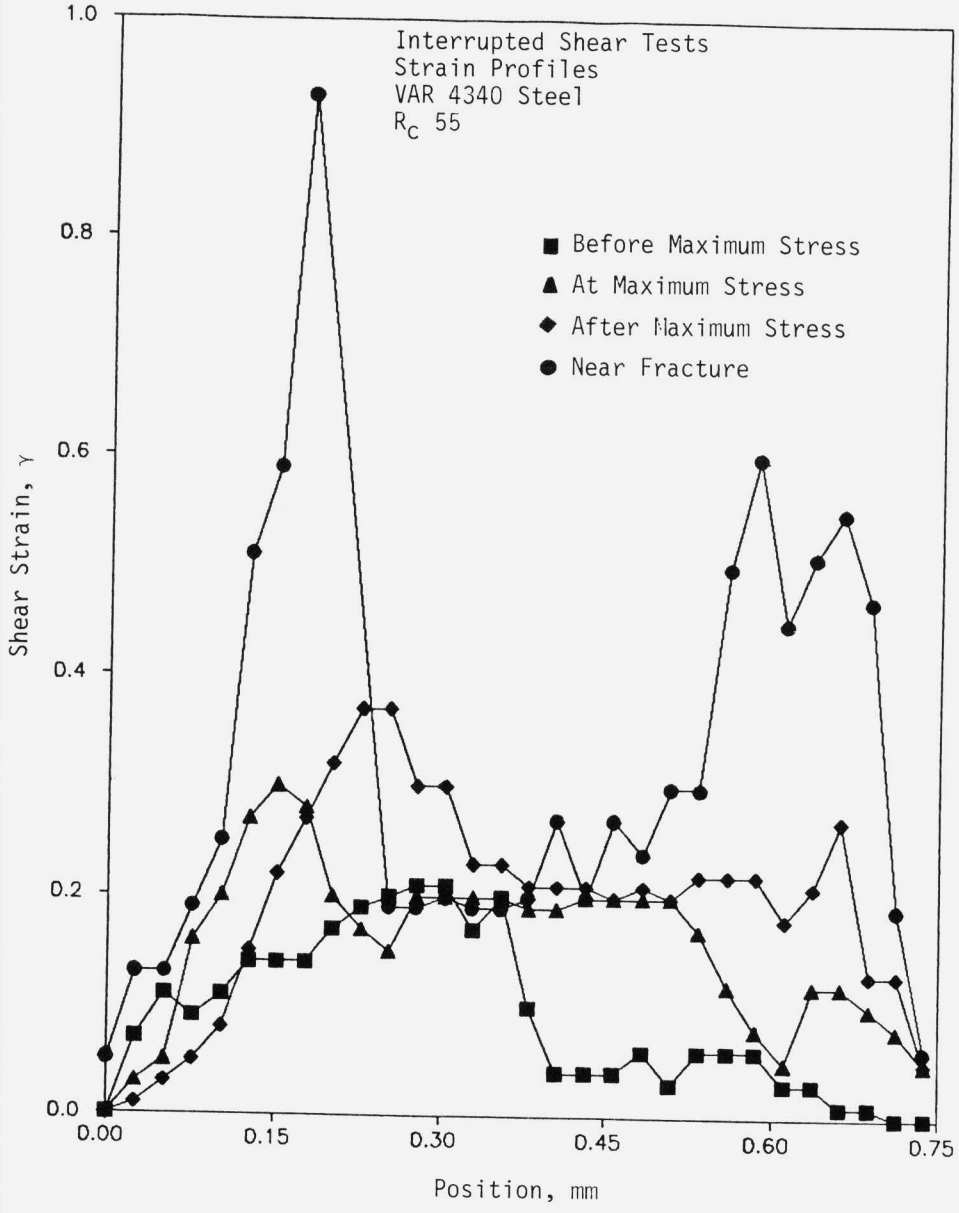

Figure 21. Strain profiles obtained from the interrupted shear tests of a VAR 4340 steel at Rc 55. Interrupted tests were performed to the points indicted (A-D) in Figure 20.

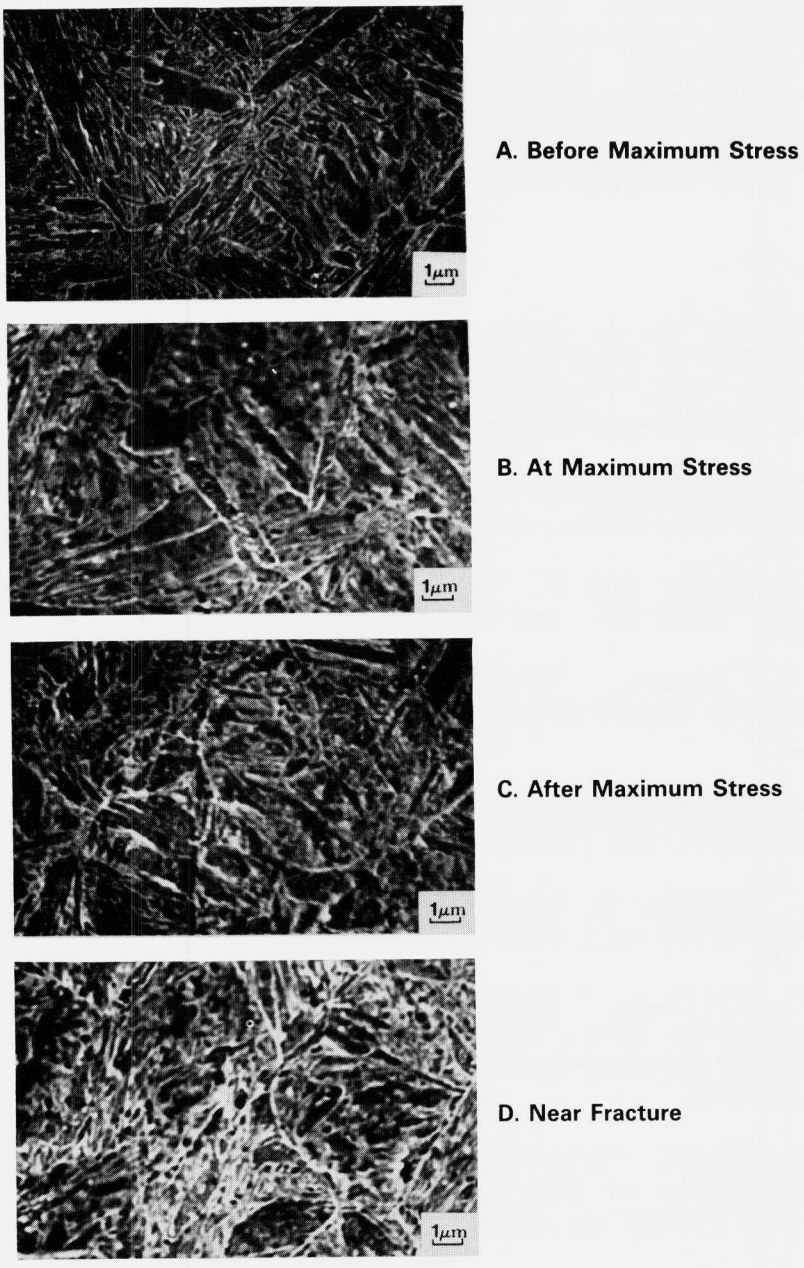

Figure 22. Photomicrographs of the interrupted shear test specimens of a VAR 4340 steel at Rc 55: (A) before maximum stress, (B) at maximum stress, (C) after maximum stress, and (D) near fracture.

For these steels at hardness near Rc 50, a direct correlation between G_{Ic} fracture toughness and shear instability strain is demonstrated. Continued study of microvoid nucleation in pure shear experiments will allow quantification of the role of a critical component of microstructure. Deliberate control of microvoid nucleating particle dispersion offer the potential for design of materials with greatly enhanced resistance to shear localization and ductile fracture.

REFERENCES

1. M. Azrin, J. Cowie, and G. Olson, "Shear Instability Mechanisms in High Hardness Steel," Annals of Israel Physical Society, V.8, Fragmentation, Form, and Flow in Fractured Media (1986), pp.409-417, also MTL TR 87-2.

2. J. Mescall and R. Papirno, "Spallation in Cylinder-Plate Impact", Exp. Mech., V.9 (1979), pp. 283-311.

3. J. Cowie and F. Tuler, "Flow loclization Models -A Review," Mat. Sci. and Eng., V.95 (1987), pp. 93-99.

4. H. Rogers, "Adiabatic Shearing: A Review," Drexel University Report prepared for the U.S. Army Research Office, 1974.

5. H. Rogers "Adiabatic Plastic Deformation," Ann. Rev. Mater. Sci., V.9 (1979) pp. 283-311.

6. A. Bedford, A. Wingrove, and K. Thompson, J. Aust. Inst. Metals, V.19, no.1 (1974)pp. 61-74.

7. R. Clifton, " Adiabatic Shear Banding," in Materials Response to Ultra High Loading Rates, Chap. 8 National Materials Advisory Board Committee, Rep. No. NMAB-356 (1980), pp. 129-142.

8. A. Argon, "Stability of Plastic Deformation," in The Inhomogeneity of Plastic Deformation, Chap. 7, ASM, Metals Park, OH (1973), pp.161-189.

9. L. Samuels and I. Lamborn, "Failure Analysis of Armament Hardware," in Metallography in Failure Analysis, J. McCall and P. French, eds., Plenum Press, NY (1978), pp. 167-190.

10. G. Olson, J. Mescall, and M. Azrin, "Adiabatic Deformation and Strain Localization, " in Shock Waves and High-Strain-Rate Phenomena in Metals, M. Meyers and L. Murr, eds., Plenum Press, NY (1981), Chap. 14.

11. T. Walker and M. Shaw, "On Deformation at Large Strains,"in Advances in Machine Tool Design and Research, S. Tobias and F. Koenigsberger, eds., Pergamon Press, NY (1969), p. 241.

12. H. Luong, "A Study of Microvoid Formation in Metal Cutting," Ph.D. Thesis, Monash University, Victoria, Australia (1977).

13. H. Luong, in "Proceedings of the Australian Conference on Manufacturing Engineering," Monash University, Victoria, Australia (1977), p.122.

14. D. Tracey and P. Perrone, "Shear Specimen Stress Analysis," Presentation at the Second Annual Steel Research Group Meeting (1986), MIT, Cambridge, MA.

15. M. Gore, G. Olson, and M. Cohen, "Particle Dispersion in UHS Martensitic Steel," Proceedings of the Thirty-fourth Sagamore Army Materials Research Conference (1987).

16. D. Tracey and P. Perrone, "Modeling of Interactions in Void Nucleation and Growth," Proceedings of the Thirty-fourth Sagamore Army Materials Research Conference (1987).

17. J. Hutchinson and V. Tvergaard, "Microvoid Nucleation Softening in Metals," Proceedings of the Thirty-fourth Sagamore Army Materials Research Conference (1987).

18. M. Schmidt and R. Hemphill, "Solution Treatment Effects in AF 1410 Steel," Proceedings of the Thirty-fourth Sagamore Army Materials Research Conference (1987).

19. O. Onyenwuenyi, "Microstructural Aspects of Flow Localization and Plastic Instability," Scripta Metall., V.18 (1984), pp.455-458.

20. A. Needleman and V. Tvergaard, "Crack Tip Stress and Deformation Fields with a Solid Vertex in Its Surface," Brown University Tech. Report No. 87, November, 1981.

SECONDARY PARTICLE DISPERSIONS AND IMPURITY GETTERING IN ULTRAHIGH STRENGTH STEELS

CLIVE HAYZELDEN
Division of Applied Sciences, Harvard University, Cambridge, MA 02138.

INTRODUCTION

The development of ultrahigh strength (UHS) in steel is often achieved only at the expense of toughness and with increased susceptibility to stress corrosion cracking (SCC). High hardness martensitic steel used for structural applications involving significant tensile loading and requiring a K_{IC} fracture toughness of 50 MPa.$\sqrt{m}$, is limited to a Rockwell C hardness (R_C) of 50-55, or an ultimate tensile strength (UTS) of 1700-2100 MPa. The replacement of R_C 50-55 hardness steel with a R_C of 55-60 and a UTS in the range 2100-2400 MPa, would, for a constant critical flaw size, require the simultaneous development of a K_{IC} in the range 70-130 MPa.$\sqrt{m}$ [1].

In service, UHS steels commonly fail by a mechanism of plastic shear instability in which flow localization leads to the formation of intense shear bands. With the aim of improving the toughness of UHS steel, we have investigated the microstructural features underlying the phenomenon of plastic shear instability and flow localization in 4340 steel produced by air melt (AM) and vacuum arc remelt (VAR) techniques.

In addition to the toughness limitations described above, UHS steels are highly susceptible to environmentally induced SCC. The threshold stress intensity for stress corrosion cracking, K_{ISCC}, is typically of the order of 10 MPa.$\sqrt{m}$. Improved reliability is sought from these steels through attempts to raise K_{ISCC} to levels approaching that of K_{IC}. In SCC, failure occurs by a brittle intergranular mode, predominantly at prior austenite grain boundaries and with negligible local plasticity [2].

The mechanism of SCC in UHS steels is hydrogen embrittlement promoted by cathodic crack-tip processes. The hydrogen susceptibility of the prior austenite boundaries is very sensitive to the presence of co-segregating embrittling metalloids. Since Mn and Cr are believed to cosegregate with P and S in steels, a low Mn-Cr modification of 4340 steel containing additional Ni and Mo has been developed. To this Ni-Mo steel, late additions of the rare earth element, lanthanum, have been added in an attempt to scavenge residual P. It is intended that rapid solidification processing (RSP) should yield, in addition to a fine grained austenite solidification structure and martensitic transformation product, a fine dispersion of coarsening-resistant La precipitates. The La precipitates should provide, through grain boundary pinning, resistance to excessive grain growth during subsequent high-temperature austenitization. Preliminary observations are reported of the size, morphology and chemistry of the precipitates formed in a modified 4340 UHS steel to which La was added prior to RSP by centrifugal atomization.

BACKGROUND

Azrin et al. [3] and Cowie et al. [4], have recently shown that the critical strain for shear localization in UHS 4340 steel was nearly identical for both isothermal (quasistatic) and adiabatic (dynamic) shear. The nearly identical instability strains and shear localization behavior in UHS steel at both high and low strain rates indicates that thermal softening provides insufficient explanation of the underlying cause of the observed shear instability. Observations that the instability strain was strongly influenced by the application of a compressive hydrostatic stress indicates that microvoid nucleation may contribute to the strain softening effects underlying plastic shear localization.

When the austenitizing temperature of the AM 4340 alloy was raised from 840°C to 1100°C prior to stage I tempering (R_C 55-56), the instability strain during shear testing, γ_I, showed an increase from around 0.12-0.18 to approximately 0.23. For the AM

alloy austenitized at 840°C, double linear shear tests were run quasistatically with the application of an axial compressive stress of 1/3 and 1/6 the tensile yield stress, σ_γ. It was found that the instability strain during isothermal shear rose from a base value of 0.12 with zero applied load, through 0.4 at 1/6 σ_γ, to 1.5 at 1/3 σ_γ. For the 1100°C austenitized material, the application of a compressive load equal to 1/6 σ_γ raised γ_i from 0.23 to 0.4.

Cowie et al.[4] have in addition investigated the role of melt practice upon alloy toughness. For example, VAR 4340 Steel austenitized at 870°C was stage I tempered and tested in quasistatic torsion. The high cleanliness material showed a virtually identical instability strain to that shown by the 840°C austenitized AM alloy.

MATERIALS AND METHODS

Two Alloys based on the 4340 composition and one Ni-Mo steel have been examined. These alloys were prepared by air melting (AM), vacuum arc remelting (VAR) and rapid solidification processing (RSP) respectively. The compositions of the AM, VAR and RSP alloy steels are presented in Table I.

TABLE I

COMPOSITIONS (WT%) OF AM, VAR AND RSP STEELS

Steel	C	Mn	P	S	Si	Cr	Ni	Mo	Cu	La
AM	.41	.75	.005	.011	.25	.79	1.71	.24	.13	-
VAR	.42	.46	.009	.001	.28	.89	1.74	.21	.19	-
RSP	.48	.03	.015	.005	.10	.32	2.52	1.68	-	.06

The AM 4340 alloy was normalized at 910°C for one hour then austenitized at either 840°C or 1100°C

for one further hour. Following the austenitization treatments, the AM specimens were given a one hour stage I tempering treatment at 160°C to form epsilon carbide and produce a peak hardness in the range R_C 55-56. The VAR steel examined in this microstructural study was austenitized at 870°C without an additional tempering treatment. The rare earth modified Ni-Mo steel was prepared by the addition of $LaNi_5$ to the melt at 1600°C. The rapidly solidified powder particles produced by centrifugally atomization were embedded in electro-plated Ni prior to thinning for examination in a transmission electron microscope.

Bulk samples of the 840°C and 1100°C austenitized AM alloy were ground and polished using a combination of silicon carbide grit and alumina powder. The polished samples were etched with a 2% solution of nitric acid in methanol prior to examination by scanning electron microscopy (SEM). The fracture surfaces of the AM 4340 alloy austenitized at 840°C were examined directly by SEM without further treatment using a JEOL JSM 35U SEM operated at an accelerating potential of 35 kV. Microanalysis was performed at an accelerating potential of 20 kV and a Tracor Northern TN2000 multi-channel analyser was used to record the x-ray spectra.

Thin foils were prepared for transmission electron microscopy (TEM) by a combination of mechanical pre-thinning, electro-chemical polishing and ion-beam thinning. Specimen pre-thinning was carried out using a South Bay Technology Model 510 dimpling instrument. Jet electro-polishing was carried out using a solution of 20% perchloric acid in methanol in a South Bay Technology model 550C twin-jet electro-polisher. Ion-milling was performed using Ar^+ ions in a Gatan Duo Mill operated at 4 KV and 1 mA beam current. Carbon extraction replicas (CER) were prepared by polishing the AM and VAR 4340 steels to a 1 μm finish, lightly etching with a 2% solution of nitric acid in methanol (nital) and coating the surface with evaporated carbon. The carbon-coated surface was scored into 3 mm squares and loosened from the matrix by further etching with

the nital solution. The carbon extraction replicas were floated off in de-ionized water and collected on 3 mm, 400 mesh Cu grids.

Transmission electron microscopy was carried out on a Philips EM 420T (S)TEM equipped with an EDAX 184 energy dispersive x-ray detector, Gatan model 607 electron energy loss spectrometer and Tracor Northern TN5500 multi-channel analyser. Conventional bright and dark field imaging, convergent beam electron diffraction (CBED), x-ray (EDS), and electron energy loss (EELS) spectroscopy were carried out at accelerating potentials of 100 kV and 120 kV.

RESULTS

Air Melt 4340 alloy

The 840°C and 1100°C austenitized alloys showed an approximately 0.2% areal fraction of MnS stringers that were 10-30 μm in length. As shown in figure (1a) for the 840°C austenitized steel, where the MnS stringers appear brighter than the matrix, a typical inter-particle spacing of 70 μm was observed. A similar distribution of MnS stringers was seen in the 1100°C austenitized specimens. Figure (1b) shows a large MnS stringer in the 1100°C austenitized alloy in which a dark, Al-Ca rich, spherical nucleus may be seen. Figure (1c) shows a fracture surface from the shear tested 840°C austenitized alloy. Sheet microvoid failure was associated with the intense shear localization that occurred during double linear shear testing. Figure (1d) shows a high magnification micrograph of the fracture surface of the 840°C austenitized alloy. Several MnS precipitates of around 1 μm diameter, and 15-20 μm separation may be seen within the larger voids. The microvoids on the fracture surface show a nearest neighbor spacing of approximately 0.75 μm. Fine particles, around 1000 Å in diameter, could occasionally be resolved within these voids using SEM.

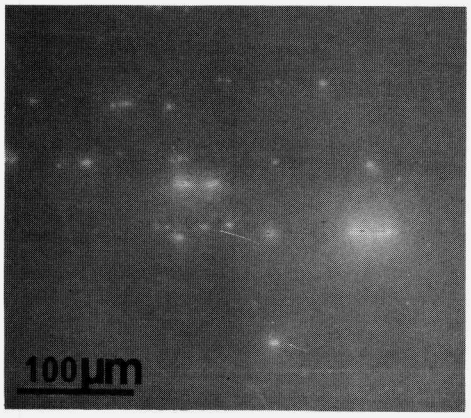

Fig.1a. Scanning electron micrograph of 840°C austenitized steel showing MnS stringers aligned in rolling direction.

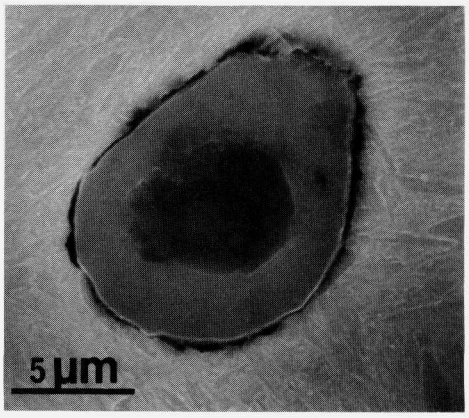

Fig.1b. Scanning electron micrograph of 1100°C austenitized steel showing large MnS stringer which has precipitated on a nucleus of Al/Ca-rich slag.

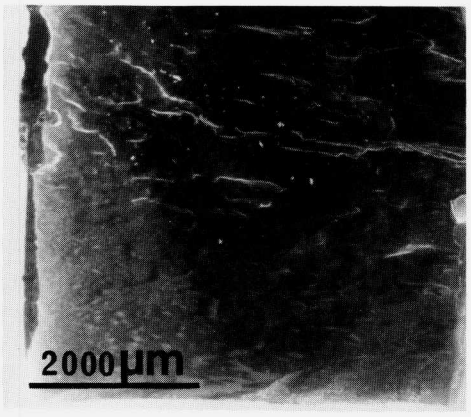

Fig.1c. Low magnification scanning electron micrograph of fracture surface of 840°C austenitized AM steel sample following double linear shear testing with 1/3 σ_γ load.

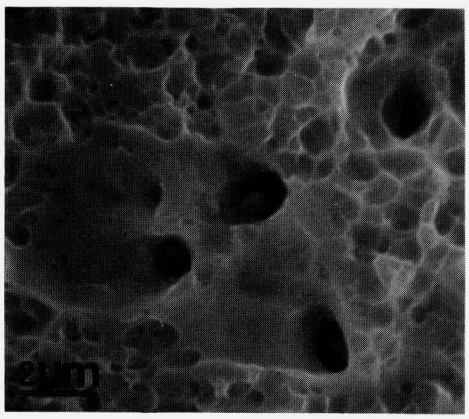

Fig.1d. High magnification scanning electron micrograph showing sheet microvoid failure and MnS inclusions on fracture surface of 840°C austenitized AM steel.

Carbon extraction replicas revealed a combination of fine-scale MnS, AlN and Ti(CN) precipitate phases within the AM alloy following both austenitization treatments. The areal number density of second phase precipitates, determined directly from the carbon extraction replicas, was however, considerably lower following the higher temperature austenitization treatment. Spherical MnS particles of 1600 Å diameter and with an areal number density of 2.10^9 m^{-2} were noted in the 840°C austenitized alloy. This was in agreement with the observation of similar sized MnS precipitates within some of the larger voids on the fracture surface of the 840°C austenitized alloy (see figure 1d). The same alloy revealed a high density, 5.10^{12} m^{-2}, of rectangular parallelepiped AlN precipitates of average length 529 Å. Figure (2a) shows a typical low magnification image of such a cluster of precipitates. These precipitates formed the dominant second phase within the steel and corresponded well with the observed density of voids on the fracture surface (some of the larger precipitates were probably just observable by SEM). Round-cornered square plate Ti(CN) precipitates were also observed, although with a significantly lower number density of around 10^9 m^{-2}.

At the higher austenitization treatment of 1100°C, the CER revealed AlN precipitates with an average length of 460 Å and an areal number density of 6.10^{11} m^{-2}. Figure (2b) shows an unusually large and faulted AlN precipitate, around 1500 Å in length, from the 840°C austenitized material. The sharply angular appearance was typical of the AlN precipitates. Figure (2c) shows an AlN precipitate in the 840°C material with length 615 Å and width 350 Å. The corresponding diffraction pattern is shown in figure (2d). The CBED pattern was taken along the $[11\bar{2}0]$ zone axis. The $[11\bar{2}0]$ zone axis in the hexagonal AlN phase is quite distinctive and contains dynamic absences (dark bars) in the kinematically forbidden (0001) reflections as a result of the glide plane parallel to the beam and a perpendicular 2_1 screw axis [5]. The dark bars were confirmed as dynamic absences by their insensitivity to crystal thickness and accelerating voltage.

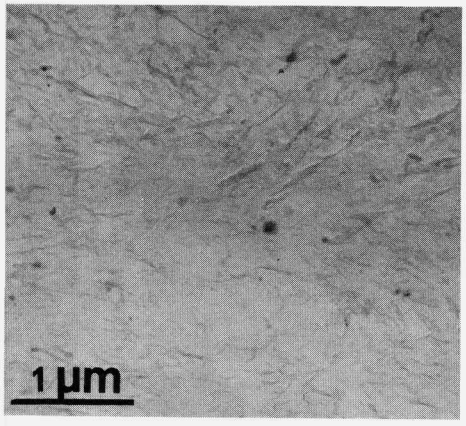

Fig.2a. Transmission electron micrograph of 840°C austenitized AM steel. CER showing AlN precipitates with a similar number density to that of the fracture surface microvoids.

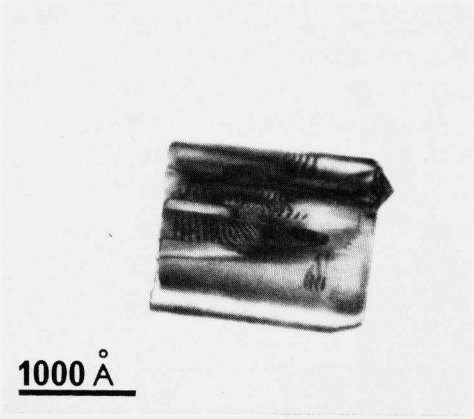

Fig.2b. Transmission electron micrograph showing AlN precipitate extracted from 840°C austenitized AM steel.

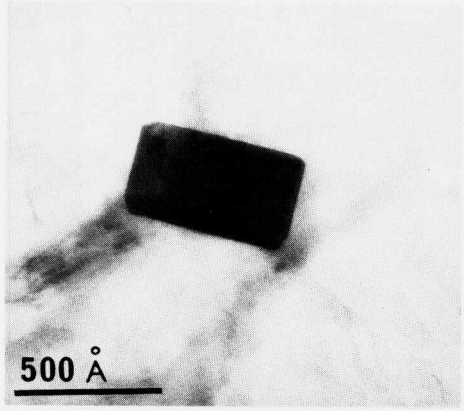

Fig.2c. Transmission electron micrograph showing AlN precipitate extracted from 840°C austenitized AM steel.

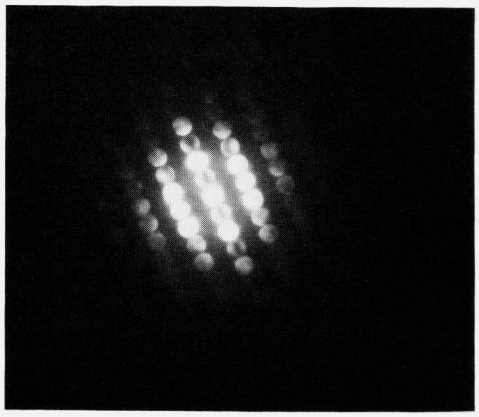

Fig.2d. CBED pattern recorded at the $[11\bar{2}0]$ zone axis from the AlN precipitate shown in fig.2c. Dynamic absences occur within the (0001) (and alternate systematic) reflections.

Figure (3a) shows a very similar CBED pattern recorded from a different AlN precipitate also oriented at the $[11\bar{2}0]$ zone axis and at an accelerating potential of 120 KV. A longer diffraction camera length was used to reveal details within the diffraction discs. Figure (3b) shows the diffraction pattern subsequently obtained from the same crystal at a lower accelerating potential of 100 kV, and in which the characteristic dark bars within the (0001) reflections remain. Figures (3c) and (3d) show the corresponding x-ray and energy loss spectra from the AlN precipitate shown in figure (2c). The presence of minor quantities of Si, shown in the x-ray spectra is not uncommon for AlN. The small Fe peak results from traces of the matrix attached to the extracted precipitate, whilst the Cu grid gave rise to the large peaks to the right of the spectrum. The EEL spectrum shows the clear presence of a N absorption K-edge. An oxygen absorption edge, indicative of the Al_2O_3 phase, was not observed.

Figure (4a) shows a Ti(CN) precipitate extracted from the 840°C material. The square plate crystals displayed rounded corners and an average diameter of 145 Å. The Ti(CN) precipitates exhibited a number density of 2.10^{11} m^{-2}. This may be compared with the alloy austenitized at 1100°C, where the number density fell to approximately 10^{10} m^{-2}. Figure (4b) shows a CBED pattern from the precipitate in figure (4a) oriented at the $[\bar{1}12]$ zone axis. Both the first and second order Laue zones may be seen. The corresponding EDS and EELS spectra for this precipitate are shown in figures (4c) and (4d) respectively. X-ray spectra in general revealed the presence of trace quantities of Cr, Nb, and Mo. Small quantities of Si and Al were observed in some of the precipitates. The EELS spectrum in figure (4d) revealed a small N-K absorption edge in addition to a much larger C-K edge (which resulted in part from the C substrate) and Ti-L_1 edge. Nitrogen was not found in all precipitates. Figure (5a) shows a second Ti(CN) precipitate of 900 Å diameter from the 840°C austenitized alloy recorded with the crystal in the [001] orientation. The corresponding diffraction pattern is shown in figure (5b). The Ti(CN)

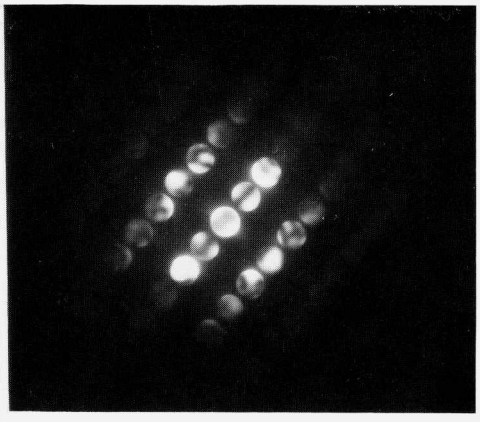

Fig.3a. CBED pattern from AlN precipitate in 840°C austenitized AM steel. Oriented at the $[11\bar{2}0]$ zone axis and with an accelerating potential of 120kV.

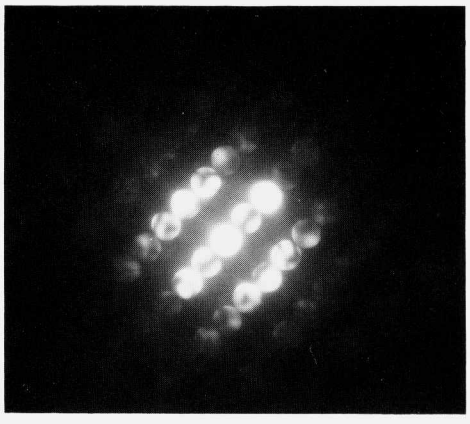

Fig.3b CBED pattern from AlN precipitate in 840°C austenitized AM steel. Oriented at the $[11\bar{2}0]$ zone axis and with an accelerating potential of 100kV.

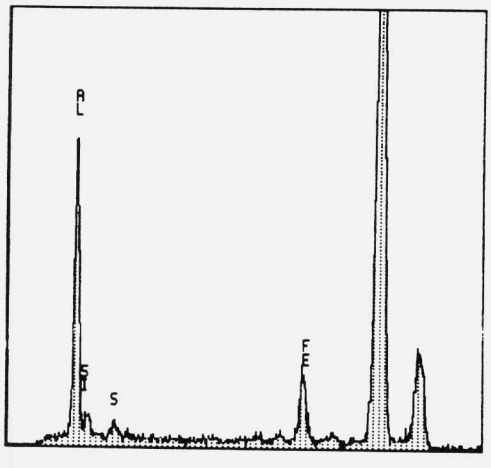

Fig.3c X-ray spectrum from AlN precipitate shown in fig.2c.

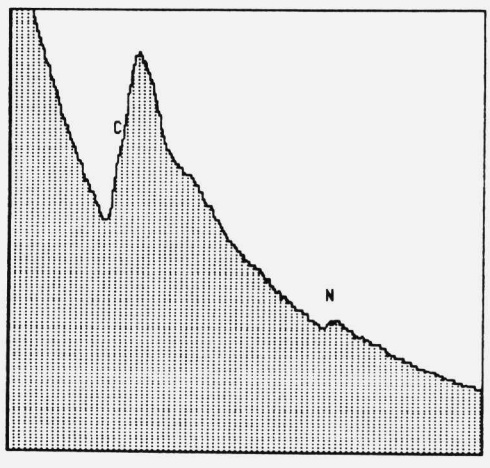

Fig.3d EELS spectrum from AlN precipitate shown in fig. 2c.

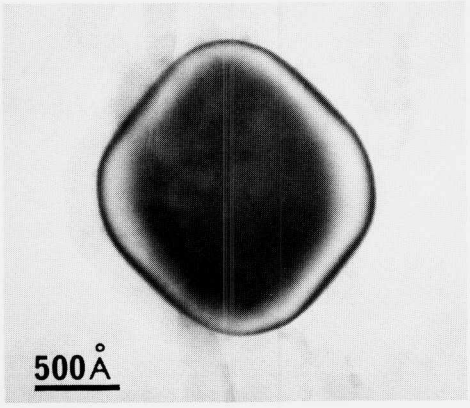

FIG.4a. Transmission electron micrograph showing Ti(CN) precipitate from 840°C austenitized AM steel.

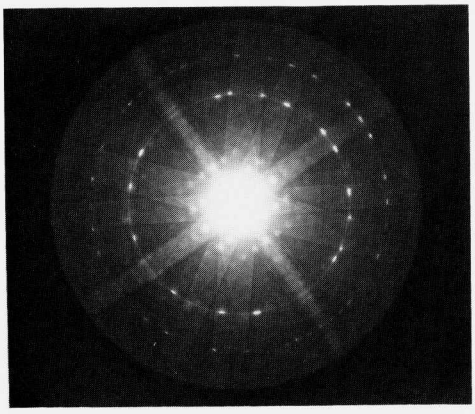

Fig.4b. CBED pattern from the Ti(CN) precipitate shown in fig. 4a oriented at the $[\bar{1}12]$ zone axis.

Fig.4c. X-ray spectrum recorded from Ti(CN) precipitate shown in fig. 4a. Note trace quantities of Cr, Mo and Nb.

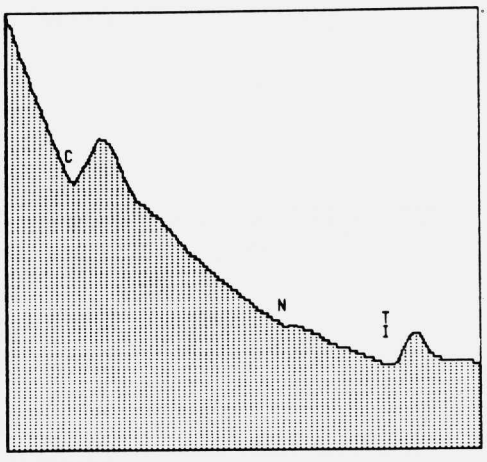

Fig.4d. EELS spectrum recorded from the Ti(CN) precipitate shown in fig. 4a. A small N K-edge was observed in addition to the high-loss Ti-$L_{2,3}$ edge.

phase was found to be an fcc Hägg compound with a lattice parameter (derived from the radius of the FOLZ ring) of 4.4 Å. This is in good agreement with the lattice parameters recorded by Goldschmidt [6] for TiC and TiN of 4.328 Å and 4.244 Å respectively. The second phase particles observed in the AM and VAR 4340 steels are summarized in Table II.

TABLE II

A SUMMARY OF THE SECOND PHASE PARTICLES OBSERVED IN AM AND VAR 4340 UHS STEELS

Steel	Phase	Shape	Size	Density
AM 4340 840°C Austenitization				
	MnS	Stringers	10-20 μm	0.2% area
	MnS	Spherical	1600 Å	2.10^{9} m^{-2}
	AlN	Rectangular Parallelepiped	530 ±130 Å	5.10^{12} m^{-2}
	Ti(CN)	Round-Cornered Square Plate	145 Å	Trace
AM 4340 1100°C Austenitization.				
	MnS	Stringers	10-30 μm	0.2% area
	AlN	Rectangular Parallelepiped	460 ±280 Å	6.10^{11} m^{-2}
	Ti(CN)	Round-Cornered Square Plate	500 Å	Trace
VAR 4340 870°C Austenitization.				
	$(FeCrMo)_{23}C_6$	Spherical	1200 ±600 Å	2.10^{11} m^{-2}
	TiNb(CN)	Rectangular Parallelepiped	800 ±300 Å	2.10^{10} m^{-2}

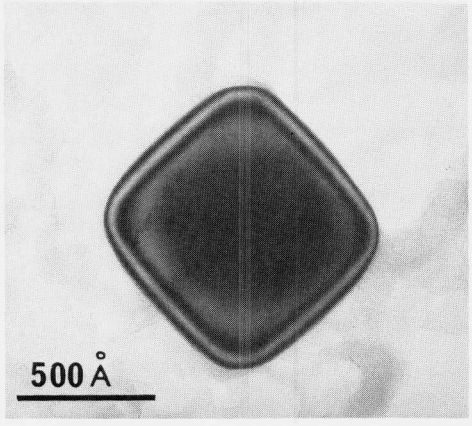

Fig.5a. Transmission electron micrograph of Ti(CN) precipitate from the 840°C austenitized AM alloy recorded with the crystal in the [001] orientation.

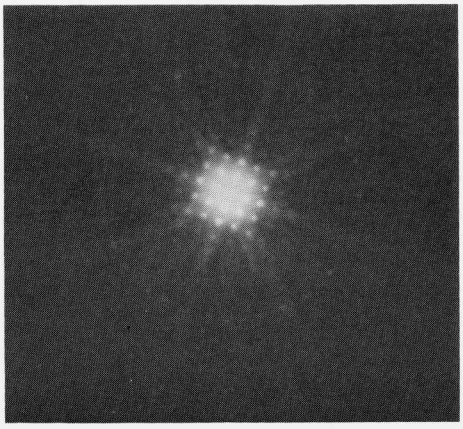

Fig.5b. CBED pattern recorded along the [001] zone axis of the Ti(CN) precipitate shown in fig. 5a. The FOLZ ring is clearly visible at a reciprocal spacing of 3.65 $Å^{-1}$.

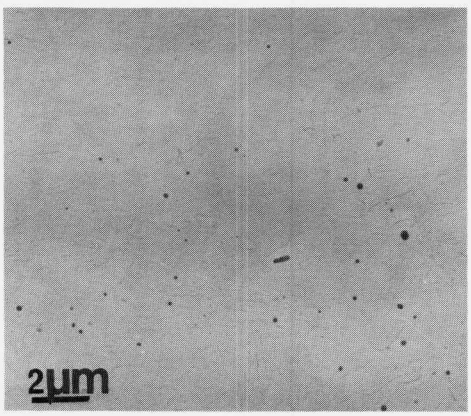

Fig.6a. Transmission electron micrograph of a carbon extraction replica from VAR 4340 steel. The precipitates are mostly $(FeCrMo)_{23}C_6$.

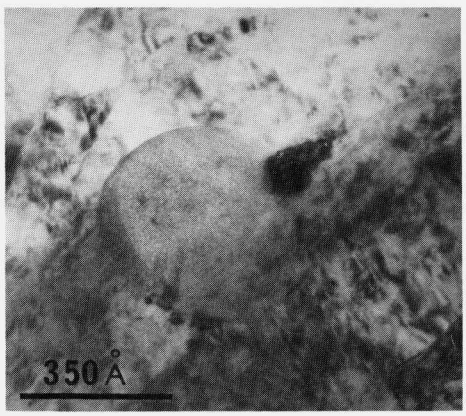

Fig.6b. Bright field transmission electron micrograph of VAR 4340 steel matrix containing an $(FeCrMo)_{23}C_6$ precipitate.

Vacuum Arc Remelt 4340 Steel

The VAR 4340 steel was composed of a lath martensitic matrix with a prior austenite grain size of 20 μm. Second phase particles in this steel were of the $M_{23}C_6$ and MX types. Figure (6a) shows a carbon extraction replica onto which $M_{23}C_6$ precipitates, mostly spherical and of average diameter 1200 Å have been extracted. The number density of the $M_{23}C_6$ precipitates was found to be 1.2 10^{11} m^{-2}. Figure (6b) shows a TEM bright field image of a 2,400 Å diameter precipitate within the heavily dislocated lath-martensitic VAR steel matrix. Figures (6c) and (6d) show the x-ray spectra obtained from the matrix and precipitate shown in figure (6b). The Fe-rich matrix showed Ni and Cr levels of approximately 1.3 and 1.0 at.% in good agreement with the bulk composition of the steel. The embedded precipitate exhibited both a sizeable Cr K_α peak and a smaller Mo L_α peak toward the left hand side of the spectrum. Semi-quantitative analysis of similar spectra was carried out on precipitates extracted onto carbon replicas to estimate the site occupation ratios of the metallic components in the precipitates.

Figure (7a) shows a carbon extraction replica exhibiting $(FeCrMo)_{23}C_6$ and Ti(Nb)CN precipitates. The rounded $(FeCrMo)_{23}C_6$ precipitate was 3200 Å long whilst the sharply angular Ti(Nb)CN precipitate was 1200 Å long. A CBED pattern recorded from the $(FeCrMo)_{23}C_6$ precipitate at the [111] orientation is shown in figure (7b). Measurements of the spacing of both the {220} reflections in the zero order Laue zone (ZOLZ) and the radius of the first order Laue zone (FOLZ) yielded a lattice parameter of 10.8 Å. The corresponding x-ray spectrum, is shown in figure (7c). From a series of 20 analyses the precipitates were found to have an average composition of: Fe-74.2$\pm$3.2at%, Cr-25.1$\pm$3.2at% and Mo-0.7$\pm$0.1at%. The quoted errors correspond to the standard deviation of the normalized concentrations. The precipitates may thus be documented in the form: $(Fe_{.742}Cr_{.251}Mo_{.007})_{23}C_6$. A minor component of Si was also observed in the majority of the precipitates. When included in the compositional analysis, the mean Si content was found to be 1.1at% with a standard deviation of 0.6at%.

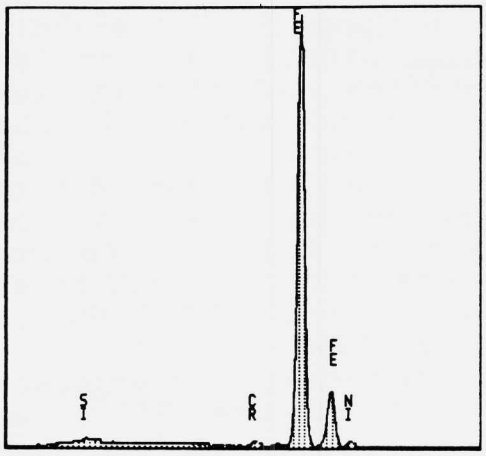

Fig.6c. X-ray spectrum from matrix surrounding precipitate in fig. 6b.

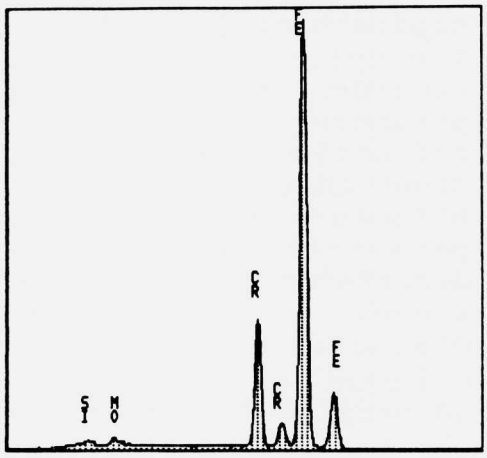

Fig.6d. X-ray spectrum from $(FeCrMo)_{23}C_6$ precipitate in fig. 6b.

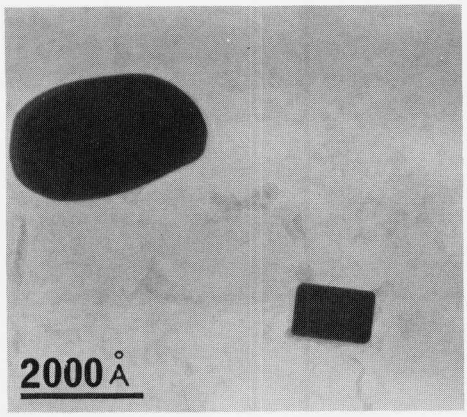

Fig.7a. Transmission electron micrograph of carbon extraction replica exhibiting a rounded $(FeCrMo)_{23}C_6$ and a parallelepiped Ti(Nb)-CN precipitate.

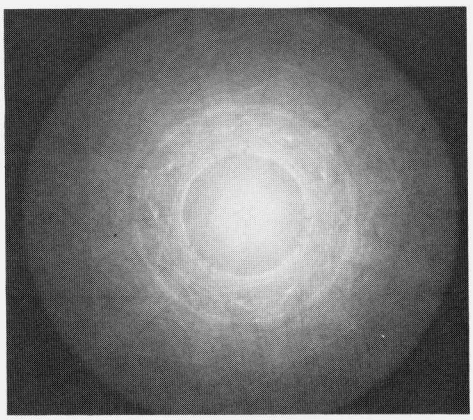

Fig.7b. CBED pattern recorded from the $(FeCrMo)_{23}C_6$ precipitate oriented at the [111] zone axis in fig. 7a. Three HOLZ rings may be seen, the first occurring at a reciprocal spacing of 1.79 $Å^{-1}$.

A further example of a large $(FeCrMo)_{23}C_6$ precipitate of 3,400 Å length is shown in figure (7d). The corresponding diffraction pattern (figure 7e) recorded at the [011] orientation yielded a lattice parameter of 10.8 Å from the {200} and {111} ZOLZ reflections, and 11 Å from the radius of the second order Laue zone (note that the FOLZ is absent due to structure factor considerations and that lattice parameter measurements suffer from increasing distortion at higher angle regions of the back focal plane). The fine detail within the ZOLZ disks is characteristic of the $M_{23}C_6$ phase at the [011] orientation and provides an additional 'fingerprint' identification of the phase [5]. Figure (7f) shows the electron diffraction pattern obtained from this fcc precipitate after tilting to the [001] zone axis. Measurement of the {002} spacings in the ZOLZ gave a unit cell dimension of 10.54 Å, whilst measurement of the FOLZ diameter gave a unit cell cell dimension of 10.8 Å. These values compare well with the tabulated data of Pearson's Handbook [7], which quotes the unit cell dimensions of the $(CrFe)_{23}C_6$ phase as 10.59 Å and the $(CrFeMo)_{23}C_6$ phase as 10.65 Å.

Figure (8a) shows the x-ray spectrum obtained from the Ti(Nb)CN precipitate shown in figure (7a). Such x-ray spectra revealed an average composition of Ti-1.8at%Nb with trace quantities of Cr, Al and Si. The presence of C and N was confirmed by EELS. Figure (8b) shows the diffraction pattern obtained from the Ti(Nb)CN precipitate in the [001] orientation. The lattice parameter was determined ,from the radius of the FOLZ to be 4.3 Å. This was slightly smaller than the lattice parameter of the non Nb-containing Hägg phase observed in the AM alloy. Figure (8c) shows the angular morphology of a second Ti(Nb)CN precipitate, 1500 Å in length. The corresponding diffraction pattern, also from the [001] zone axis, is shown in figure (8d) using a long camera length. A summary of the precipitates observed in the VAR 4340 alloy steel is presented in Table II.

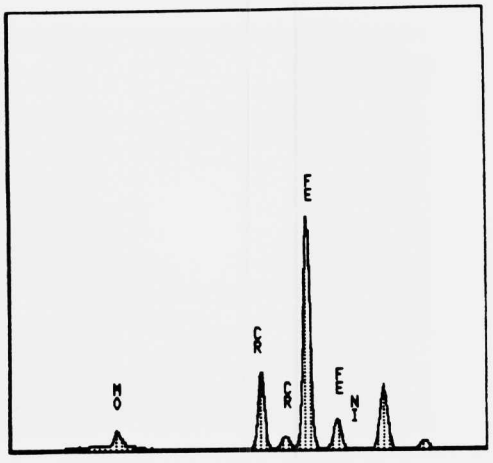

Fig.7c. X-ray spectrum from the $(FeCrMo)_{23}C_6$ precipitate shown in fig. 7a.

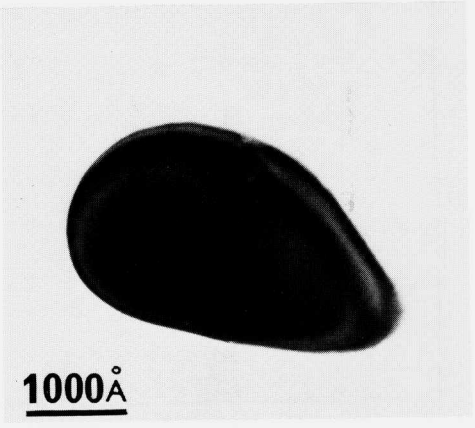

Fig.7d. Transmission electron micrograph of $(FeCrMo)_{23}C_6$ precipitate from VAR 4340 steel.

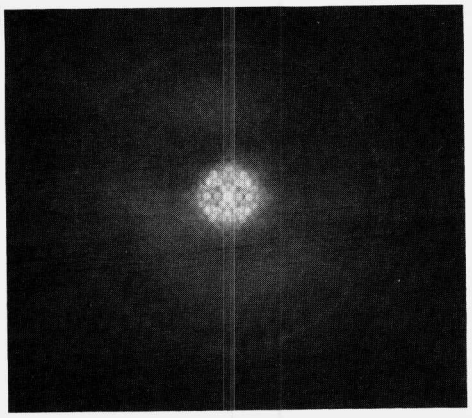

Fig.7e. CBED pattern from $(FeCrMo)_{23}C_6$ precipitate shown in fig. 7d, recorded at the [011] zone axis. The SOLZ ring may be seen at a reciprocal spacing of $2.75Å^{-1}$.

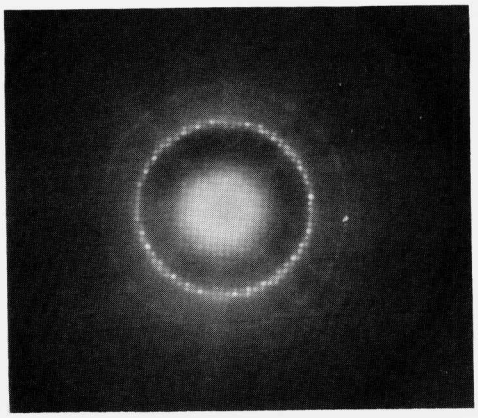

Fig.7f. CBED pattern from $(FeCrMo)_{23}C_6$ precipitate shown in fig. 7d, after tilting to the $[00\bar{1}]$ zone axis. The FOLZ ring may be seen at a reciprocal spacing of $2.33Å^{-1}$.

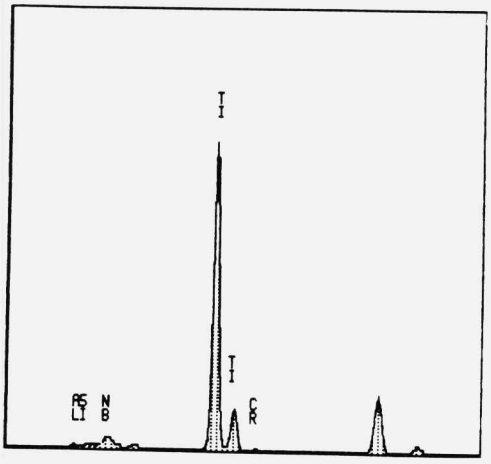

Fig.8a. X-ray spectrum obtained from the Ti(NB)CN precipitate shown in fig. 7a. The precipitate contained around 2 at%Nb.

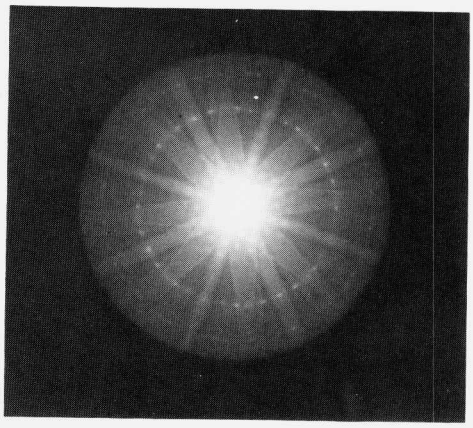

Fig.8b. CBED pattern at the [001] zone axis from the Ti(Nb)CN precipitate shown in fig. 7a. The FOLZ ring appears at a reciprocal spacing of 3.69 $Å^{-1}$.

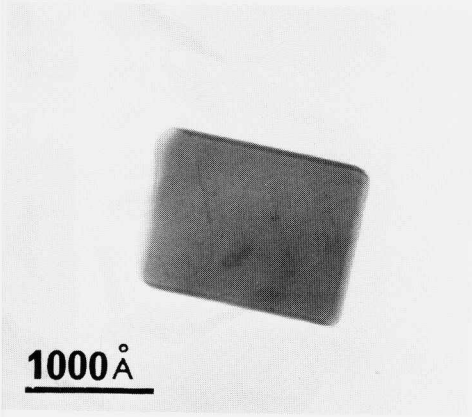

Fig.8c. Transmission electron micrograph showing the angular morphology of the Ti(Nb)CN precipitates.

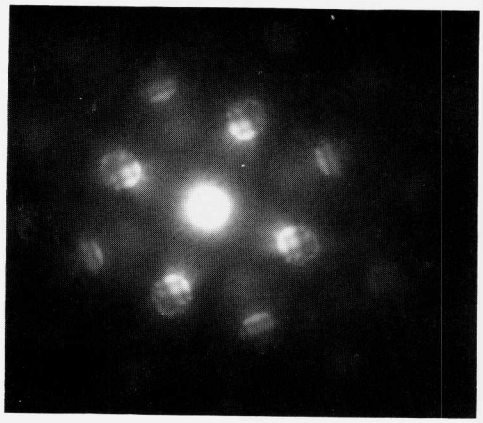

Fig.8d. CBED pattern recorded at the [001] zone axis with a long camera length from the Ti(Nb)CN precipitate shown in fig. 8c.

Rare Earth Processed Steel

Watton et al. [8], have examined the structure and properties of the rare earth modified Ni-Mo steel following consolidation at 1100°C. The addition of La to the Ni-Mo steel was found to achieve a K_{ISCC} level in excess of 22 MPa.$\sqrt{m}$. This was attributed to the successful gettering of P from the steel as a dispersion of sub-micron precipitates of $LaPO_4$. It is of interest to determine however, whether the La-P-O phase was formed during rapid solidification processing or during subsequent consolidation and processing of the powder.

The rare earth processed steel exhibited an average powder particle diameter of approximately 50 μm following RSP. The steel powder was found to be extremely difficult to examine due to the very different thinning rates for the steel and Ni matrix encountered during electro-chemical or ion-beam thinning. TEM of the Ni-Mo steel powder revealed La-P-O precipitates with a typical diameter of 200-500 Å. Figure (9a) shows a bright field micrograph of an La-P-O precipitate of 430 Å diameter within the lath-martensitic matrix of the steel. The x-ray spectrum produced by this particle is shown in figure (9b). The Fe and Ni peaks originated from broadening of the electron beam into the matrix, whilst the La and P peaks came from the precipitate.

An EEL spectrum from the matrix surrounding the particle (figure 9c) revealed, in addition to the low-loss plasmon peak, an Fe $M_{2,3}$-edge at around 54ev. The very low zero-loss to plasmon peak ratio indicates the extreme thickness of the matrix. An EEL spectrum from the precipitate itself (figure 9d) revealed a low-loss spectrum characteristic of lanthanum oxide with major low-loss peaks centered at 15 and 30ev, and a La $N_{4,5}$ edge centered at around 124ev [9]. At the high-loss end of the same spectrum, shown in figure (9e), Fe $L_{2,3}$ and La $M_{4,5}$ edges were observed. The thickness of the precipitate precluded the observation of O or P K-edges in the EEL spectrum and rendered quantitative analysis impossible.

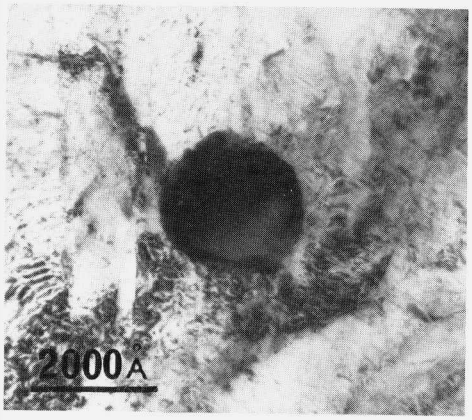

Fig.9a. Transmission electron micrograph of an La-P-O particle within the lath martensitic matrix of the RSP Ni-Mo steel.

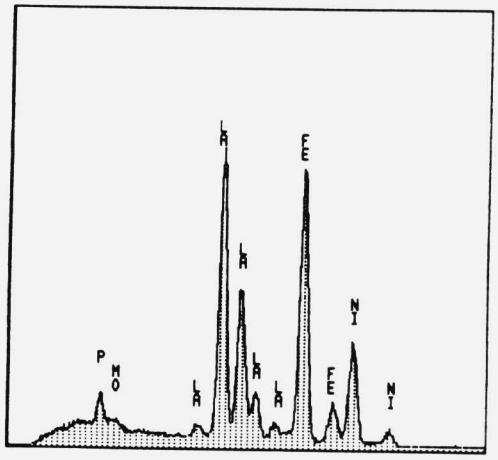

Fig.9b. X-ray spectrum from the La-P-O precipitate shown in fig. 9a. Analysis of the La and P peaks showed an La:P atomic ratio of approximately 5:1.

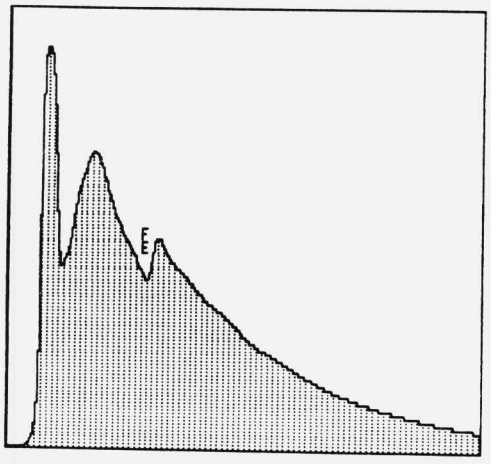

Fig.9c. EELS spectrum recorded from matrix surrounding the La-P-O precipitate in fig.9a. the spectrum shows the zero loss peak followed by a large plasmon peak and an Fe $M_{2,3}$-edge at around 54ev.

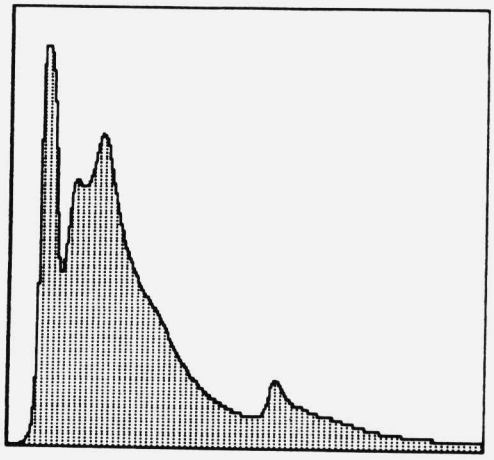

Fig.9d. Characteristic EELS spectrum recorded from the La-P-O precipitate shown in fig. 9a. Major low-loss peaks are centered at 15 and 30ev. A La $N_{4,5}$ edge appears at approximately 124ev.

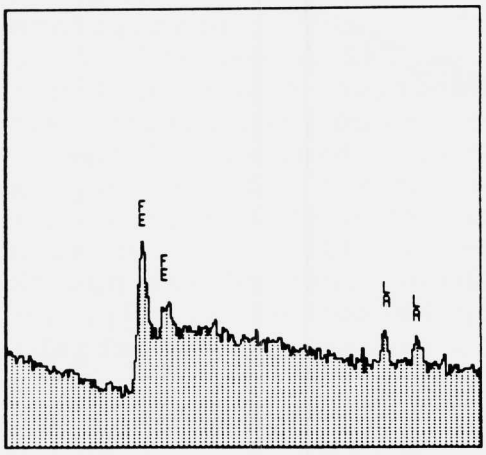

Fig.9e. High-loss region of EELS spectrum shown in figure 9d. Fe-$L_{2,3}$ (matrix) and La-$M_{4,5}$ edges (precipitate) are visible.

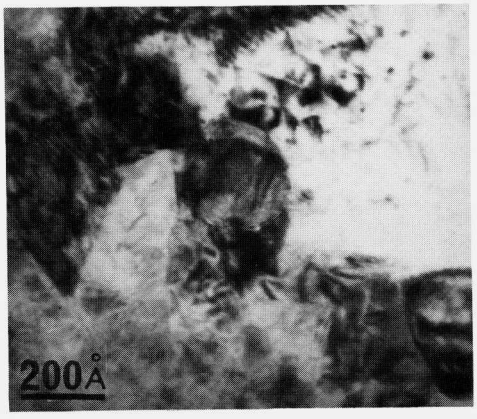

Fig. 10a. Bright field transmission electron micrograph showing a La-P-O precipitate in RSP Ni-Mo steel.

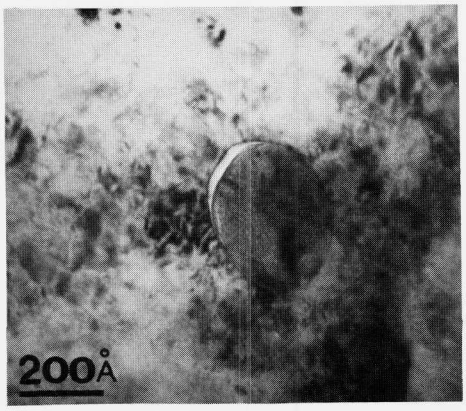

Fig. 10b. Bright field scanning transmission electron micrograph of La-P-O precipitate in RSP Ni-Mo steel.

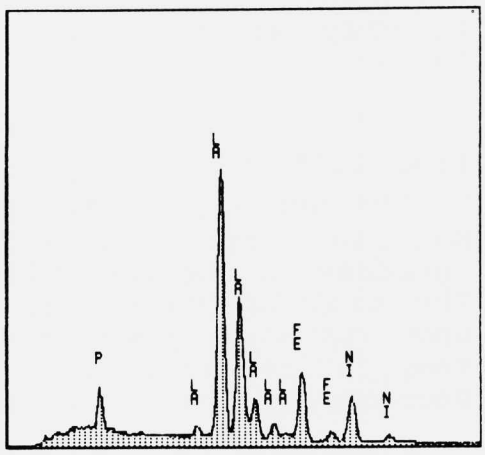

Fig.10c. X-ray spectrum recorded from La-P-O precipitate shown in fig.10b. Analysis of the La:P peak ratios revealed an atomic ratio of approximately 4:1.

Figures (10a and 10b) show TEM and STEM bright field images of two further La-P-O precipitates which exhibited diameters of 242 Å and 1500 Å respectively. The x-ray spectrum shown in figure (10c) was obtained from the second precipitate using a STEM probe of 20 nm diameter. Analysis of the La-to-P peak ratios revealed an atomic ratio of approximately 4:1. The high La:P ratio of the rare earth oxide precipitates examined in this limited study suggests that the La-P-O phase observed was not the expected $LaPO_4$.proposed by Watton et al [8], but rather La_2O_3 with the inclusion of a variable percentage of P.

Summary

The secondary particles responsible for the microvoid nucleation in stage I tempered UHS AM 4340 steel were AlN precipitates of approximately 500 Å diameter. The coalescence of microvoids gave rise to sheet microvoid failure in the shear tested specimens. Primary inclusions such as the MnS stringers observed in the AM alloys did not appear to play an important role in sheet microvoid failure.

An increase in the austenitizing temperature from 840°C to 1100°C resulted in a decrease in the number density of AlN precipitates by an order of magnitude from 5.10^{12} m^{-2} to 6.10^{11} m^{-2} and a 50% increase in the instability strain of the material. The diminishing effect of axial compressive load upon instability strain with increased austenitizing temperature was in good agreement with the observed decrease in precipitate density.

In the VAR 4340 steel the major secondary particle dispersion was found to be a complex intermetalic carbide, $(Fe_{.742}Cr_{.251}Mo_{.007})_{23}C_6$, of 1200 Å diameter and with a number density of 2 10^{11} m^{-2}. A minor component of 800 Å diameter TiNb(CN) precipitates was also observed with an order of magnitude lower number density. Despite the very different sizes and number densities of the precipitates in the 870°C austenitized VAR, and

840°C austenitized AM steels, a nearly identical instability strain was observed under conditions of linear shear. The $(FeCrMo)_{23}C_6$ and TiNb(CN) precipitates particles are therefore believed to be responsible for the microvoid nucleation underlying shear localization in the VAR steel.

The late addition of La to a modified Ni-Mo steel prior to rapid solidification processing was found to be successful in scavenging residual P from the steel in the form of a 200-500 Å diameter dispersion of spheroidal La-P-O precipitates. Subsequent compaction of the centrifugally atomized powder has produced a highly stress corrosion cracking resistant steel with a K_{ISCC} level in excess of 22 MPa.$\sqrt{m}$. The La addition has been shown to successfully getter P during the solidification process and the precipitates do not appear to have coarsened significantly during subsequent thermo-mechanical processing. The La addition would not appear to have formed the $LaPO_4$ phase expected by Watton et al. [8]. Instead, the distinctive low-loss EEL spectra and high La:P ratio indicate the precipitates to be essentially La_2O_3 with the inclusion of a variable percentage of P.

REFERENCES

1. G. B. Olson, "Conference Overview: Science of Steel", these proceedings.

2. C. J. McMahon Jr. and M. J. Morgan, "Impurity Segregation and Hydrogen Embrittlement in High Strength Steels", these proceedings.

3. M. Azrin, J. G. Cowie and G. B. Olson, "Shear Instability Mechanisms in High Hardness Steel", Annals of Israel Physical Society, 8 Fragmentation, Form and Flow in Fractured Media, 1986, pp.409-417.

4. J. G. Cowie, M. Azrin and G. B. Olson, "Microvoid Formation During Shear Deformation of Ultrahigh Strength Steels", these Proceedings.

5. The Bristol Group. Convergent Beam Electron Diffraction of Alloy Phases, 1984, Bristol, Adam Hilger.

6. H. J. Goldschmidt. Interstitial Alloys, 1967, London, Butterworth.

7. W. B. Pearson. A Handbook of Lattice Spacings and Structure of Metals and Alloys, 1958, London, Pergamon Press, pp 926-927.

8. J. F. Watton, G. B. Olson and M. Cohen, "A Novel Hydrogen-Resistant UHS Steel", these proceedings.

9. C. C. Ahn and O. L. Krivanek, A Catalog of Energy Loss Spectra, 1982, Arizona State University, HREM Facility, Tempe.

ACKNOWLEDGEMENTS

This work was supported by the Harvard Materials Research Laboratory under NSF Grant DMR-86-14003 as part of the Steels Research Group (SRG). Discussions with G. Olson, J. W. Hutchinson and F. Spaepen throughout this work are greatly appreciated. The AM, VAR and RSP steel samples were kindly provided by J. G. Cowie, M. Gore and M. Libera respectively. The technical assistance of Y.Z. Lu is gratefully acknowledged.

SOLUTION TREATMENT EFFECTS IN AF 1410 STEEL

MICHAEL SCHMIDT*[1], MARK GORE[2]
(1) Tool and Alloy R&D, Carpenter Technology Corp., Reading, Pennsylvania, 19612-4662; (2) Department of Materials Science, Massachusetts Institute of Technology, Cambridge, Massachusetts, 02139.

INTRODUCTION

Presently, a ferrous-base high strength/high toughness alloy does not exist which exhibits 55-60 HRC and 60-120 ksi $\sqrt{in.}$ Such an alloy, if it existed, could be used extensively in defense-related programs to produce support and structural components for aircraft and aerospace vehicles and possibly in the fabrication of armor components. Recognizing the need for such a material the National Science Foundation (NSF) has awarded a grant to the Massachusetts Institute of Technology (MIT) to develop a martensitic steel with the previously described strength and toughness levels.

The personnel involved in this "Innovations in High Strength Steel Technology" program believe that the program objectives can be achieved by modifying the composition of AF 1410 (nominal composition: 0.16% C, 14% Co, 10% Ni, 2% Cr, 1% Mo, balance Fe). This alloy is a high strength (48-50 HRC), high fracture resistant (150+ ksi $\sqrt{in.}$) steel developed by Little and Machmeier(1,2) for use in highly stressed airframe structural components. Presently, this alloy is being used in the manufacture of the arrestor hook landing mechanism for carrier-based F-18 aircraft.

By increasing the carbon content and rebalancing the level of M_2C carbide formers in AF 1410, it is believed that the strength of this alloy can be increased to 55-60 HRC while still maintaining a relatively high level of toughness (60-120 ksi $\sqrt{in.}$). Additionally, it is envisioned that the use of austenitizing temperatures in excess of 1525°F - the temperature used for the standard commercial version of AF 1410 - may impart improved toughness to the modified alloys to be evaluated in this program by reducing the number of sub-micron size microvoid nucleating particles. The purpose of this work is to characterize the effects of austenitizing temperature on the mechanical properties and microstructure of AF 1410.

MATERIALS AND METHODS

Material representing a standard commercial lot of AF 1410 in the normalized (1650°F-1h, AC) and overaged (1250°F-6/8h, AC) condition was used for this study. This material was melted using standard VIM/VAR practices and was rotary forged to 4-5/8" rd. bar prior to normalizing and over-aging. The composition of this particular lot of AF 1410 (0.166 C, 0.02 Mn, 0.02 Si, 0.001 S, 0.003 P, 2.04 Cr, 10.15 Ni, 1.04 Mo, 14.16 Co, balance Fe) is typical for this product.

The effect of austenitizing temperature on the austenetic grain size was evaluated using Riedl's technique. The longitudinal surface from representative 1/2" cube samples was metallographically prepared. These samples were then placed with the polished face up in an open atmosphere furnace and austenitized at 1500, 1525, 1550, 1575 or 1625°F for 1 or 3 hours and oil quenched. The heat treat oxide was carefully removed from the previously polished surface using 600 grit SiC prior to metallographic preparation. All samples were lightly etched with 2% Nital and the grain size was evaluated using the Snyder-Graff intercept method(3). The average Snyder-Graff intercept grain size was then converted to an ASTM grain size using the equation below, and these data were plotted as a function of austenitizing temperature.

$$\text{ASTM G.S.} = [6.635 \log(\text{Avg. S-G})] + 2.66$$

The effect of austenitizing temperature on the as-quenched hardness and microstructure was evaluated. Representative 1/2" cube samples were austenitized in a neutral salt bath at 1500, 1525, 1550, 1575 or 1625°F for 1 or 3 hours and oil quenched. Rockwell hardness readings were taken and the average of these test results was plotted versus austenitizing temperature. Microstructures were examined using optical and electron microscopy techniques. The transmission electron microscopy work was performed using MIT's JEOL 200 CX TEM and Vacuum Generators HB5 STEM and Carpenter Technology Corporation's Philips EM 420T TEM/STEM. The levels of retained austenite were also determined in each of the as-quenched specimens. This work was performed on a General Electric XRD5 x-ray diffraction unit using V filtered Cr-K_α radiation and the direct comparison method(4).

The effect of austenitizing temperature on the aging behavior of AF 1410 was also examined. Representative 1/2" cube samples were austenitized in neutral salt at 1525 or 1625°F for 1 or 3 hours and oil quenched to room temperature, were deep frozen at -100°F for 1 hour in a solution of dry ice and methanol and were then aged at 850, 900, 950 or 1000°F for 5 hours. The average Rockwell hardness data were plotted as a function of aging temperature for each of the investigated austenitizing parameters. The microstructure and levels of reverted austenite present in samples aged at 950°F for 5 hours were also evaluated using TEM and x-ray diffraction techniques, respectively.

The effects of austenitizing temperature on the tensile properties and Charpy V-notch impact toughness of material in the 950°F-5 hour aged condition were evaluated. Representative longitudinal specimen blanks (Charpy specimen blanks were removed from the L-C orientation) were removed from the mid-radius bar location, rough machined, heat treated, finish machined and tested at room temperature. Heat treating entailed austenitizing in neutral salt at 1500, 1525, 1550, 1575 or 1625°F for 1 or 3 hours and oil quenching to room temperature followed by deep freezing to -100°F and aging at 950°F. The average test data were plotted as a function of austenitizing temperature.

RESULTS AND DISCUSSION

As-Quenched Behavior

The data contained in Figure 1 show that the grain size of AF 1410 is rather insensitive to variations in austenitizing temperature within the investigated temperature range. For example, the grain size of material soaked at temperature for 1 hour changes from an ASTM 11.4 to 10.7 when the austenitizing temperature is increased from 1525 to 1625°F. In addition, the plots contained in Figure 1 indicate that a trend of slightly coarser grain size is associated with a 3 hour versus a 1 hour soak during austenitizing; however, this trend was not statistically significant at a confidence level of 95%.

An inverse linear relationship exists between the as-quenched hardness of AF 1410 and the range of austenitizing temperatures that were investigated (Figure 2). Correlation coefficients of -0.9590 and -0.9825,

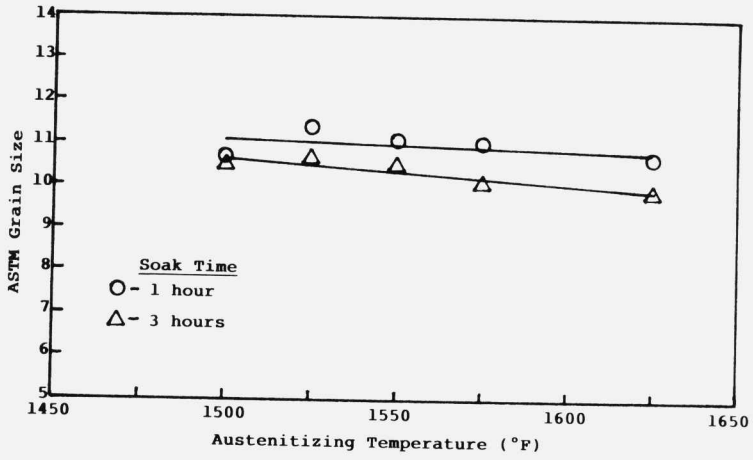

FIGURE 1. Plots of ASTM grain size versus austenitizing temperature (°F) for AF 1410.

respectively, were obtained for the least squares fit of the data points representing 1 and 3 hour soaks. The plots contained in Figure 2 show that the observed inverse linear relationship becomes more pronounced as the soak time is increased from 1 to 3 hours. For example, a 50°F increase in austenitizing temperature resulted in a decrease of approximately 1 HRC for material soaked at temperature for 1 hour; whereas, a similar increase in austenitizing temperature used in conjunction with a 3 hour soak resulted in a 2.5 HRC decrease in as-quenched hardness.

In an attempt to identify the mechanism responsible for the behavior depicted in Figure 2, the levels of retained austenite were determined using standard x-ray diffraction techniques and the general microstructure and fine structure were evaluated using optical and electron microscopy, respectively. The x-ray diffraction work revealed that regardless of the austenitizing parameters used, no retained austenite was detected in the samples of AF 1410.

Optical photomicrographs detailing the as-quenched microstructure of AF 1410 appear in Figure 3. This series of photomicrographs shows that the low-carbon, lath martensitic structure becomes more clearly delineated and that some coarsening of the packet and block structure occurs as the austenitizing temperature is increased from

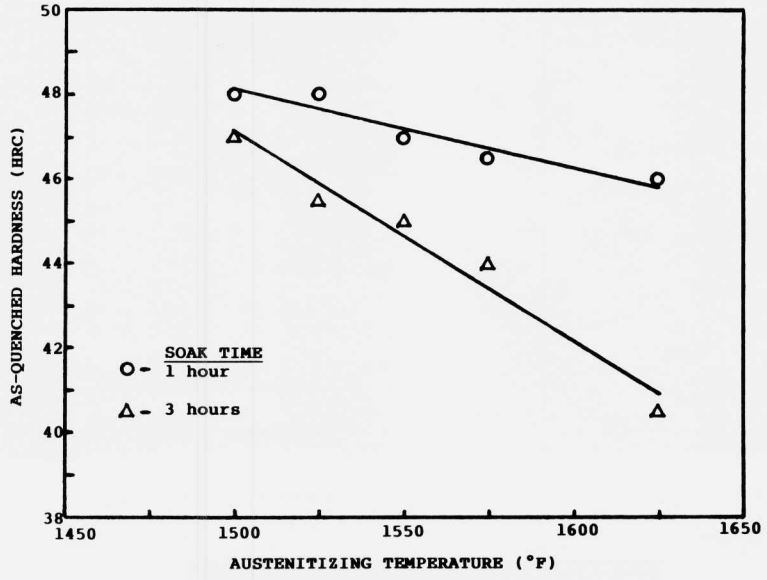

FIGURE 2. Plots of as-quenched hardness versus austenitizing temperature (°F) for AF 1410.

1525 to 1625°F. It is believed that these changes are not sufficient to promote the trend between as-quenched hardness and austenitizing temperature that is depicted in Figure 2.

Examination of extraction replicas and thin foil specimens, representing as-quenched structures, using TEM/STEM revealed that a distinct variation exists between the type of carbides present in material austenitized at 1625°F versus 1525°F. For example, nearly spherical carbides in the 40-200 nm size range were observed in material austenitized at 1525°F for 1 hour (Figure 4). Energy dispersive spectroscopy (EDS) revealed that the larger carbides (90-200 nm) were enriched in Cr and Fe and contained small but significant amounts of Mo (68% Cr, 24% Fe, 8% Mo); whereas, the smaller carbide structures (40-80 nm) were enriched in Mo and contained some Cr (85% Mo, 14% Cr, 1% Fe) or were enriched in Mo and Ti (53% Mo, 43% Ti, 4% Fe). Convergent beam electron diffraction patterns (CBDP) revealed that the larger Cr-rich particles were M_6C carbides and that the smaller Mo and Mo/Ti-rich particles were MC carbides. In contrast,

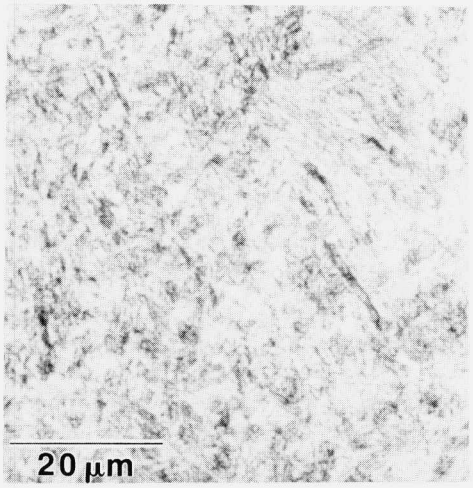

(a) 1525°F - 3h, OQ

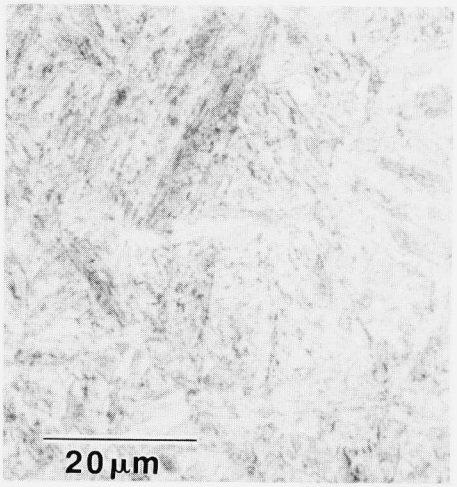

(b) 1575°F - 3h, OQ

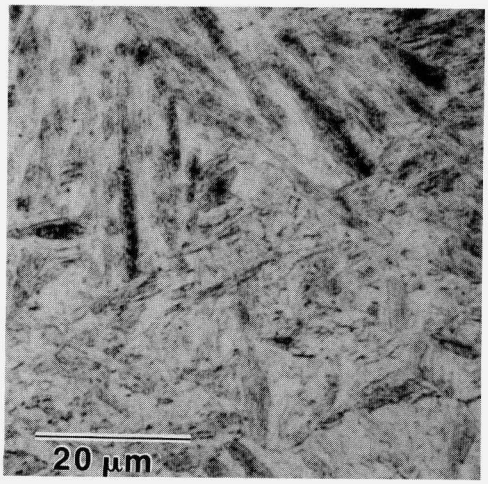

(c) 1625°F - 3h, OQ

FIGURE 3. Optical photomicrographs showing the effect of austenitizing temperature on the as-quenched microstructure of AF 1410. Samples were etched with 25% Nital for 5-10 sec. followed by Vilella's reagent for 10 sec.

the material austenitized at 1625°F for 1 hour contained numerous intralath rod-like carbides displaying a Widmanstatten distribution (Figure 5). These carbides were determined to be enriched in Fe, Ni and Co and ranged in size from 20/40 nm in width x 100/250 nm in length. Based

on the composition and morphologies of these carbide structures, it is believed that the spheroidal carbides shown in Figure 4 are the result of incomplete carbide solutioning when austenitizing at 1525°F; whereas, the particles shown in Figure 5 are an alloyed M_3C that formed via auto-tempering.

The presence of the auto-tempering phenomenon being associated with the use of the higher austenitizing temperature does offer an explanation for the inverse relationship between as-quenched hardness and austenitizing temperature that is shown in Figure 2. The formation of auto-temper carbides will result in a tempered lath martensite of a lower hardness level being substituted for an as-quenched lath martensitic structure. As the volume fraction of the former is increased, the as-quenched hardness will decrease. While auto-tempering does offer an explanation for the inverse relationship observed between as-quenched hardness and austenitizing temperature, it can not explain the effect observed in the test data with regard to soak time. Presently, no explanation can be offered for the effect that increasing soak time has on the rate of decrease in the as-quenched hardness with increasing austenitizing temperature.

The auto-tempering condition that was observed with the use of a 1625°F austenitizing temperature suggests that the M_s temperature of AF 1410 is affected by variations in austenitizing temperature. One would suspect intuatively that the M_s temperature should decrease as Cr-rich M_6C carbides are dissolved through the use of increased austenitizing temperatures since both Cr and C are known to suppress the M_s temperature. Therefore, additional work is planned to evaluate the effects of austenitizing temperature and quench practice on the M_s temperature of AF 1410.

Aging Behavior

Aging curves representing material austenitized at 1525 or 1625°F for 1 or 3 hours are plotted in Figure 6. This work was performed in order to determine if changes in the austenitizing cycle of AF 1410 produce significant changes in the aging characteristics of the alloy. The data contained in Figure 6 show that increased austenitizing temperature and time do not result in any apparent horizontal shifts in the aging curve of AF 1410. This observation would indicate that when aging for 5 hours, peak aged hardness occurs in the 850/900°F

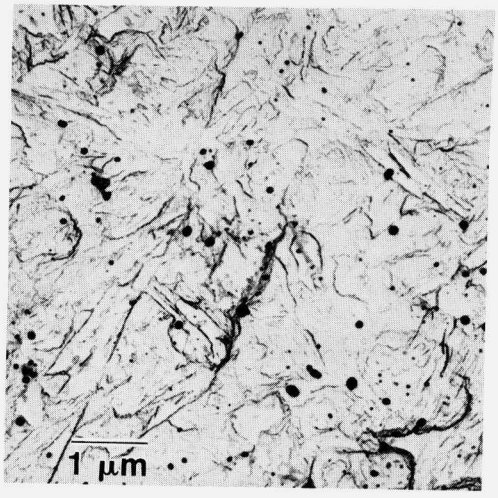

FIGURE 4. TEM photomicrograph of an extraction replica showing the carbides observed in AF 1410 following a 1525°F-1h, OQ treatment.

temperature range regardless of whether the alloy is austenitized at 1525 or 1625°F for either 1 or 3 hours.

The data in Figure 6 do indicate that a downward vertical shift in the aging curve of AF 1410 does occur as the austenitizing temperature and/or time are increased. In particular the effect of time becomes more pronounced when used in conjunction with the 1625°F austenitizing temperature. These data would therefore tend to indicate that AF 1410 becomes more sensitive to soak time as the austenitizing temperature is raised above 1525°F. This same effect of increased time sensitivity with increasing austenitizing temperature was also observed in the as-quenched hardness data (Figure 2).

The downward vertical shift in aging response that is apparent in Figure 6 as the austenitizing temperature and time are increased can not be attributed to the auto-tempering phenomenon that was observed in the as-quenched material. The tempering sequence reported by Speich et al.(5) for AF 1410 type alloys is $M_3C \rightarrow M_2C$ with the M_3C phase dissolving around 800°F and precipitation of M_2C occurring in the 800-1000°F temperature range. Thus, the presence of M_3C auto-temper carbides in the as-quenched structure should not reduce the peak aged hardness of the

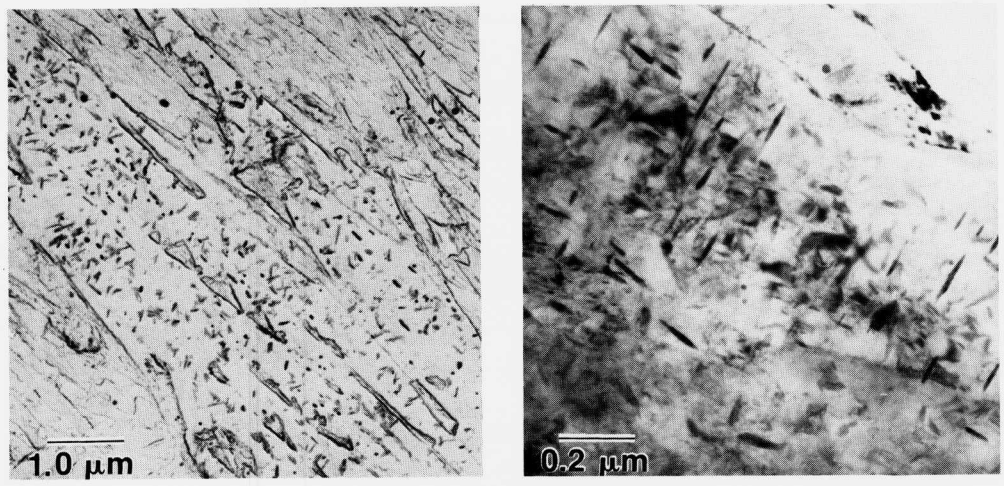

(a) extraction replica (b) thin foil

FIGURE 5. TEM photomicrographs showing the presence of auto-temper carbides in AF 1410 following a 1625°F-1h, OQ treatment.

material based on the fact that the M_3C phase dissolves.

Examination of aged microstructures representing the 950°F-5 hour condition using optical microscopy revealed findings similar to those observed in the as-quenched condition. In effect, the only significant trend that could be observed was an increase in the size of the packet and block structure of the lath martensite, and it is believed that this condition by itself would not produce the downward vertical shifts in the aging curve of AF 1410 that are shown in Figure 6.

Initially it was believed that increased levels of reverted austenite might be responsible for the reduction in aged hardness that accompanies increased austenitizing temperatures and times. However, the x-ray diffraction data contained in Table 1 show that increased levels of reverted austenite are not found in the 950°F-5 hour aged condition as the austenitizing temperature and time are increased within the range of conditions that were studied. In general, these data show a trend of decreased reverted austenite being associated with an austenitizing temperature of 1625°F versus 1500°F; however, it should be noted that the variations in reverted austenite reported in

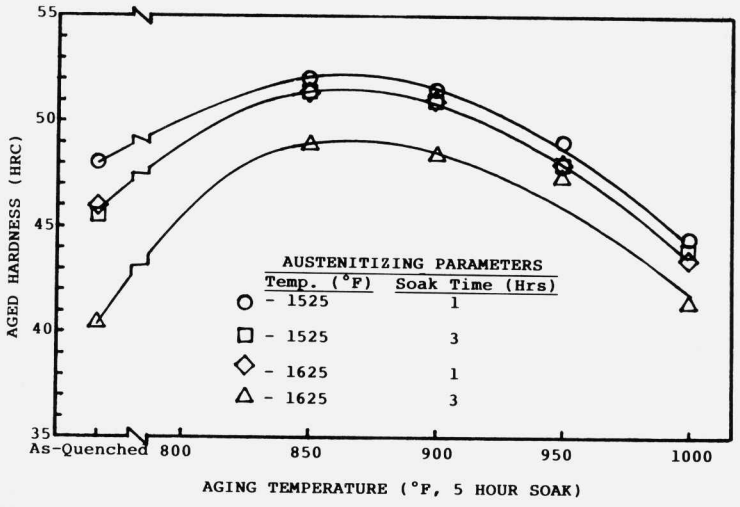

FIGURE 6. Plots of aged hardness versus aging temperature for AF 1410 austenitized as indicated.

TABLE 1

REVERTED AUSTENITE PRESENT IN AF 1410*

Austenitizing Temperature (°F)	Soak Time (hr.)	Volume % Reverted Austenite+
1500	1	5
1500	3	6
1525	1	4
1525	3	3
1550	1	3
1550	3	5
1575	1	3
1575	3	3
1625	1	3
1625	3	2

* Determined following a 950°F-5 hour age.
+ Determined using standard x-ray diffraction techniques.

Table 1 are not statistically significant.

Examination of the fine structure of material aged at

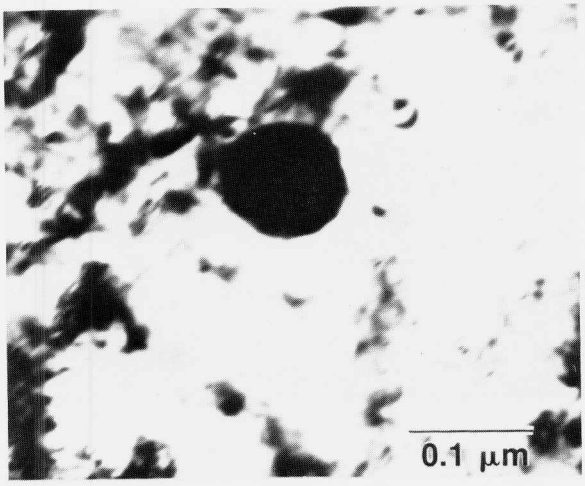

FIGURE 7. Bright field TEM photomicrograph showing a large undissolved carbide present in AF 1410 following austenitizing at 1525°F for 1 hour and aging at 950°F for 5 hours.

950°F for 5 hours following austenitizing at 1525°F for 1 hour using thin foil specimens and bright field imaging in the TEM revealed the presence of large ($\approx$0.1 μm) spherical incoherent carbides in addition to the strain contrast effects which probably are the result of coherent M_2C carbide precipitation (Figure 7). These former structures are identical in appearance to the remnant, undissolved carbides observed in the as-quenched condition (Figure 4), and it should be recalled that EDS and CPDP analysis of these carbides revealed that they were Cr-rich M_6C. Work by Speich et al.(6) has shown that the presence of increased Cr in AF 1410 type alloys promotes an increase in the coarsening of the M_2C carbide phase. Since this phase is responsible for the strong secondary hardening response in AF 1410, an increase in matrix Cr, as the result of the dissolution of undissolved carbides by increasing the austenitizing temperature, has resulted in coarser M_2C carbides (Figure 8), which in turn, would account for the behavior shown in Figure 6.

The results of the mechanical property testing are plotted as a function of austenitizing temperature in

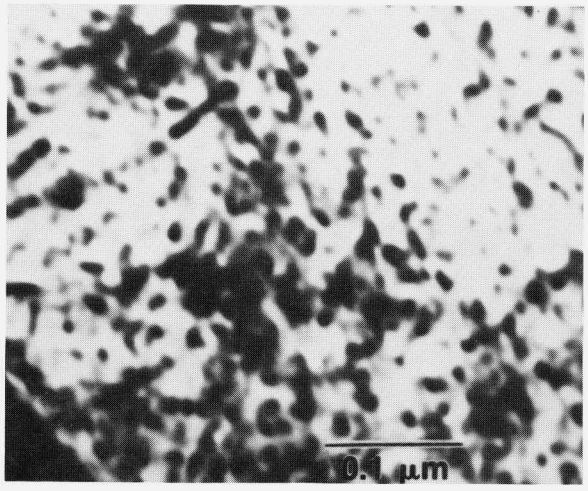

Figure 8. Bright field TEM photomicrograph showing the presence of coarse M_2C precipitates in AF 1410 austenitized at 1625°F for 1 hour followed by aging at 950°F for 5 hours.

Figure 9. These plots clearly show that austenitizing temperature and time have similar effects on both the 0.2% offset yield and ultimate tensile strengths of AF 1410. For example, material austenitized at temperature for 1 hour attains peak strength when aged at 950°F for 5 hours when an austenitizing temperature of 1525°F is used. For austenitizing temperatures greater than 1525°F both the yield and tensile strengths decrease. As the austenitizing time is increased to 3 hours both the yield and tensile strength levels are reduced on the average by 9.9 and 7.7 ksi, respectively. Additionally, material austenitized at temperature for 3 hours attains peak strength levels in the 950°F-5 hour aged condition when an austenitizing temperature of 1500°F is used.

Based on the observations made in the previous paragraph, it is clear that an inverse relationship exists between the yield and ultimate tensile strengths and the variables of austenitizing temperature and time. Close examination of the yield strength and ultimate tensile strength plots in Figure 9 shows that the spread between these two properties appears to increase as the austenitizing temperature is increased. The difference between the ultimate tensile and yield strengths is plotted

versus austenitizing temperature in Figure 10. These data show an extremely strong positive correlation (correlation coefficients of 0.9857 and 0.9565, respectively, for the data representing 1 and 3 hour soaks) between the spread in the yield and the tensile strengths and austenitizing temperature. The parallel nature of the plots representing 1 and 3 hour soaks suggests that soak time during austenitizing does not have an effect on the spread between the yield and tensile strengths of AF 1410 that is observed following a 950°F-5 hour age.

The reduction in both the yield and tensile strengths with increasing austenitizing temperature and time reinforces the observations made with respect to the effects these same variables have on the aged hardness of AF 1410 (recall the data in Figure 6). Based on the nearly parallel trends shown for aged hardness in Figure 6 and aged strength in Figure 9, it is believed that the same mechanism which was postulated to explain the effects shown in Figure 6 is responsible for the behavior shown by the yield and tensile strength data that are plotted in Figure 9.

With regard to tensile ductility and impact toughness, the data contained in Figure 9 generally show that increases in both austenitizing temperature and time have a beneficial effect on these two properties. However, it is interesting to note that both temperature and time have more of an effect on the impact toughness of AF 1410. For example, the impact toughness is increased by approximately 14 ft.-lbs. as the austenitizing temperature is raised from 1525 to 1575°F when using either a 1 or 3 hour soak, and increasing the austenitizing time from 1 to 3 hours within this same temperature interval resulted in a 12 to 15 ft.-lb. improvement. Analysis of the %RA test data showed that typical improvements on the order of approximately 3% were achieved for comparable changes in austenitizing temperature and time. The data in Figure 9 show that austenitizing temperatures in excess of 1575°F result in diminishing improvements in both tensile ductility and impact toughness when a 1 hour soak is used, and that both properties are reduced when a 3 hour soak is used in conjunction with an increase in austenitizing temperature from 1575 to 1625°F.

The grain size trends that were previously discussed (Figure 1) are not sufficient enough to explain the toughness and ductility trends shown in Figure 9. However,

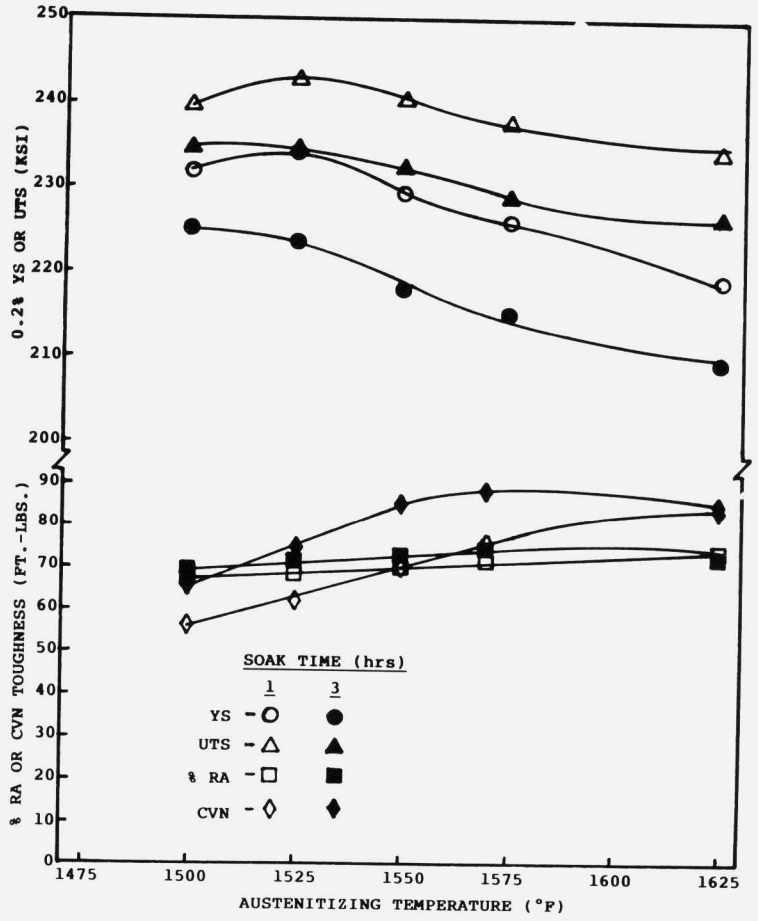

FIGURE 9. Plots of the longitudinal, room temperature mechanical properties of AF 1410 in the 950°F-5 hour aged condition versus austenitizing temperature.

a possible explanation for the observed increase in the tensile ductility and impact toughness as the austenitizing temperature and time are increased can be formulated based on the effect that these heat treating parameters have on the volume fraction of undissolved, sub-micron sized carbides. These carbides can act as microvoid nucleation sites during the fracture initiation stage associated with a tensile or impact test. Thus, by reducing the number of these undissolved carbides as the result of increasing either the austenitizing temperature or time, the number of microvoid nucleating sites can be reduced and the average interparticle spacing can be increased, which in turn can

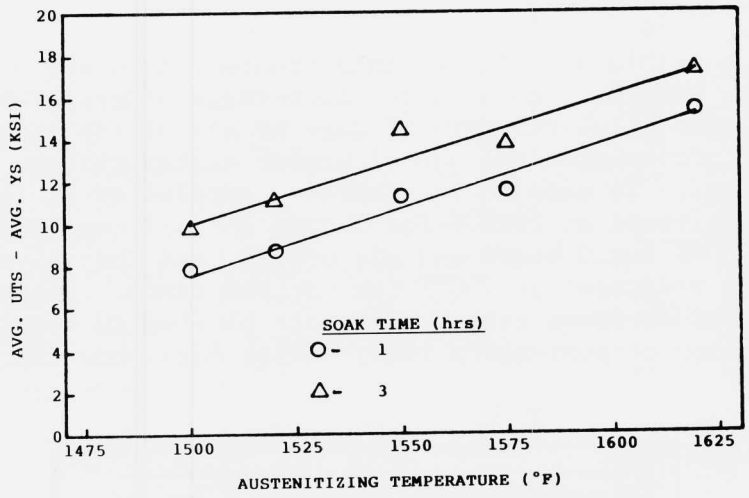

FIGURE 10. Plots of the spread between the longitudinal, room temperature yield and ultimate tensile strengths of AF 1410 following a 950°F-5 hour age versus austenitizing temperature.

reduce possible interparticle interactions and can also increase the energy required for the nucleated micovoids to link up. These changes in turn can result in larger initiation and propagation energies during the fracture process. This explanation is quite consistent with work performed by Garrison and Moody(7) on the effect of inclusion spacing on the fracture toughness of 4340 type alloys and AF 1410. At present, an explanation can not be offered for the reduction in tensile ductility and impact toughness that occurs when the austenitizing parameters are changed from 1575°F-3 hours to 1625°F-3 hours.

Post Aging of AF 1410

There is increasing evidence that the mechanical properties, particularly the toughness, of high-strength materials are controlled by nucleation of microvoids on sub-micron particles present in the material. Thus, for improved K_{IC} and Charpy V-notch impact toughness, it would be desirable to exploit the ability of high austenitizing temperatures to reduce the number of microvoid nucleating particles (recall Figure 4 versus Figure 5a) in AF 1410. However, as shown by Figure 9, the use of higher austenitizing temperatures is accompanied by a slight

decrease in strength.

One possible solution to this problem is to use a post-aging treatment to promote short-range ordering which in turn, will allow recovery of some or all of the strength loss that accompanies the use of higher austenitizing temperatures. To examine this effect, samples of AF 1410 were austenitized at 1625°F for 1 hour and oil quenched, aged at 950°F for 5 hours and air cooled, and then given a post-aging treatment at 750°F for various times. Diamond pyramid microhardness test results are plotted in Figure 11 as a function of post-aging time. These data show that

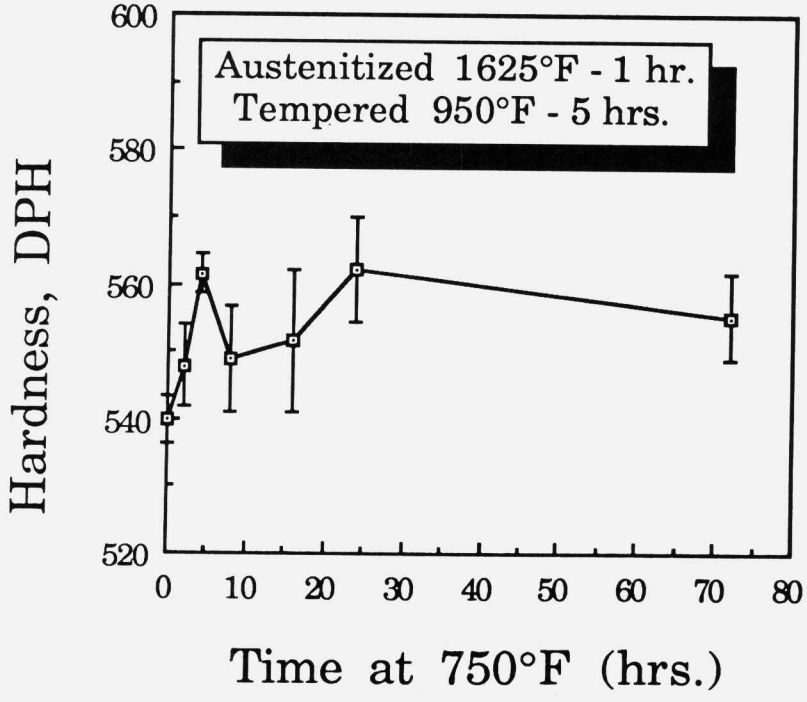

FIGURE 11. Plot of hardness versus aging time at 750°F for AF 1410 heat treated as indicated.

hardness increases of over 20 DPH are possible after a 4 hour post-age at 750°F. Thus, the use of post-aging treatments to achieve order-hardening appears promising for regaining the strength and hardness that was lost due to the use of a higher austenitizing temperature. However, more work is necessary to determine the optimum time and

temperature required for this post-aging treatment and to determine the effect(s) of this treatment on the K_{IC} and Charpy V-notch impact toughness of AF 1410.

SUMMARY

Increasing the austenitizing temperature from 1500/1525°F to 1625°F results in slight coarsening of the packet and block structure of the lath martensite; increased dissolution of sub-micron sized Cr-rich M_6C carbides; a decrease in as-quenched hardness, aged hardness and aged strength; the formation of M_3C auto-temper carbides; an increase in tensile ductility and Charpy V-notch impact toughness; and an increase in the spread between the yield and ultimate tensile strengths. The reduction in as-quenched hardness is believed to be the result of auto-tempering; whereas, the reductions in 950°F aged hardness and strength are probably caused by increased solutioning of Cr-rich M_6C carbides which accelerates the coarsening of M_2C carbides. Preliminary work indicates that a post-aging treatment at 750°F, which promotes short-range order, may be useful in recovering the strength loss associated with higher austenitizing temperatures. The improvements in tensile ductility and impact toughness are probably related to a reduction in the volume fraction of void nucleating sub-micron size carbides.

ACKNOWLEDGEMENTS

The authors would like to express their sincere gratitude to the management at Carpenter Technology Corporation for their support of this research program; to Mrs. B. Messersmith for the austenite determinations; to Mr. R. Razzano for performing the mechanical testing; to Mr. G. Haidemenopolos from MIT and Dr. R. Mahidhara for the TEM/STEM analysis, to Mr. D. Englehart for general services; to Dr. G. Olson from MIT and R. Hemphill for the many hours of thought provoking discussion pertaining to the data generated in this study; and to Mrs. D. Dunkelberger and Mrs. D. Heckman for their aid in the preparation of this manuscript.

REFERENCES

1. P. M. Machmeier, et al. "Development of a Strong

Martensitic Steel Having Good Fracture Toughness," Metals Technology, August 1979, p. 291.

2. C. D. Little and P. M. Machmeier, "High Strength Fracture Resistant Weldable Steels," United States Patent 4,076,525, February 28, 1978.

3. G. F. Vander Voort, Metallography Principles and Practice, 1st ed. New York, NY, McGraw-Hill Book Co., 1984, pp. 458-460.

4. B. D. Cullity, Elements of X-Ray Diffraction, 2nd ed. Reading, Mass. Addison-Wesley, 1978, pp. 411-415.

5. G. R. Speich, et al. "Strength and Toughness of Fe-10 Ni Alloys Containing Carbon, Chromium Molybdenum and Cobalt," Met.Trans., Vol. 4 (1973), pp. 304.305.

6. Ibid, p. 314.

7. W. M. Garrison and N. R. Moody, "The Influence of Inclusion Spacing and Microstructure on the Fracture Toughness of the SEcondary Hardening Steel AF 1410, "Met. Trans., Vol. 18A (1987), p. 1257.

GRAIN-REFINING DISPERSIONS AND PROPERTIES IN ULTRAHIGH-STRENGTH STEELS

MARK J. GORE*, GREGORY B. OLSON*, and MORRIS COHEN
Massachusetts Institute of Technology
Department of Materials Science and Engineering
Cambridge, Massachusetts 02139

*now at: Northwestern University
Department of Materials Science and Engineering
Evanston, Illinois 60208

INTRODUCTION

The complex interplay between structure, properties, and processing forms the central concern of materials science. Better understanding of this interplay has lead to the advent of "clean steel" technology, which dramatically reduced the volume fraction of the large (>1μm) inclusion particles in ultrahigh-strength martensitic steels. As such, the detrimental effect of these "primary" inclusions on the mechanical properties, particularly toughness and ductility, has been considerably reduced. It now appears that *microvoid* nucleation on the *submicron* "secondary" dispersions can limit the toughness and ductility of many high-strength structural materials under certain conditions[1]. These "secondary" dispersions, such as carbides, are the direct result of the processing history of the material and should be controllable through better understanding and control of the processing.

At first glance it might appear desirable to strive for the complete elimination of these submicron particles to remove potential microvoid nucleation sites. These fine particles, however, pose an interesting metallurgical paradox, being at the same time beneficial and detrimental to attaining the optimum mechanical properties in a material. It is well established that second-phase particles serve to pin migrating grain boundaries, maintaining the fine grain sizes desirable for good toughness and ductility[2]. It is, however, these same *submicron* grain-refining particles which can initiate *microvoids*, limiting the fracture toughness of the material. Thus, it is important to quantify and characterize these submicron secondary dispersions and examine their response to processing and thermal treatments in order to gain insight into achieving optimum properties in this important class of materials.

In the interest of enhancing the toughness of these steels it is necessary to make these grain-refining dispersions as resistant to the processes of microvoid

nucleation as possible. Recent modeling of the microvoid nucleation phenomenon suggests it is desirable to minimize both the size and volume fraction of the dispersion[3,4]. Also, selection of the composition of the grain-refining dispersion should be made so as to maximize the interfacial strength with the matrix in order to delay the debonding of the interface. Enhancement in the microvoid nucleation resistance of the grain-refining dispersion must be accomplished without compromising the grain-refining effectiveness.

The ability of second-phase particles to pin migrating boundaries was first quantitatively analyzed by Zener[2]. Numerous models have expanded upon this idea which predict a limiting grain size for a material containing a second-phase dispersion by establishing a static equilibrium between the driving force for boundary migration and the pinning force offered by the particle[2,5,6]. The grain size is found to be proportional to the ratio $\bar{d}/f_v$, where $\bar{d}$ is the average particle size and f_v is the volume fraction. These models would suggest there is no loss in the grain-refining ability of a dispersion when the necessary size and volume fraction reductions are made that enhance microvoid nucleation resistance, provided the same ratio of size to volume fraction is maintained. The obvious question, then, is how far can the necessary reduction in particle size, which enhances microvoid nucleation resistance, be pushed before the grain-refining ability of the dispersion is compromised.

Several factors will become important as the particle size is reduced which could impair the grain-refining ability of a dispersion. Certainly, these particles must have very high stability at the submicron size scale to resist both dissolution and Ostwald ripening. High stability dispersions assure grain refinement with a minimum volume fraction, which reduces their detrimental effect on toughness. Another possibility, reviewed extensively by Ashby[7], is the migrating boundary can drag the particles along with it through numerous mechanisms, reducing the pinning effectiveness and yielding a coarser microstructure. It appears that particle drag effects can again be minimized with highly stable dispersions. It is also quite possible that thermal activation effects could modify the pinning phenomenon as the particle size is reduced. Thermal activation could assist the boundary in unpinning from the particle, leading to a larger grain size. As such, the role of thermal activation in the grain coarsening process needs to be assessed. Hence, enhancement of microvoid nucleation resistance may not be as straightforward as a simple reduction in the size of the grain-refining dispersion, and must address the above effects.

EXPERIMENTAL

The submicron grain-refining dispersions were quantified in two ultrahigh-strength martensitic steels, 4340 and AF1410. The composition of each alloy is given in Table I. In order to study the effect of processing, the 4340 alloy was examined as produced by rapid solidification processing (RSP) and the more

traditional vacuum arc remelting (VAR). The RSP 4340 was produced by centrifugal atomization and the powder was "canned" in a mild steel container. Consolidation was accomplished through hot extrusion at 1100°C with an area reduction of 20:1. The AF1410 steel was processed using VAR. Both alloys were studied after an austenitizing (solution) treatment at a conventional temperature (CTA) and after austenitizing at higher than normal temperature (HTA). The solution treatment time for both alloys was 1 hour followed by an oil quench.

TABLE I
ALLOY COMPOSITIONS

Material	Cr	Ni	Mo	Co	Mn	Si	S	P	C
VAR 4340	.89	1.74	.21	-	.46	.28	.001	.009	.42
RSP 4340	.79	1.83	.23	-	.86	.30	.004	.008	.42
AF 1410	2.04	10.15	1.04	14.16	.02	.02	.001	.003	.166

The microstructure of each material was evaluated using both optical and electron microscopy. The prior austenite grain size was evaluated using quantitative microscopy after suitable etching.

Carbon extraction replicas were prepared of the as-quenched material for examination using transmission electron microscopy (TEM) and scanning transmission electron microscopy (STEM). Using these techniques the type of submicron particle dispersions as well as their representative size distributions were identified.

Due to uncertainty in the amount of material removed in the replication process accurate volume fractions cannot be determined using extraction replicas. A technique involving a light electropolishing in a 10% perchloric acid in methanol solution was developed to quantify the volume fractions. A 3 mm. diameter disk of material was prepared using traditional methods for TEM specimens. The specimen was then jet polished, but instead of running to perforation, thinning was done for 5 seconds at 17.5 mV., followed by 15 seconds at 10 mV., all at -40°C. These specimens were examined using scanning electron microscopy (SEM) and volume fractions were determined through standard quantitative metallography techniques.

Shear instability behavior was examined in the 4340 steel using linear shear specimens in the quenched and tempered condition. The specimen design is described in ref. [1]. The heat treatment consisted of the 1 hour austenitizing at 870°C, 950°C, 1025°C, 1100°C, or 1200°C followed by oil quenching plus a one hour temper at 200°C. Scribe marks were placed in the gage sections of the specimens to facilitate shear strain measurements after testing. The strain rate was 10^{-3} per second to assure isothermal conditions. The loading was halted after a ≈5% load drop was observed and the shear strains were determined by local angle

measurements of the longitudinal scribe lines using a Leitz universal measuring microscope.

The Charpy impact toughness of the AF1410 steel was evaluated after a heat treatment consisting of a one hour austenitizing treatment at 830°C or 885°C followed by an oil quench plus a five hour temper at 510°C. In addition, the effect of a post-tempering treatment at 400°C for various times was investigated for the AF1410 alloy.

RESULTS AND DISCUSSION

1. RSP and VAR 4340

The microstructure of the 4340 steel was a fine, heavily dislocated tempered lath martensite for both the VAR and RSP material. The RSP steel contained considerable internal porosity due to incomplete consolidation. The RSP material also contained a fair amount of contaminants in the form of large oxide inclusions and superalloy powder particles. The VAR steel suffered considerable grain coarsening as a result of using HTA with the prior austenitic grain size increasing from 17 to 300μm as the austenitizing temperature was raised from 870 to 1200°C. The RSP 4340 showed marked coarsening resistance with the grain size only increasing from 17 to 40μm over the same temperature interval.

The submicron dispersions identified in the as-quenched VAR and RSP 4340 steels after austenitizing at 870°C (CTA) and 1200°C (HTA) are summarized in Table II. It is apparent that the use of high temperature austenitizing (HTA) can drastically reduce the volume fraction of fine dispersions in the VAR 4340 steel. The conventionally austenitized (CTA) material contained a large volume fraction, ≈0.40%, of spheroidal ≈0.2μm $M_{23}C_6$ type alloy carbides. These carbides were completely dissolved after using HTA leaving behind a finer dispersion of highly stable Ti(C,N) particles with a greatly reduced volume fraction of ≈0.04%. In the case of the RSP 4340 the dominant dispersions present are very stable Al_2O_3 and Ti(C,N), and the use of HTA appears to have little effect on the dispersions. The appearance of a large amount of Al_2O_3 is to be expected due to oxidation of the powder surface prior to consolidation. The absence of the alloy carbide indicates that the particles either did not form on solidification or were dissolved during the hot extrusion process. Thus, both solidification and thermal processing can dramatically alter the size, volume fraction, and even the type of submicron dispersions present in 4340 steel in important ways.

The results of the linear shear testing for the Stage I (200°C) temper VAR 4340 steel are illustrated in Figure 1, which plots the instability strain, γ_i, (defined as the uniform background shear strain achieved prior to the shear localization event) as a function of austenitizing temperature. The Stage I temper VAR 4340 displayed instability strains that decreased as the austenitizing temperature was

TABLE II
SUBMICRON PARTICLES IN AS-QUENCHED 4340

Mat'l	Sol'n Temp.	Particle Type	Size Range (nm)	Average Size (nm)	Volume Fraction
VAR	870°C	$(Fe,Cr,Mo)_{23}C_6$	40 - 430	171±67	0.44%
		Ti (C,N)	15 - 100	44±23	
		Al_2O_3	35 - 60	51±9	
		(Ti,Mo)C	5 - 10	5.6±1.3	
	1200°C	Ti (C,N)	30 - 140	78±23	0.05%
		Al_2O_3	40 - 60	53±12	
RSP	870°C	Al_2O_3	15 - 50	28±8	0.27%
		Ti (C,N)	15 - 75	33±11	
	1200°C	Al_2O_3	10 - 55	25±8	0.25%
		Ti (C,N)	15 - 70	35±12	

raised. The reduction in instability strain was moderate up to 1100°C after which a significant reduction occurred. The latter change coincides with the large increment in grain growth previously mentioned. The failure of the HTA (1200°C) VAR occurred in an almost brittle fashion, with the specimen completely fracturing at the first indication of a load drop. The decrease in instability strain with increasing austenitizing temperature is a rather surprising result in light of the proposed microvoid softening mechanism[1,8-10] for inducing shear localization. As illustrated in Table II, the use of HTA yields a substantial reduction in the volume fraction of microvoid nucleating particles in the 4340 material. Hence, the instability strain would be expected to increase. Although there was some metallographic evidence of voiding at the submicron carbide particles, the diminished resistance to shear instability after HTA suggests that microvoid-softening is not the only important mechanism for inducing localization in 4340.

In addition to the differences in the volume fraction of submicron particles in the CTA and HTA VAR 4340 steels (summarized in Table II), there is a substantial amount of coarsening of the prior austenitic grain structure after the HTA treatment. To examine the role of grain size the CTA and HTA VAR steels were given a Stage III (610°C) temper. This introduces a large volume fraction (≈10%) of spheroidized cementite particles into the microstructure of both materials eliminating the disparity in the submicron particle dispersions between the CTA and HTA material. Thus, the only substantial difference between the CTA and HTA conditions after a Stage III temper will be in the prior austenitic grain size. The results of shear testing of the Stage III tempered 4340 are displayed in Figure 2 where the instability strain, γ_i, is plotted as a function of the

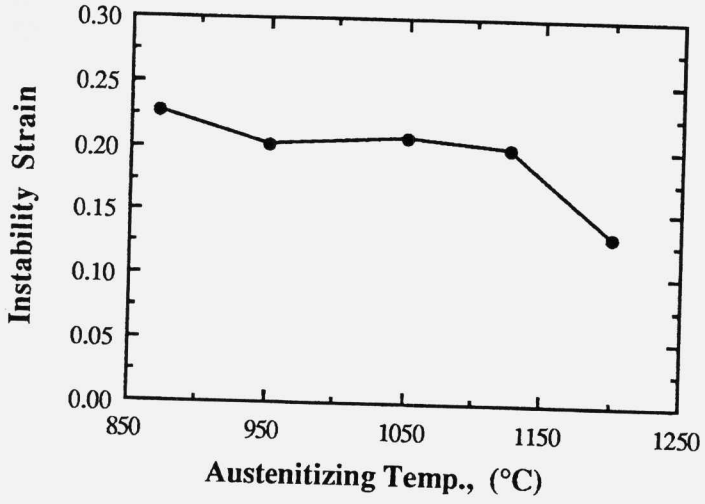

Figure 1 Instability strain as a function of austenitizing temperature on linear shear specimens of VAR 4340.

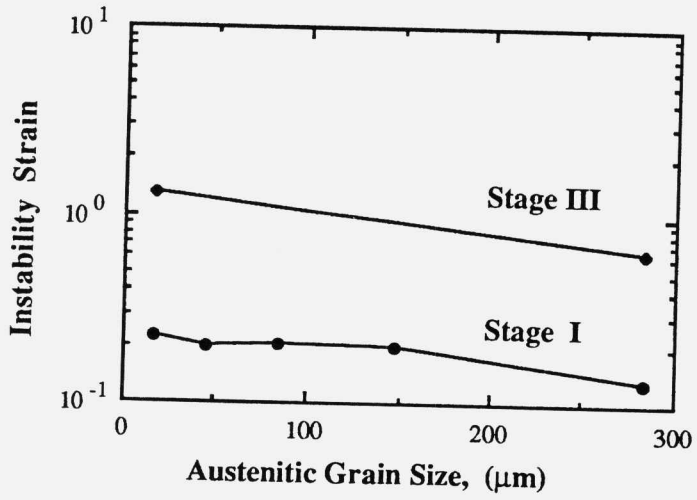

Figure 2 Instability strain as a function of prior austenitic grain size on linear shear specimens of VAR 4340 after different tempering treatments.

prior austenitic grain size for both the Stage I and Stage III tempers. While the instability strain of the Stage III steel is superior to that of the Stage I steel (due to the much lower hardness resulting from the Stage III temper) the instability strain is found to decrease substantially with grain coarsening in both materials. The strain-softening phenomenon driving earlier instability in coarse-grained microstructures may be related to single-crystal plasticity effects[11,12] associated with the limited number of slip systems operating within a single austenite grain. In the fine grain size limit microvoid nucleation is likely the dominant mechanism for localization, but it is clear that substantial grain coarsening severely diminishes the resistance of the material to shear localization (particularly when the grain size becomes comparable to the critical specimen dimension reducing the polycrystalline nature of the test). The observed grain size effect in shear localization again emphasizes the importance of fine grain sizes and hence, grain-refining dispersions, for achieving optimum properties in steels.

2. AF1410

The submicron dispersions identified in the as-quenched AF1410 steel are summarized in Table III after austenitizing at 830°C and 885°C. From the table it is evident that relatively small increases in the solution temperature have a dramatic effect on the fine dispersions in the steel. The CTA material contained several types of alloy carbides with a total volume fraction of nearly 1.0%. The use of HTA, which in this case represents a mere 55°C increase, resulted in the elimination of the majority of these carbides leaving behind only the very stable Ti(C,N) type dispersion. The volume fraction was reduced to well below 0.10%. Autotempering effects resulted in a dispersion of rod-shaped cementite particles for both CTA and HTA AF1410, with the effect being more pronounced in the HTA material. AF1410 is a secondary-hardening steel in which the tempering treatment can completely dissolve the cementite dispersion, eliminating its detrimental effect on toughness.

Unlike the case of the 4340 steel previously described, the alloy carbide dispersions in AF1410 could be removed without suffering severe grain coarsening. The prior austenitic grain size was 27 and 34 μm after austenitizing AF1410 at 830 and 885°C respectively[13]. Hence, a slight increase in the austenitizing temperature for AF1410 eliminates a considerable amount of microvoid nucleating grain-refining particles without suffering the adverse grain coarsening effects.

The Charpy toughness of the quenched and tempered AF1410 steel increased from 57 to 80 ft.-lbs. as the austenitizing temperature was raised from 830 to 885°C. Unfortunately, the hardness decreased slightly from 48 to 47 HRC after raising the austenitizing temperature. While the increase in toughness is clearly beneficial, the diminished hardness, and hence yield strength, will not meet the specifications required for AF1410.

TABLE III

PARTICLES IN AF1410

SOLUTION TEMP.	PARTICLE TYPE	SIZE RANGE
1525°F (830°C)	$(Ti,Mo)_xC,N$	10 - 180 nm
	$(Cr,Fe,Mo)_xC$	50 - 125 nm
	$(Fe,Cr,Mo)_xC$	75 - 105 nm
	$(Mo,Cr)_xC$	30 - 65 nm
	$(Mo,Fe)_xC$	40 - 50 nm
	Mo_xC	5 - 10 nm
1625°F (885°C)	$(Ti,Mo)_xC,N$	20 - 35 nm

There is evidence of short-range ordering (SRO) occurring in the Fe-Ni-Co alloy system[14]. FIM evidence of SRO has also been obtained in AF1410[15]. The effect of a post-tempering treatment at 400°C for various lengths of time was explored in an attempt to exploit SRO reactions to recover the hardness lost as a result of using HTA. Figure 3 plots the hardness and Charpy toughness of the HTA AF1410 steel as a function of post-ageing time at 400°C. In the figure it can be seen that the post-temper ordering treatment can readily recover the hardness lost due to using HTA and by extending the post-tempering time out to 8 hours the hardness can be increased to 49.5 HRC. The hardness is recovered with only a slight loss in the toughness of the steel. Thus, using a combination of HTA and post-age heat treatments can yield superior combinations of hardness and toughness when compared to the conventionally processed steel. This hardness/toughness enhancement is accomplished with only a slight modification of the currently used industrial heat treatment for AF1410.

In the AF1410 steel the toughening effect of removing excess grain refining particles was compromised by the effects of the altered matrix composition resulting from dissolution of the alloy carbides. Thermodynamic modelling of this type of alloy[16] suggests that increased chromium in solution will promote a coarser M_2C strengthening dispersion, reducing the strength and hardness. This constitutes another important consideration when eliminating dispersions through thermal treatment (i.e. dissolution). Fortunately, it appears possible to overcome this "composition altering" effect in AF1410 through exploitation of SRO.

3. Thermally Activated Boundary Unpinning

To enhance the fracture toughness of these ultrahigh-strength steels it is necessary to attain the maximum resistance to microvoid nucleation at the grain refining particles. Recent void nucleation models predict that nucleation resistance

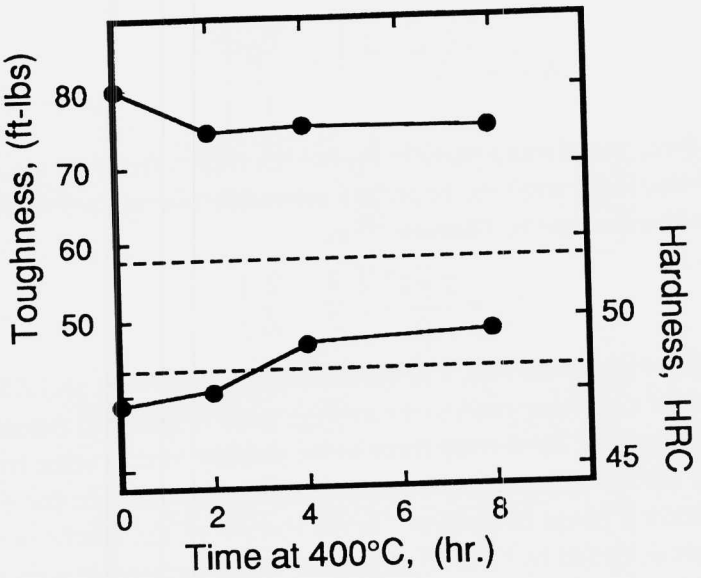

Figure 3 Charpy energy and hardness of high-temperature austenitized AF1410 as a function of post-tempering time at 400°C. Properties of the conventionally heat-treated material are indicated by dashed lines.

is promoted by making the dispersions as fine as possible and by minimizing their volume fraction[3,4]. The pinning force exerted by a particle on a boundary it contacts will decrease with particle size and it is quite feasible that at fine particle sizes the available thermal energy will be sufficiently large so as to assist the grain boundary in unpinning, leading to a larger grain size than predicted by the traditional "Zener-Gladman" type static equilibrium models. The conditions under which thermal activation is important in the boundary migration process were established by applying the traditional concepts of thermal activation[17] to the grain boundary pinning problem. The full details of the model developed can be found elsewhere[18].

From the original analysis of Zener[2] the maximum pinning force $\hat{F}$ exerted on a migrating grain boundary by a particle of radius r is given by:

$$\hat{F} = c \pi r \gamma \qquad (1)$$

where γ is the grain boundary energy and c is a constant reflecting boundary rigidity and multiple particle interactions ($0<c<1$). From this relationship the activation energy ΔG^* needed to free the boundary from the particle as a function of some driving force F_D can be derived, yielding:

$$\Delta G^{*} = \frac{2\,c\,\pi\,\gamma\,r^{2}}{3}\left[\,1 - \frac{F_D}{\hat{F}}\,\right]^{3/2} \qquad (2)$$

The driving force per pinning particle F_D (which results from the elimination of excess grain-boundary area) for boundary migration through a uniform particle distribution was expressed by Gladman[5] as:

$$F_D = \frac{2\,\gamma\,\lambda^{2}}{\bar{D}}\left(\frac{3}{2} - \frac{2}{Z}\right) \qquad (3)$$

where $\bar{D}$ is the average grain size, λ is the mean particle spacing, and Z is the ratio of the diameter of a growing grain to the average grain diameter $\bar{D}$ (usually $Z \approx 1.7$ for steels). By equating the driving force to the pinning force a static equilibrium is established which will predict a limiting average grain size for a material containing a second phase dispersion. In the context of the Gladman model[5], which was later modified by Hsu[19] to provide better agreement with measured particle distributions in tool steels, the average limiting grain size, $\bar{D}_G$, will be given by:

$$\bar{D}_G = \frac{8}{3\,\alpha}\left(\frac{3}{2} - \frac{2}{Z}\right)\frac{r}{f_v} \qquad (4)$$

where α is the boundary/particle interaction distance, which is taken as unity.

The activation energy can now be used in an Arrhenius rate equation[17], with suitable geometrical conversions, to yield an expression for the boundary migration velocity in the presence of thermal activation:

$$v = \frac{d\bar{D}}{dt} = \frac{2\,\lambda}{3\,Z}\,\upsilon\,\exp\left(\frac{-\Delta G^{*}}{kT}\right) \qquad (5)$$

where k is Boltzman's constant, T is the temperature, and υ is the attempt frequency with which the boundary tries to free itself from the pinning particle (here taken to be equivalent to the mechanical attempt frequency for coordinated atomic motion, i.e. $\upsilon \approx 10^{-3}\upsilon_o$, where υ_o is the Debye frequency)[17]. It is apparent in Eq. 5 that the migration velocity can never be zero so that a true static equilibrium is never predicted. This equation can then be integrated to yield the time dependence of the grain size in the regime of significant thermal activation effects.

By choosing an arbitrarily small velocity, so that an effective static equilibrium exists for the time scale of interest, Eq. 5 can be solved to yield the activation energy, and hence the driving force (from Eq. 2), as a function of particle size and temperature. If the effects of thermal activation are minimal the driving force F_D, calculated from Eqs. 2 and 5, will be equal to the maximum driving force $\hat{F}$ of Eq. 1, thus implying that the static equilibrium situation is valid. The ratio of the driving force F_D to the maximum pinning force $\hat{F}$ is plotted

in Figure 4 as a function of temperature for various particle sizes. For large particle sizes, ≤1.0μm, the ratio remains unity indicating a static equilibrium is maintained. However, as the particle size is reduced below 1.0μm the ratio deviates from unity indicating thermal activation has a significant role and thus the grain size will be coarser than predicted by Eq. 4. This effect becomes worse as the temperature is raised.

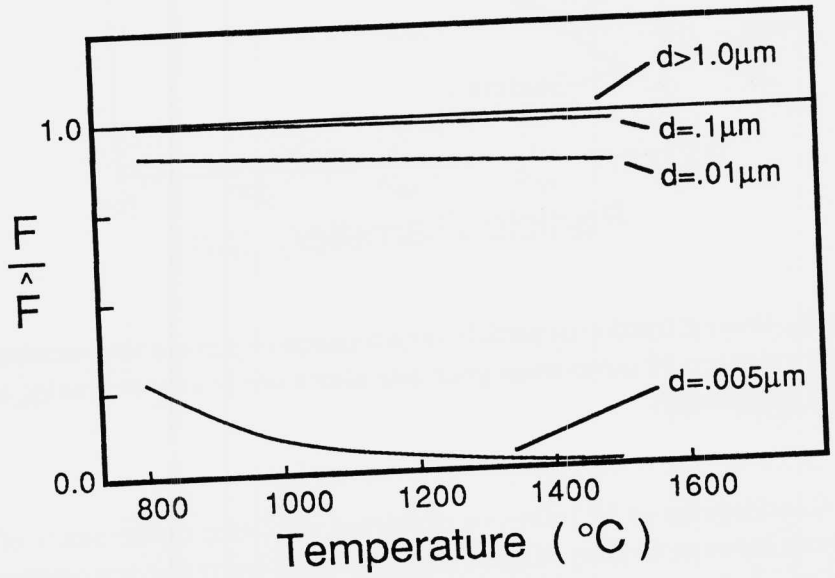

Figure 4 Normalized pinning force as a function of temperature for various particle sizes at the "quasistatic equilibrium" boundary velocity of 10^{-11} cm/sec.

The reduced effective pinning force observed in Figure 4 implies that a larger number, and therefore a higher volume fraction, of particles will be necessary to maintain a given grain size due to the diminished pinning force of each individual particle. Through integration of Eq. 5 the volume fraction of second phase required to maintain a specified grain size can be determined. The particle volume fraction required to maintain a 10 μm grain size in iron after one hour at 870°C and 1200°C is plotted in Figure 5 as a function of particle size. The Gladman relation (Eq. 4) corresponding to a constant r/f_v ratio is plotted for comparison. Figure 5 indicates the Gladman model is quite adequate for large particle sizes, but at fine particle sizes the necessary volume fraction deviates to higher values. This effect becomes stronger as the temperature is raised. Thus, in the thermally activated regime a much larger number of particles is required to prevent coarsening than would be necessary to satisfy the static equilibrium model. A minimum in the required volume fraction occurs at r≈3 nm.

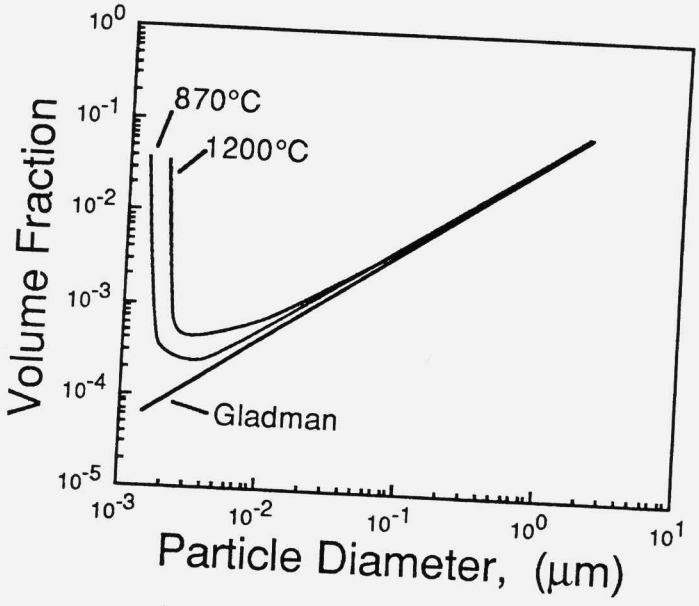

Figure 5 Volume fraction of particles as a function of particle size necessary to maintain a constant 10 μm average grain size after a one hour austenitizing at the indicated temperatures.

Consideration of the influence of thermal activation on the nature of the interactions between an array of static particles and a migrating grain boundary predicts a high degree of thermally activated "unpinning" at very small particle sizes and high temperatures. For a given array of particles, the average grain size will then be coarser than that predicted by the conventional "Zener-Gladman" static equilibrium model, and will be time dependent. Estimating the particle volume fraction, f_v, required to maintain a 10μm grain size in ferrous alloys after a one hour treatment at temperatures of 870-1200°C, it is found that efficient boundary pinning can be achieved by reducing the average particle radius to as low as 10 nm without significant interference from thermal activation effects. Grain refinement with finer and lower volume fraction dispersions may thus offer a viable route to improved microvoid-nucleation resistance and fracture toughness.

4. Microvoid-Nucleation Resistance

The effects of thermal activation on microvoid-nucleation resistance can be ascertained by application of the debonding formalism of Needleman[3,4] to the particle size/volume fraction relationship presented in Figure 5. Experimental data on CTA VAR 4340[20], summarized in Table IV, along with the particle

size/volume fraction relationship depicted in Figure 5, was used as input for the debonding model of Needleman in an effort to examine the microvoid-nucleation strain as a function of particle size in the regime where the grain size is controlled by thermal activation. The calculations maintain a constant 10μm grain size by using the particle size/volume fraction relationship obtained from the thermally activated boundary unpinning model. The results of these calculations are plotted in Figure 6, which illustrates that a decrease of the size of the grain-refining dispersion from the current typical levels of ≈0.2 μm will yield a considerable increase in the void nucleation strain. The results also indicate that the enhanced nucleation resistance, stemming from decreasing the particle size, is not compromised by the increased volume fraction of particles required to prevent the effects of thermal activation for the range of particle sizes of practical interest.

TABLE IV
Physical and mechanical data on VAR 4340 austenitized at 870°C used as input for the Needleman model for particle debonding calculations[20]

Mat'l	Grain Size	Particle Size	Volume Fraction	3-D (*) Spacing	2-D (**) Spacing	Instability Strain
VAR	17μm	0.171μm	0.44%	0.464μm	1.31μm	0.227

$$* \quad \lambda^{3D} = 0.89\, r\, f_v^{-1/3}$$

$$** \quad \lambda^{2D} = 0.5\left(\frac{4\pi r^2}{3 f_v}\right)^{-1/2}$$

4340 Constitutive Equation

Mat'l	σ_o	K	n
VAR	236.0	0.68	0.23

$$\bar{\sigma} = \sigma_o\left(1 + K\bar{\varepsilon}^{n}\right)$$

It is apparent in Figure 6 that if an order of magnitude reduction in particle size from the current levels of ≈0.2 μm could be realized, the critical strain for microvoid nucleation could be increased by over a factor of four even in the presence of significant thermal activation. Recent work by Cowie[1] on ultrahigh-strength steels suggests the critical crack-extension force, G_{Ic}, is directly proportional to the microvoid-nucleation strain. The fracture toughness, K_{Ic}, is related to the square-root of the crack-extension force, G_{Ic}. Hence, a factor of four increase in the debonding strain will roughly translate into a doubling of the

fracture toughness of the material. Thus, substantial increases in K_{Ic} fracture toughness can be realized by reducing the size of the grain-refining dispersion, provided the toughness of the material remains controlled by microvoid induced shear localization.

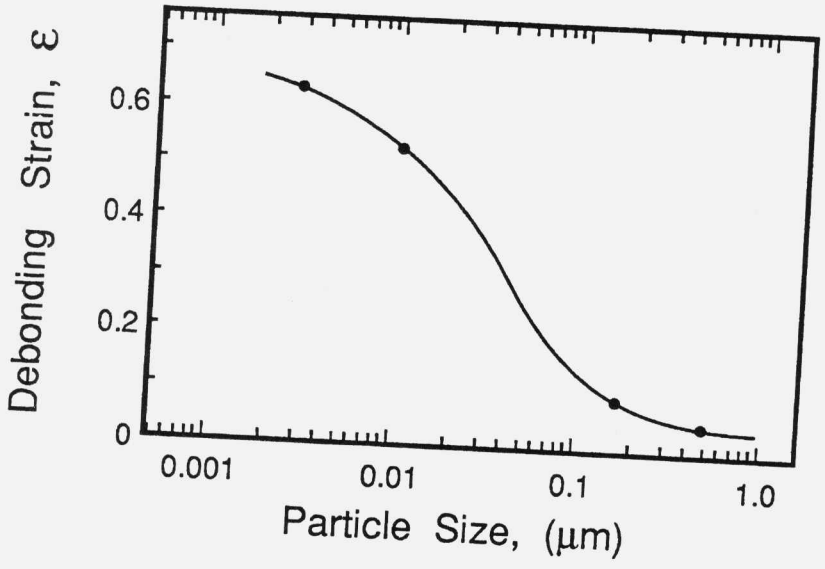

Figure 6 Debonding strain as a function of particle size for alloy carbides in Stage I temper CTA VAR 4340 with a cohesive strength of 2.4 GPa. The material maintains a constant grain size of 10μm using the particle size/volume fraction relationship obtained from the thermally activated unpinning model depicted in Figure 5. Substantial improvement in the debonding strain is predicted if the size of the grain-refining dispersion can be reduced an order of magnitude from the current level of ≈0.2μm..

CONCLUSIONS

Ultrahigh-strength martensitic steels, as exemplified by 4340 and AF1410, contain a variety of very fine (<1μm) particle dispersions. Both solidification and thermal processing can dramatically alter the size, volume fraction, and even the type of dispersions present. Excess alloy carbides of ≈0.2 μm in size were found to be the dominant phases present in the conventionally processed steels. These particles could readily be eliminated by raising the austenitizing temperature, leaving only the most thermodynamically stable compounds.

The role of microvoid nucleation at these fine particles in the mechanical failure of these steels remains somewhat unclear. Some evidence of microvoid nucleation was observed on the submicron dispersions which will have a strong destabilizing effect on the material, particularly with regard to shear instability[21]. However, the apparent dependence of the critical strain for shear localization on the grain size of the steel suggests there are other important mechanisms for inducing failure, especially at the very coarse grain sizes resulting from high-temperature austenitizing. The process of microvoid nucleation alone cannot account for all the observed shear-localization behavior in 4340, but likely represents a dominant mechanism in the fine-grained conventionally austenitized steel.

Elimination of excess grain-refining dispersions, achieved through raising the austenitizing temperature, can lead to substantial improvement in the properties of AF1410. High-temperature austenitizing combined with a suitable post-tempering treatment to promote short-range ordering yields superior combinations of toughness and hardness in AF1410. This represents a significant property gain in the standard alloy composition with only a slight modification of the heat treatment.

The effects of thermally activated grain-boundary unpinning tend to set an absolute limit on the effectiveness of a dispersion to pin grain boundaries at small particle sizes, regardless of the thermodynamic stability of the compound. Thermal activation reduces the effective pinning force of fine particles, and so a larger volume fraction is required to maintain a given grain size. The influence of thermal activation starts becoming significant at particle sizes smaller than ≈0.1 μm. Particles smaller than ≈2 nm offer negligible resistance to boundary migration.

The particle size at which the effects of thermal activation become significant is predicted to be of the order of r≤10 nm. Resistance to microvoid nucleation is enhanced not only by reducing the size of the particles but also by reducing their volume fraction due to the reduced interaction between particles. Preliminary evidence indicates that the volume fraction effect may be stronger than the size effect in enhancing void-nucleation resistance[4]. Hence, substantial reduction of r and f_v (at a constant r/f_v) from the currently typical levels of r=200 nm and $f_v \approx 10^{-3}$ for grain-refining dispersions can potentially offer large improvements in microvoid nucleation resistance.

Interfacial debonding calculations predict that substantial improvement in resistance to microvoid nucleation can be realized by reducing the size of the grain-refining dispersion below the current levels of ≈0.2 μm, even in the presence of significant thermal activation. This change will yield a significant increase in the toughness of the material provided the dominant mechanism remains void-nucleation-controlled shear localization. The size scale at which thermal activation effects would severely compromise these potential improvements (by requiring higher f_v to maintain a given $\bar{D}$) is likely well below

that achievable with high-stability grain-refining dispersions and current processing methods in ferrous alloys.

The focus of this investigation has been on the fine-scale secondary dispersions, which in high-cleanliness steels of optimal microstructure will serve as a grain-refining dispersion as well as potential sites for microvoid nucleation. These particles have taken on importance due to the near elimination of the primary inclusions now possible with improved processing techniques. In reality, some finite volume fraction of primary inclusions will still be present. Whereas, it is important to minimize the size of the secondary grain-refining dispersions for optimum toughness, investigation into the role of the primary inclusions on fracture toughness suggests that for a given volume fraction they should be as coarse as possible to maximize the interparticle spacing[22,23]. Hence, a material designed for optimum toughness will contain a dichotomy of particle sizes; a grain-refining dispersion whose size is to be minimized, and a residual primary inclusion content whose size is to be maximized.

Clearly, in the development of improved ultrahigh-strength structural materials, a critical element of the microstructure is the grain-refining dispersion. It is well established that fine grain sizes generally impart better toughness and ductility to a material. In addition to the well known benefits of grain refinement, results of this investigation indicate that resistance to shear localization can be enhanced by maintaining a fine prior austenitic grain size. These vital grain-refining dispersions likewise serve as sites for microvoid nucleation, subsequently limiting the useful ductility of the material. Hence, it is necessary to explore potential improvements in both grain-refining ability and microvoid-nucleation resistance to effectively optimize the second-phase particles in an alloy.

ACKNOWLEDGEMENTS

The authors are grateful to Prof. Alan Needleman of Brown University for his help in running the microvoid nucleation calculations of Fig. 6. The research reported here was sponsored by the Office of Naval Research and the National Science Foundation.

REFERENCES

1. J. Cowie, M. Azrin, G.B. Olson, elsewhere in this proceedings
2. C. Zener, quoted by C. S. Smith, Trans. A.I.M.E., 175, 15 (1948)
3. A. Needleman, J. Appl. Mech., in press
4. A. Needleman, elsewhere in this proceedings
5. T. Gladman, Proc. Roy. Soc. London, 294A, 298 (1966)
6. M. Hillert, Acta Met., 13, 227 (1965)
7. M. F. Ashby, *First Int. RISØ Symp. on Met. and Mat. Sci.*, 325 (1980)
8. M. Saje, J. Pan, A. Neeedleman, Int. J. of Frac., 19, 163 (1982)

9. J. Pan, M. Saje, A. Neeedleman, Int. J. of Frac., 21, 261 (1983)
10. C.A. Berg, *Inelastic Behavior of Solids*, ed. M.F. Kanninen, McGraw-Hill, New York, 171 (1970)
11. J.W. Rudnicki, J.R. Rice, J. Mech. Phys. Solids, 23, 371 (1975)
12. R.J. Asaro, J.R. Rice, J. Mech. Phys. Solids, 25, 309 (1977)
13. M.L. Schmidt, M.J. Gore, elsewhere in this proceedings
14. A.F. Yedneral, O.P. Zhukov, M.A. Kablukovskaya, B.M. Mogutnov, M.D. Perkas, Fiz. Metal. Metalloved, 36, 727 (1974)
15. L. Chang, G.D.W. Smith, G.B. Olson, J. de Physique, in press
16. M. Grujicic, elsewhere in this proceedings
17. U. F. Kocks, A. S. Argon, M. F. Ashby, Prog. in Mater. Sci., 19, 1 (1974)
18. M.J. Gore, M. Grujicic, G.B. Olson, Acta Met., in press
19. C.Y. Hsu, Doctoral Thesis, Massachusetts Institute of Technology, (1983)
20. M.J. Gore, Doctoral Thesis, Massachusetts Institute of Technology, (1988)
21. J.W. Hutchinson, V. Tvergaard, research at Harvard University, in press, (1987)
22. W.M. Garrison, Met. Trans., 17A, 669 (1986)
23. W.M. Garrison, N. Moody, Met. Trans., 18A, 1257 (1987)

FRACTURE TOUGHNESS:

PARTICLE-DISPERSION CORRELATIONS

W. M. GARRISON, JR., AND K. J. HANDERHAN
Department of Metallurgical Engineering and Materials Science
Carnegie Mellon University
Pittsburgh, PA 15213

INTRODUCTION

The purpose of this paper is to discuss ongoing research at Carnegie Mellon University on the fracture behavior of ultra high strength steels and how this work may be of relevance to the design of ultra high strength steels of improved upper shelf toughness.

The measure of toughness considered here is the fracture initiation toughness. Throughout, this will be quantified by the critical crack tip opening displacement (δ_{IC}). δ_{IC} can be related to the usual measure of fracture initiation toughness (K_{IC}) through the equations

$$\delta_{IC} = d_n \, J_{IC}/\sigma_0 \qquad J_{IC} = K_{IC}(1 - \nu^2)/E \qquad [1]$$

where J_{IC} is the value of the J integral at fracture, σ_0 is the flow stress, and d_n is a function of the work hardening exponent n and the ratio of the yield strength to the modulus (1,2). In all cases, unless noted, the δ_{IC} reported will be that calculated from measured values of K_{IC} or J_{IC}. While δ_{IC} is perhaps a less precisely defined quantity than J_{IC} or K_{IC}, it has been used because it emphasizes the scale of the fracture process and the importance of the blunting behavior in determining fracture toughness.

Our interest then is to quantify the extent to which and under what conditions various microstructural features influence the fracture initiation toughness when fracture is by microvoid coalescence. To do this we have found it convenient to separate

the microstructure into three categories: primary particles, secondary particles inherited from the austenitizing temperature and the fine scale microstructure.

The primary particles are the inclusions. A variety of inclusions can be found in steels, depending on the composition and the melt practice (3). In the steels we have considered the inclusions are primarily either manganese sulfides, chromium sulfides or rare earth compounds. It is commonly believed, and will be assumed here, that these particles are weakly bonded to the matrix and can be regarded as pre-existing voids in the material (4).

In addition to the inclusions or primary particles steels can contain other particles. We will term these the secondary particles. There are two sources of secondary particles: the secondary particles inherited from the austenitizing treatment and the secondary particles precipitated during the quench from the austenitizing temperature (auto-tempered carbides) or during tempering. In the materials we have examined the secondary particles are much smaller than the inclusions and are believed to be strongly bonded to the matrix. Thus we expect void nucleation at the secondary particles will occur much later in the fracture process than the nucleation of voids at the inclusions.

The secondary particles inherited from the austenitizing temperature can include undissolved carbides, undissolved nitrides and complex carbo-nitrides. They are typically present in such small volume fractions that they do not contribute to the strength of the steel. Their only function appears to be to help minimize grain growth during austentitzing. The secondary particles inherited from the austenitizing temperature play no role in the fracture process unless conditions are such that they nucleate voids.

At this point we regard all microstructural features other than inclusions and secondary particles inherited from the austenitizing temperature as constituting the fine scale microstructure. The fine scale microstructure can influence the fracture process both directly and indirectly. The fine scale microstructure can directly influence the fracture process if some of the particles formed during the quench or on tempering actually nucleate voids. However, the

secondary particles precipitated on tempering can influence the fracture process even if they do not nucleate voids. They can indirectly influence the fracture process by helping to determine the flow characteristics of the material and the nature of the blunting process. Other microstructural features may indirectly influence the fracture process. These include the prior austenite grain size, the packet and lath size, the amount, morphology and mechanical stability of the retained austenite, and the dislocation structure in the material.

Our first goal is to quantify how the inclusions, secondary particles inherited from the austenitizing temperature and the fine scale microstructure influence the fracture initiation toughness. The first section of this paper will discuss the effects of inclusions on fracture initiation toughness. The second section will present our limited results on the effects of second phase particles formed during austenitizing. A third section will discuss indirect effects of the fine scale microstructure on the fracture initiation toughness.

Our second goal is to determine how one might most conveniently relate δ_{IC} to the various parameters used to quantify the microstructure. The fifth section will discuss various approaches to this problem. We conclude with a brief summary of our results to date.

INCLUSION SPACING

In assessing the influence of inclusions on fracture initiation toughness it will be assumed that the inclusions are characterized by a unimodal size distribution and can be considered as pre-existing voids. The materials discussed here are believed to satisfy these requirements. Within this constraint it appears the most important variable is the inclusion spacing. We have some results which suggest the sharpness of the size distribution can also be of importance but it appears to be normally of secondary importance to the inclusion spacing. We emphasize however that if there is a bimodal size distribution of primary particles then the average particle spacing does not appear to be a useful parameter.

The theoretical treatment of Rice and Johnson (5) suggests the importance of inclusion spacing. Rice and Johnson considered a pre-existing void of radius R_0 a distance X_0 from the initially sharp crack tip. They calculated the void size as a function of δ using the Rice and Tracey (6) equations for void growth and ignoring possible interactions with the crack tip and the growing void. Assuming fracture to occur when the ligament between the growing void and the blunting crack tip was the same as the vertical void radius, they obtained a relationship between δ_{IC}/X_0 and the ratio X_0/R_0 as shown in Fig. 1. This allows δ_{IC} to be written as

$$\delta_{IC} = X_0 F(X_0/R_0) \qquad [2]$$

where $F(X_0/R_0)$ varies slowly with X_0/R_0. They suggested that in applying their model, that X_0 could be regarded as the average three-dimensional spacing defined by $X_0 = .89\ R_0 f^{-1/3}$ where R_0 is the average particle radius and f is the particle volume fraction. This treatment then implies that δ_{IC} and K_{IC} will scale as the inclusion spacing according to the equations

$$\delta_{IC} = X_0 F(.89 f^{-1/3}) \qquad [3]$$

$$K_{IC} = \left\{ \frac{X_0 E \sigma_0 F(.89 f^{-1/3})}{d_n (1-\nu^2)} \right\}^{1/2} \qquad [4]$$

The Rice and Johnson model predicts that δ_{IC} should scale with X_0, the primary spacing. The model, however, does not provide particularly good quantitative agreement with experiment, as shown in Fig. 2. In addition it predicts that K_{IC} will increase with the material's strength, which is in contradiction to most experimental studies. These observations suggest that the model is incomplete, which should not be too surprising as it does not incorporate possible effects of secondary particles and the fine scale microstructure. However, the work of Hahn and Rosenfield (8,9) and of Birkle et al. (10) suggests that as long as the microstructure remains otherwise constant, δ_{IC} will scale with X_0.

However, other experimental studies have been interpreted to suggest that δ_{IC} will not scale with X_0 even for an otherwise constant microstructure. The Rice and Johnson model predicts that, as $X_0 = .89\ R_0 f^{-1/3}$, then, at a fixed inclusion volume fraction, the toughness should increase with the primary particle size, R_0. Cox

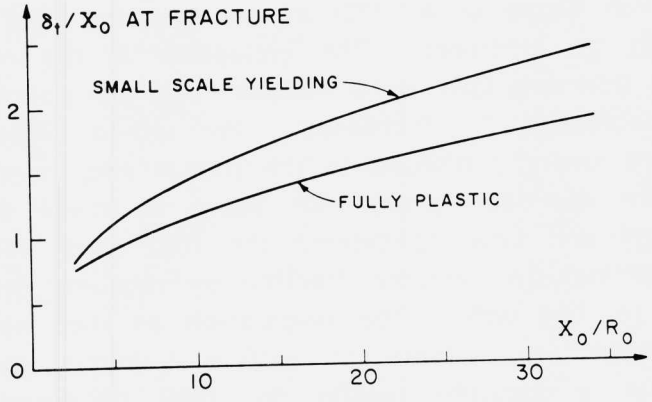

FIGURE 1. The numerical results obtained by Rice and Johnson (5) for δ_{IC}/X_0 as a function of X_0/R_0.

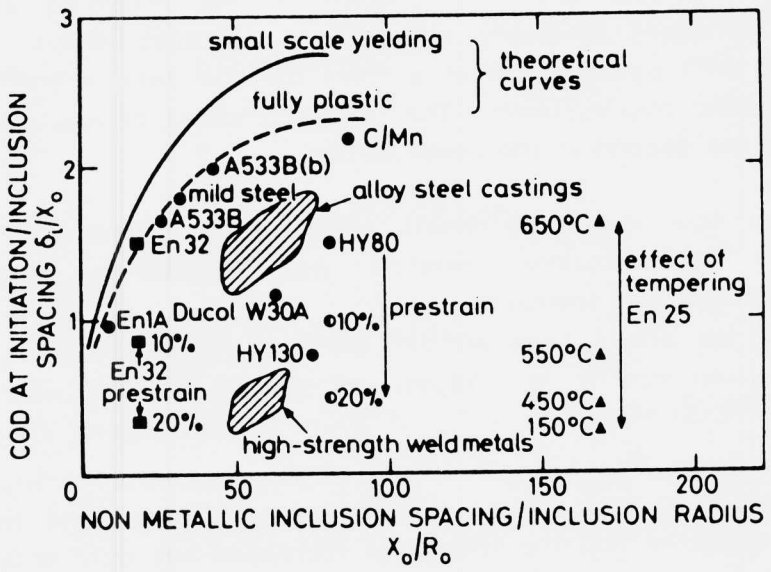

FIGURE 2. Experimental data for δ_{IC}/X_0 plotted as a function of X_0/R_0 (from ref. 7).

and Low (11) found for both a maraging steel and a low alloy steel that at a fixed X_0, δ_{IC} increased as the particle size decreased; therefore Van Stone et al. (12) argued that the Rice and Johnson model must be incorrect. The inclusions in the maraging steel studied by Cox and Low were Ti(C,N). As the size of the Ti(C,N) particles decreased, δ_{IC} increased. We would argue that Ti(C,N) particles are strongly bonded to the matrix and, therefore, the Rice and Johnson approach would not apply to these materials. In addition, Cox and Low considered the low alloy steel 4340 and changed the inclusion volume fraction by reducing the sulfur level from .013 to .004 wt%. The orientation of their test specimens would enhance any effects of sulfide stringers and we would suggest that a possible reason for their observed increase in toughness with reduced sulfur content was the reduction in the influence of stringers.

Here we will present evidence that in the absence of nucleation strains (probably present in the maraging steel) and sulfide stringers (probably present in the 4340 steel), δ_{IC} does increase with particle size at a fixed particle volume fraction. We will consider two systems. The first is a series of low alloy steels (13) and the second is the steel AF1410.

The four low alloy steels whose compositions are given in Table 1 are virtually identical with respect to fine scale microstructure and inclusion volume fraction. As shown in Table 2, three of the steels have almost identical toughnesses ($\delta_{IC} \approx 10\mu m$) and inclusion size ($R_0 \approx 0.30\mu m$) and spacing ($X_0 \approx 3.5\mu m$). However, the base+Ni+Si steel has a δ_{IC} of $20\mu m$ and inclusions almost three times as large ($R_0 \approx 0.71\mu m$) and as widely spaced ($X_0 \approx 10\mu m$). The inclusions in all four steels are manganese sulfides. The importance of this result is that the toughness increases not only with spacing but does so at a constant volume fraction; that is, by increasing the average size.

The second system is the steel AF1410. Two heats of the steel are considered and their compositions are given in Table 3. The inclusions in the first heat are rare earth oxysulfides and; in the second heat they are CrS. As shown in Table 4, the two heats contain almost identical inclusion volume fractions but $R_0 = 0.17\mu m$

TABLE 1

COMPOSITIONS OF EXPERIMENTAL LOW ALLOY STEELS

Alloy	Compositions*							
	C	Ni	Cr	Mn	Si	S	P	O
base	0.39	1.47	1.01	0.49	0.01	0.005	0.008	0.0045
base + Si	0.36	1.48	0.95	0.48	1.91	0.005	0.007	0.0035
base + NI	0.35	2.93	0.98	0.49	0.01	0.008	0.007	0.0022
base + Ni + Si	0.34	2.89	1.02	0.49	1.88	0.005	0.006	0.0028

*compositions in wt pct

TABLE 2

MECHANICAL PROPERTIES AND INCLUSION DATA FOR EXPERIMENTAL LOW ALLOY STEELS

	σ_y (MN/m^2)	σ_o (MN/m^2)	K_{IC} (MN/m$^{3/2}$)	δ_{IC} (μm)	f	R_o (μm)	X_o (μm)
base	1655	1802	75	8.5	0.00036	0.26	3.3
base+Si	1772	1903	70	7.1	0.00024	0.26	3.7
base+Ni	1565	1688	79	10.1	0.00039	0.28	3.4
base+Ni+Si	1682	1810	115	20	0.00027	0.71	9.8

and X_0 = 2.34μm in the heat containing CrS inclusions and R_0 = 0.64μm and X_0 = 7.62μm in the heat containing the rare earth oxysulfides. The properties of two heats compared after aging at 425°C and 510°C are shown in Table 4. As shown in Table 4, δ_{IC} increases with R_0 and X_0 for both aging temperatures. The effect is critical. After aging at 510°C, δ_{IC} at the spacing of 2.34μm is 28μm and is 66μm at a spacing of 7.62μm. The secondary particles inherited from the austenitizing temperature in the two heats were very similar with respect to type, average size, and the number per unit area as measured from extraction replicas of polished cross sections.

TABLE 3

COMPOSITIONS OF TWO HEATS OF AF1410

	Compositions*													
Alloy	C	Co	Ni	Cr	Mo	V	Mn	P	S	Si	Al	O	N	La
heat 1 (R.E.)	0.16	14	10.1	2.1	1.0	.001	.03	.004	.001	.03	.003	.0009	.0003	.008
heat 2	0.16	14	9.97	2.04	1.0	.001	.001	.004	.001	.01	.003	.001	.0009	<.002

*Compositions in wt%; O and N are total

TABLE 4

COMPARISON OF INCLUSIONS AND MECHANICAL PROPERTIES OF THE TWO HEATS OF AF1410

	Yield Strength (MN/m^2)	δ_{IC} (μm)	f	R_0 (μm)	X_0 (μm)	$\bar{\epsilon}_f$	n
HEAT1							
425°C	1458	23	.00042	0.64	7.62	0.14	0.12
510°C	1533	66	.00042	0.64	7.62	0.23	0.09
HEAT2							
425°C	1414	12	.00034	0.18	2.34	0.16	0.11
510°C	1527	28	.00034	0.18	2.34	0.21	0.08

In conclusion, we find that the prediction of the Rice and Johnson model appears to be correct; that is, for a fixed fine scale microstructure and identical dispersions of secondary particles inherited from the austenitizing temperature, δ_{IC} will, over some range of X_0, scale as X_0. We note here, and will return to this point, that δ_{IC} cannot continue to scale indefinitely with X_0. At some point δ_{IC} will become independent of the inclusion spacing. In terms of controlling X_0, it appears that rare earth additions can be used to achieve spacings of the order of 8-10 μm in any steel. Thus, it is possible, through the use of such additions, to achieve fracture toughnesses on the order in 115 $MN/m^{3/2}$ for low alloy steels such as 4340 and 300M tempered to high strength levels.

SECONDARY PARTICLES

The conventional picture we have of how the secondary particles might enter the fracture process is drawn from the observations of Cox and Low (11). As shown in Fig. 3, the voids nucleated at the primary particles grow until they coalesce *via* the formation of a void sheet where the voids in the void sheet are nucleated at the secondary particles. Certainly, we expect the effects of such particles to be detrimental to the toughness and we will present some results to illustrate their effects. However, as we will discuss, it is extremely difficult to quantify the effects of such particles on fracture initiation toughness, even at a fixed primary particle spacing; and it may be that the secondary particles will become increasingly important in the fracture process as the primary particle spacing increases.

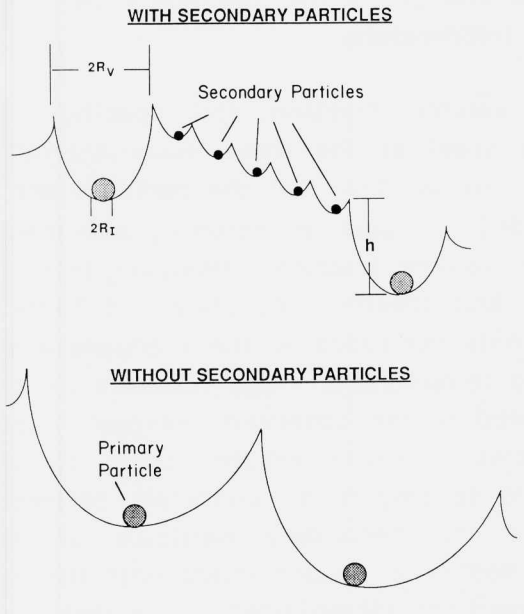

FIGURE 3. A schematic illustrating how void sheet formation leads to the coalescence of voids initiated at the primary particles.

First we will consider the effect of austenitizing temperature on the toughness of a heat of HP9-4-20 steel in the as-quenched condition. This heat is designated HP9-4-20#1 and its chemistry is given in Table 5. The mechanical properties and microstructural data concerning the as-quenched condition of this heat of HP9-4-20 steel are summarized in Table 6 for austenitizing temperatures of 840°C, 1050°C and 1200°C. As shown in Table 6, δ_{IC} increases with austenitizing temperature and is 10μm, 23μm, and 44μm at 840, 1050, and 1200°C, respectively. The improvement in toughness with increasing austenitizing is due in part to the increase in the spacing of the primary particles (MnS). The spacing of the MnS inclusions is 3.7μm, 5.4μm, and 7.4μm after austenitizing at 840, 1050, and 1200°C, respectively. However, normalizing δ_{IC} with respect to X_0, as shown in Table 6, we see that the toughness increase cannot be attributed to the increase in X_0 alone. At this point we feel that the other factor which leads to the increase in δ_{IC} with austenitizing temperature is a change in the secondary particles inherited from the austenitizing temperature.

The size, volume fraction, and spacing of the secondary particles in this steel at the three austenitizing temperatures are given in Table 7. It is clear that the particles are extremely stable and do not readily go back in solution, and; there is no apparent decrease in their volume fraction. However, there is an increase in the average size and spacing. As shown in Table 6, the extent of growth of the voids nucleated at the manganese sulfides increases with austenitizing temperature. This increase in the extent of void growth is attributed to the observed changes in the spacing of the secondary particles. These results seem to suggest that the secondary particle spacing is an important parameter in discussing the influence of the secondary particles on fracture initiation toughness. This seems to be consistent with the work of Curry and Pratt (14) who found for spheroidized steels that δ_{IC} scaled as

$$\delta_{IC} \approx X_0(k_1 D^{1/2} + k_2)$$

where X_0 was the inclusion spacing, D was the spacing of the spheroidized carbides, and k_1 and k_2 were material constants.

However, it is clear that the particle spacing is not sufficient to quantify the effects of secondary particles. Consider the second

TABLE 5

CHEMISTRIES OF HP9-4-X STEELS

	Compositions*												
Alloy	C	Co	Ni	Cr	Mo	V	Mn	P	S	Si	Al	Ti	O	N
HP9-4-20#1	0.20	4.6	9.2	7.6	1.09	.10	.47	.006	.004	.06	.03	.007	.001	.004
HP9-4-20#2	0.21	4.3	8.6	.77	.94	.09	.26	.005	.002	.04	.009	.004	.0013	.002
HP9-4-10	0.10	3.9	8.9	.76	1.02	.10	.31	.004	.002	.01	.001	nil	.001	.0002

*Compositions in wt%.

TABLE 6

MECHANICAL PROPERTIES AND INCLUSION DATA OF HP9-4-20(#1) AS A FUNCTION OF AUSTENITIZING TEMPERATURE

γ Temp.	σ_0 (MN/m^2)	δ_{IC} (μm)	f	R_0 (μm)	X_0 (μm)	(R_V/R_I)	δ_{IC}/X_0
840°C	1469	10	.00022	.25	3.7	6.8	2.7
1050°C	1409	24	.00016	.30	5.4	7.9	4.44
1200°C	1380	44	.00015	.43	7.4	9.6	5.95

TABLE 7

SECONDARY PARTICLES AS A FUNCTION OF AUSTENITIZING TEMPERATURE FOR THE STEEL HP9-4-20(#1)

γ Temp.	f	R_0 (μm)	X_0 (μm)
840°C	.00014	.043	.37
1050°C	.00013	.052	.45
1200°C	.00016	.06	.50

TABLE 8

COMPARISON OF MECHANICAL PROPERTIES AND INCLUSION DATA FOR THE TWO HEATS OF HP9-4-20 STEEL AUSTENITIZED AT 840°C

Steel	σ_0 (NM/m^2)	δ_{IC} (μm)	f	R_0 (μm)	X_0 (μm)	R_V/R_I	$\bar{\epsilon}_f$	n	δ_{IC}/X_0
HP9-4-20#1	1469	10	.00022	.25	3.7	6.8	.15	.14	2.7
HP9-4-20#2	1398	15	.00022	.17	2.5	10.3	.25	.18	6.0

heat of HP9-4-20 steel whose composition is also given in Table 5. The mechanical properties of the two heats of HP9-4-20 steel in the as-quenched condition after austenitizing at 840°C are compared in Table 8.

The δ_{IC} of the second heat is 15μm, compared to the δ_{IC} of 10μm for the first heat. This is despite the fact that the second heat has a much smaller primary particle spacing. The difference seems to be the nature of the secondary particles. The secondary particles in the first heat were complex carbon-nitrides of an average radius of .041μm and average spacing of .37μm. The secondary particles in the second heat were vanadium carbides of an average radius of .014μm and an average spacing of about 0.1μm; this is a much smaller spacing than observed for the complex carbo-nitrides in the first heat. The obvious explanation is that it is much more difficult to nucleate voids at the smaller vanadium carbides than at the complex carbo-nitrides.

This is the crux of the problem. In order to account quantitatively for the effects of the secondary particles, the spacing may be important but we also need to incorporate the factors controlling void nucleation at these particles. The secondary particles will nucleate voids when the interfacial stress reaches some critical value(15,16). It is possible that this critical interfacial stress for void nucleation could vary with changes in particle composition, composition of the matrix, segregation of impurities to

the matrix-particle interface, and possibly on the particle size. In the absence of quantitative information about the void nucleation process, it is necessary to incorporate the effects of the secondary particles in a very indirect fashion either through, as has been suggested, the extent of void growth or, as we will discuss later, the plane strain tensile ductility.

FINE SCALE MICROSTRUCTURE

The fine scale microstructure can influence the fracture initiation toughness directly if particles precipitated on tempering nucleate voids. However, the particles precipitated on tempering can influence the fracture process, even if they do not nucleate voids. This is because the fine scale microstructure can influence the flow characteristics and blunting process.

For example, the data in Table 4 for the steel AF1410 clearly shows the importance of fine scale microstructure in determining the fracture initiation toughness. It can be argued (17,18) that the microstructure achieved on tempering the steel AF1410 at 510°C is tougher than the structure obtained after tempering at 425°C because it is more difficult to nucleate voids at the particles formed at 510°C than at the particles formed on tempering at 425°C.

On tempering this steel at 510°C it is believed that the intra-lath carbides are entirely M_2C. These particles are extremely fine needles (100 Å in length) and probably are semi-coherent to the matrix. Thus, it should be very difficult to nucleate voids at these particles. On the other hand, the intra-lath carbides in AF1410 tempered at 425°C are cementite needles about 1000 Å long. It is believed that these particles are more favorably disposed to nucleate voids. However, this explanation may not adequately explain the higher toughness of the 510°C microstructure. It is possible that differences in the flow characteristics of the steel after tempering at 425°C and 510°C contribute indirectly to the change in toughness. The purpose of this section is to demonstrate the effects of flow behavior on the blunting process and the possibly strong influence of this process on fracture initiation toughness.

TABLE 9

MECHANICAL PROPERTIES OF HP9-4-20 (#2) AND HP9-4-10 IN THE AS-QUENCHED CONDITION AND AFTER TEMPERING AT 565°C (1 HR)

Material	σ_0 (MN/m^2)	δ_{IC} (μm)	f	R_0 (μm)	X_0 (μm)	$\bar{\epsilon}_f$	n
HP9-4-20(#2)							
A.Q.	1398	16	.00022	0.17	2.50	.25	.18
565°C	1313	91	.00022	0.17	2.50	.37	.05
HP9-4-10							
A.Q.	1107	44	.00036	0.19	2.40	.53	.17
565°C	1117	161	.00036	0.19	2.40	.62	.05

We have examined in detail the blunting behavior of the steels HP9-4-20 (#2) and HP9-4-10 in the as-quenched condition and after tempering at 565°C. The properties of the four microstructures are compared in Table 9. Rather surprisingly the microstructures with the highest fracture initiation toughness are those obtained after tempering at 565°C and which have the lowest value of the work hardening exponent, n. This seems to be due to the differences in blunting behavior shown in Fig. 4. Both the as-quenched materials blunt smoothly and voids are formed directly ahead of the blunting crack tip. The voids ahead of the blunting crack tip appear to be single particle nucleated voids for the HP9-4-20 steel; but the voids ahead of the blunting crack tip for the as-quenched HP9-4-10 steel are quite large and appear to be super voids resulting from the coalescence of many particle nucleated voids. However, for both materials the blunting is relatively smooth. But, as shown in Fig. 4, both steels, when aged at 565°C, blunt to vertices and the void sizes when normalized by the applied J are much less than observed for the as-quenched microstructure. It is possible that the blunting to vertices observed for the materials of lower work hardening exponent results in significantly higher fracture initiation toughnesses.

McMeeking (19) suggested the possibility of blunting to

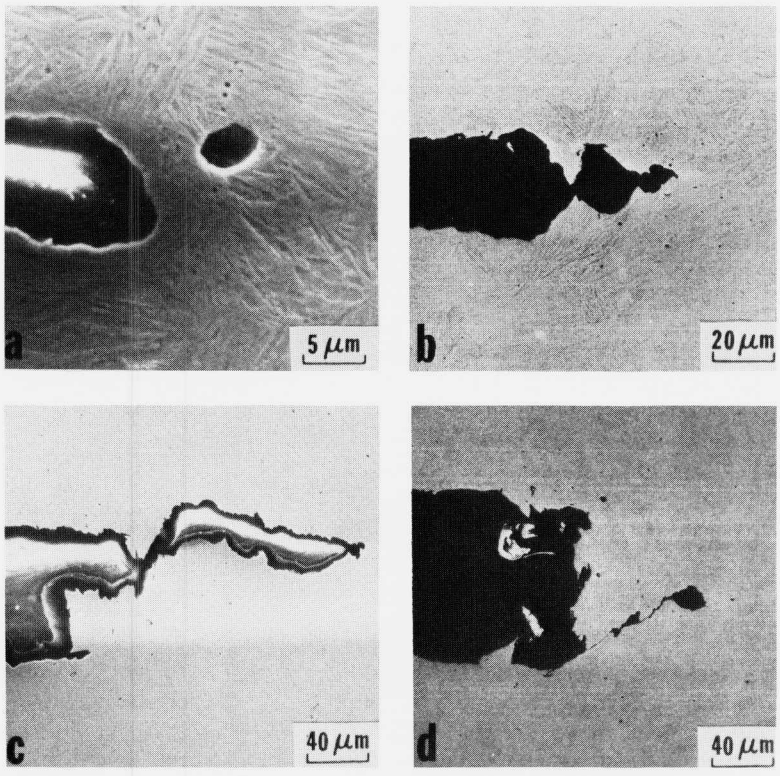

FIGURE 4. Cross sections of blunted cracks at J values close to the value J_{IC} for (a) HP9-4-20 (#2) in the as-quenched condition, (b) HP9-4-10 in the as-quenched condition, (c) HP9-4-20 (#2) tempered at 565°C, and (d) HP9-4-10 tempered at 565°C.

vertices and showed that such blunting would lead to stabilized void growth directly ahead of the crack tip. Further, such blunting would, at least directly ahead of the crack tip, result in both lower strains and less severe stress states. The rates of void growth and strains for the various blunting behaviors are shown in Fig. 5. The stress states are compared for the cases of smooth blunting and blunting to a square crack in Fig. 6. The stress states for the smooth blunting crack at n = .17 are much more severe than for the squarely blunting crack at n = .05.

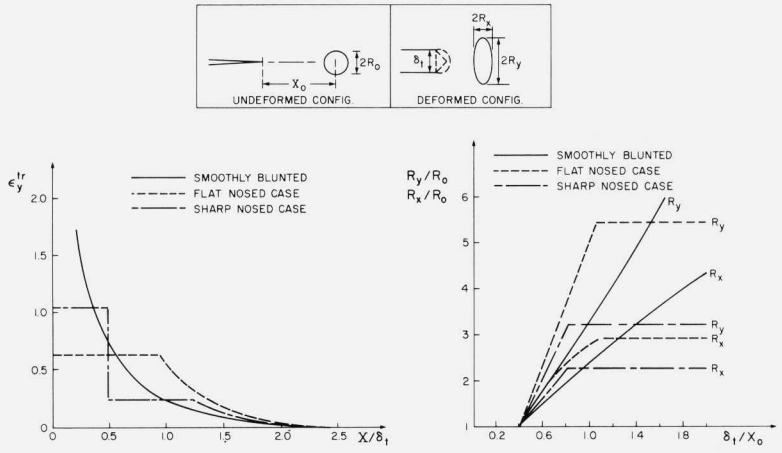

FIGURE 5. The strains and normalized rates of void growth for a crack blunting smoothly, blunting to a square, and blunting to a triangular shape (from ref. 19).

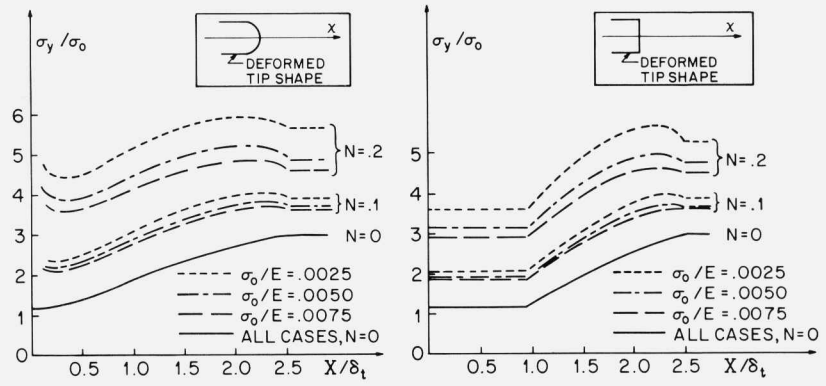

FIGURE 6. A comparison of the ratio of the stress in the y direction normalized by the yield strength ahead of a) a smoothly blunting crack and b) a crack blunting to a square or flat nose (from ref. 19).

The reduced strains and less severe stress states associated with blunting to vertices will reduce the rates of void growth and make it more difficult to reach the critical interfacial stress required to nucleate voids at the various secondary particles. We have not yet performed sectioning experiments in the steel AF1410 tempered at 425°C and 510°C. However, because of the low value of n for the 510°C structure, we anticipate there are differences in blunting behavior which contribute the differences in fracture initiation toughness.

EXPRESSIONS FOR δ_{IC}

Ideally we would like to develop expressions for δ_{IC} solely in terms of microstructural parameters. Such an expression would include the primary particle spacing, parameters necessary to include effects of the secondary particles and reflect the influence of the fine scale microstructure on the blunting characteristics. Clearly this is not possible. However, we might hope to develop such expressions utilizing X_0, the primary particle spacing, and other parameters we believe are adequate to indirectly express the effects of secondary particles and the effects of the fine scale microstructure on the blunting behavior.

Our expectation is that for a fixed dispersion of secondary particles and a fixed fine scale microstructure δ_{IC} will, at least for some range of X_0, be linear with respect to X_0. This is nicely shown in Fig. 7, which incorporates the data of Birkle *et al.* (10) as plotted by Hahn and Rosenfield (8). This shows that for a fixed fine scale microstructure δ_{IC} scales with X_0 and the slope of δ_{IC} *vs* X_0 is determined by the fine scale microstructure. Thus we expect, over some range of X_0, that $\delta_{IC} \approx X_0 f$ where f is determined by the nature of the secondary particles inherited from the austenitizing temperature and the fine scale microstructure.

However in the limit as $X_0 \rightarrow \infty$ it is clear that δ_{IC} will become independent of X_0. Therefore we expect the behavior shown in Fig. 8. In the limit as X_0 becomes small we expect $\delta_{IC} = X_0 f$ and as $X_0 \rightarrow \infty$ we expect δ_{IC} to be equal to a limiting value δ'_{IC}. Both f and δ'_{IC} will be determined by the nature of the secondary

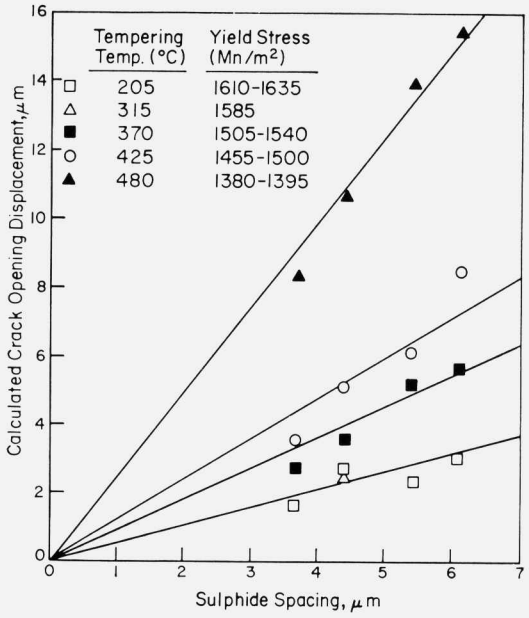

FIGURE 7. A plot of δ_{IC} as a function of X_0, the sulfide spacing, for 4340 steel tempered at different temperatures (from ref. 8 and ref. 10).

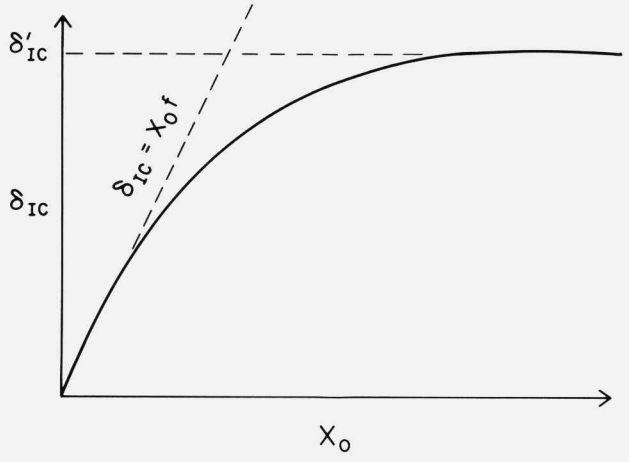

FIGURE 8. A plot of our expectations of the influence of the primary particle spacing, X_o, on δ_{IC} for a given dispersion of secondary particles and fine scale microstructure in the absence of strong bonding between the matrix and the primary particles.

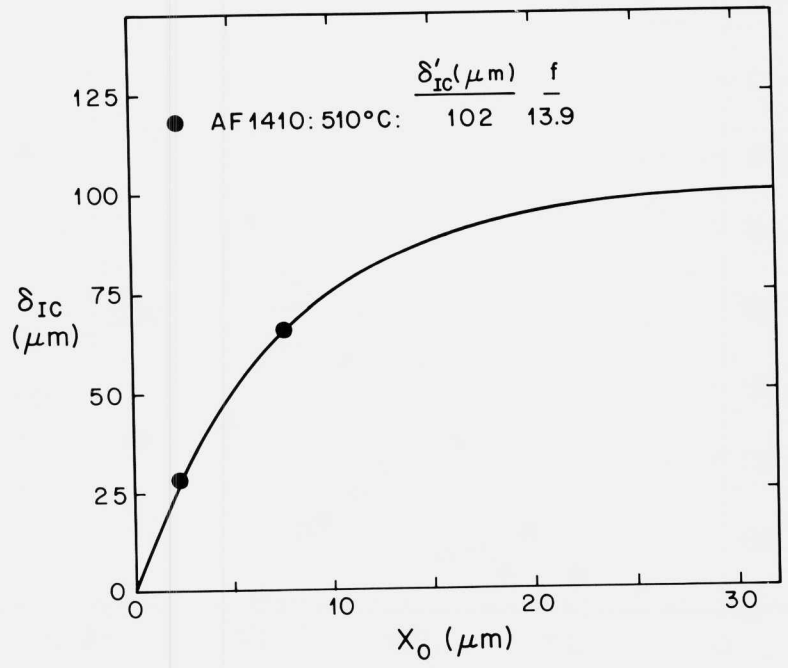

FIGURE 9. A plot of δ_{IC} as a function of X_o for the steel AF1410 tempered at 510°C where equation 5 has been used.

particles and fine scale microstructure. The expected behavior can be represented by the expression

$$\delta_{IC} = \delta'_{IC} - \delta'_{IC} exp\left(-X_0 f/\delta'_{IC}\right) \qquad [5]$$

Now, there is no fundamental rationale for this expression; it summarizes as simply as possible the expected form of the dependence of δ_{IC} on X_0. However, if this simple expression can be justified either theoretically or experimentally it would appear to have some practical consequences. The parameters f and δ'_{IC} can be determined by measuring δ_{IC} for two inclusion spacings. Having done this, it is possible to predict what inclusion spacing is required to achieve a δ_{IC} which is within a certain fraction of δ'_{IC}.

We have suggested this procedure because we are clearly beginning to examine alloys in which δ_{IC} is no longer linear in X_0. The curve for δ_{IC} *vs* X_0 for the steel AF1410 aged at 510°C is shown in Fig. 9. It is seen that at a spacing of 7.6μm, δ_{IC} is no

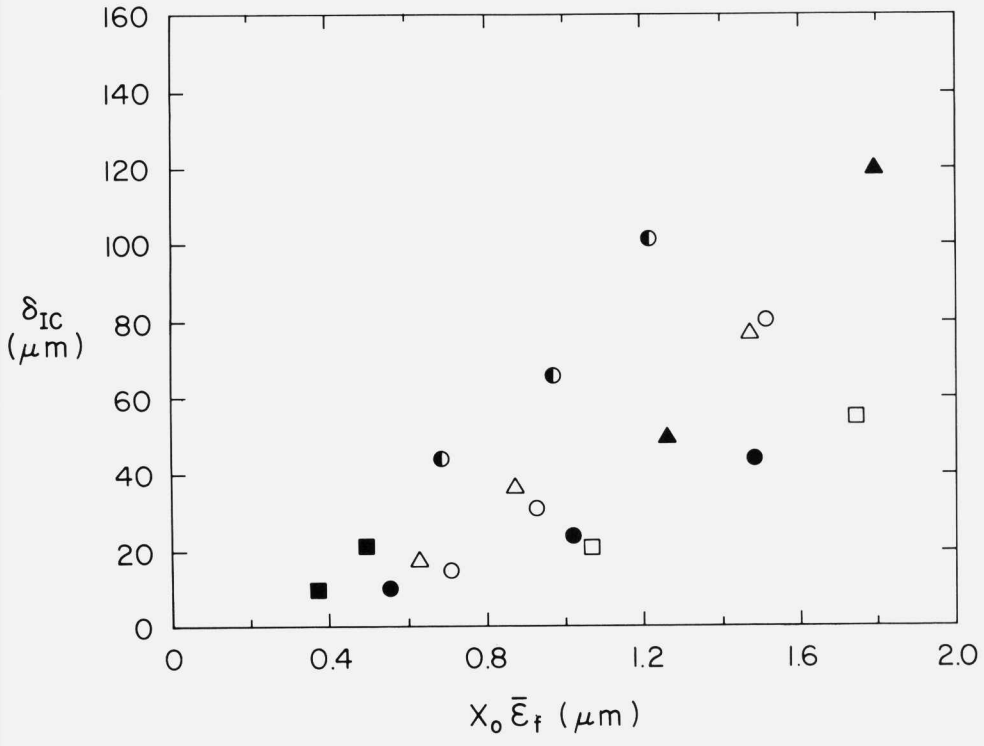

FIGURE 10. A plot of δ_{IC} as a function of $X_o \bar{\epsilon}_f$ where $\bar{\epsilon}_f$ is the effective plane strain tensile ductility.

longer linear in X_0 for this microstructure. In addition, it appears that to get very close to δ'_{IC} a spacing of X_0 = 20μm will be sufficient.

Pursuing this approach the problem is, what determines f and δ'_{IC}. While we have insufficient data to examine δ'_{IC} we can make a statement about f. From Fig. 7 we might expect f to scale as some measure of ductility. We have examined the possibility of using the plane strain tensile ductility. One reason for using this measure of ductility is that it represents plane strain conditions. In addition it does not seem to be very sensitive to the inclusion volume fraction, at least at high strength levels (20). Moreover, as shown by comparing the data for AF1410 in Table 4, it does not seem to be influenced by inclusion spacing. In addition, it is sensitive to the fine scale microstructure, as shown in Table 4. Finally it

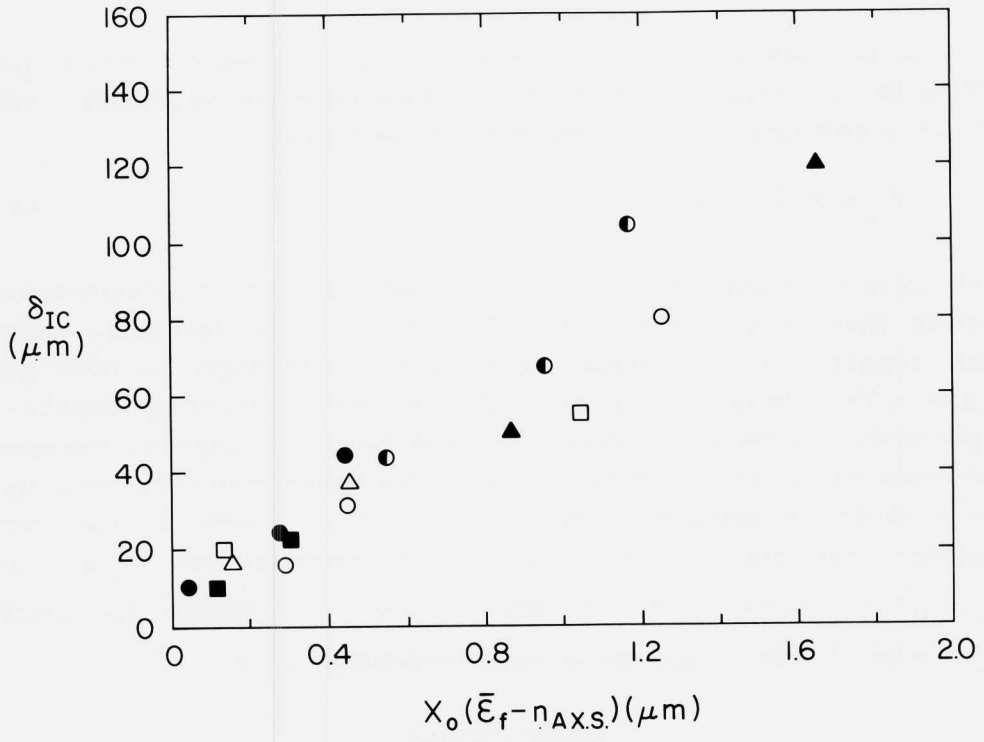

FIGURE 11. δ_{IC} plotted as a function of $X_o(\bar{\epsilon}_f - n)$ for several ultra high strength steels.

appears very sensitive to the nature of the secondary particles inherited from the austenitizing temperature; this is suggested by comparing the plane strain tensile ductilities of the HP9-4-20 steels in Table 8. In the correlations to be presented we have taken d_n to be 0.5; this is because our sectioning experiments suggest using Shih's (2) values of d_n for materials blunting to vertices over estimates δ_{IC}. In addition, where the average size of the inclusions on the fracture surface differ from the bulk, X_0 has been estimated using R_0 as determined from the fracture surface.

If we take f $\approx$ $\bar{\epsilon}_f$; there should be a correlation between δ_{IC} and $X_0\bar{\epsilon}_f$. We would not expect a perfect correlation because many of the microstructures studied are at levels of toughness where δ_{IC} is no longer quite linear in X_0. However, there is a very poor

correlation between δ_{IC} and $X_0\bar{\epsilon}_f$ as shown in Fig. 10.

A problem with this correlation is that $\bar{\epsilon}_f$ does not reflect the influence of blunting behavior on fracture initiation toughness. We obtain a somewhat better correlation if we write

$$\delta_{IC} \approx X_0(\bar{\epsilon}_f - n). \qquad [6]$$

The value of n used is that obtained from the smooth axisymmetric tensile specimens. As shown in Fig. 11 the fit is reasonably good. This suggests that for these materials f is dependent on both the plane strain tensile ductility and the work hardening capacity. Apparently we need to include the work hardening capacity because the blunting behavior changes, at least for these materials, with the work hardening exponent. We note that this expression does not suggest that previous work (21) which demonstrated $\delta_{IC} \approx n$ or $\delta_{IC} \approx n^2$ is incorrect. But it does suggest for materials for which $\delta_{IC} \approx n$ or n^2 that $\bar{\epsilon}_f$ will be strongly dependent on n.

CONCLUSIONS

First it is clear that a useful approach to improving the fracture initiation toughness of ultra strength steels is to maximize the inclusion spacing. This can be done by making the particles as large as possible and/or by minimizing the inclusion volume fraction. However, it is noted that δ_{IC} can become nonlinear with respect to X_0 at readily achieved inclusion spacings.

Our results suggest, in accordance with earlier speculation, that blunting to vertices enhances the fracture toughness by reducing the strains and reducing the severity of the stress states ahead of the crack tip. Blunting to vertices appears to be associated with low work hardening.

While blunting to vertices is favored by low work hardening exponent in the materials we have examined, it is not suggested that low work hardening *per se* is required to achieve high toughness. What appears to be required is to maximize the difference between the plane strain tensile ductiiity and the work hardening exponent.

ACKNOWLEDGEMENTS

The authors gratefully acknowledge the financial support of Ellwood City Forge and the Army Research Office under contract DAAL03-86-K-0124. In addition the authors appreciate the donations of material by Teledyne Allvac and the specialty steel division of Cytemps.

REFERENCES

1. J.A. Begley and J.D. Landes, in Fracture Toughness, ASTM STP 514, American Society for Testing and Materials, Philadelphia, PA, 1974, 201.

2. C.F. Shih, J. Mech. Phys. Solids, 1981, **29**, 305.

3. F.B. Pickering, "The Constitution of Non-metallic Inclusions in Steel", Paper No. 3 in Proceedings of Conference on Inclusions and Their Effects on Steel Properties, University of Leeds, 1974. Published by British Steel Corporation.

4. J.F. Knott, "Ductility, Toughness and Formability", Paper No. 8 in Proceedings of Conference on Inclusions and Their Effects on Steel Properties, University of Leeds, 1974. Published by British Steel Corporation.

5. J.R. Rice and M.A. Johnson, in Inelastic Behavior of Solids, M.F. Kanninen, W.G. Adler, A.R. Rosenfield and R.I. Jaffee, eds., McGraw-Hill, New York, 1970, p. 641.

6. J.R. Rice and D.M. Tracey, J. Mech. Phys. Solids, **17**, 1969, 201.

7. J.F. Knott, "Micromechanisms of Fibrous Crack Extension in Engineering Alloys", Conference Proceedings: Micromechanisms of Crack Extension Mechanics and Physics of Fracture 11, Cambridge, 1980, in Metal Science **14**, 1980, 327.

8. G.T. Hahn, M.F. Kanninen and A.R. Rosenfield, An. Rev. Mat. Sci. **2**, 1972, 381.

9. G.T. Hahn and A.R.Rosenfield, "Relationships Between Microstructure and the Fracture Toughness of Metals",

Proceedings of the Third International Conference on Fracture, Munich, April 8-13, 1973, Vol. **1**, Plenary Lectures, PLIII-211.

10. A.J. Birkle, R.P. Wei and G.E. Pellissier, Trans. ASM **59**, 1966, 981.

11. T.B. Cox and J.R. Low, Met. Trans. **5**, 1974, 1457.

12. R.H. Van Stone, T.B. Cox, J.R. Low and J.A. Psioda, Int. Metals Review **30**(4), 1985, 157.

13. W.M. Garrison, Jr., Metall. Trans. **17A**, 1986, 669.

14. D.A. Curry and P.L. Pratt, Mats. Sci. Eng., **37**, 1979, 223.

15. M. Ashby, Phil. Mag. **14**, 1966, 1157.

16. A.S. Argon and J. Im, Metall. Trans. **6A**(4), 1975, 839.

17. G.R. Speich, D.S. Dabkowski and L.F. Porter, Metall. Trans. **4**, 1973, 303.

18. W.M. Garrison, Jr. and N. Moody, Metall. Trans. 18A, 1987, 1257.

19. R.M. McMeeking, J. of Eng. Materials and Technology, Trans. ASME, Series H **99**, 1977, 290.

20. G.R. Speich and W.A. Spitzig, Metall. Trans. **13A**, 1982, 2239.

21. G.G. Garrett and J.K. Knott, Metall. Trans. **9A**, 1978, 1187.

THE DEVELOPMENT OF IMPROVED GUN STEELS

RAY HAWKINS
Royal Armament Research and Development Establishment,
Fort Halstead, Sevenoaks, Kent, England.

INTRODUCTION

In the UK gun steels are normally air melted in the basic electric arc furnace and cast, in air, into ingots for subsequent press forging. Traditionally medium carbon Ni Cr Mo steels have been used but the demand for higher working pressures subsequently led to the adoption of a 3¼ Ni Cr Mo V steel.

This method of manufacture proved satisfactory for steels heat treated to strength levels of 900MN/m^2. At these strength levels the steels had toughness levels more than adequate to provide the safety margins required by the gun designers. However, the gradual trend to higher working pressures has meant that, even using the existing steels at higher strength levels, safety margins are less than the designers have been traditionally accustomed. This situation was recognised in the early 1970's[1,2] when it was realised that future gun barrels would require greater attention to factors which affect failure by thermal and mechanical fatigue. In particular it was recognised that high fracture toughness and low fatigue crack growth rates at high proof stresses would be required. To achieve these properties would require improved steelmaking as well as efficient forging and heat treatment techniques. The reason for this was because the state of the art steelmaking was unable to consistently produce low sulphur, clean steels of the quality that would be required to ensure adequate low temperature toughness and acceptable fatigue lives at the higher strength levels. For example, at that time it was difficult to produce steels with sulphur levels much below 0.010%. This situation was to dramatically change in the late 1970's with the advent of ladle treatment techniques.

This paper describes the steps that have been taken to produce improved gun steels which may conveniently be discussed under three headings.

a. Improved steelmaking.
b. Optimisation of existing steels.
c. Development of alternative gun steels.

IMPROVED STEELMAKING

The recognition that improved steelmaking techniques would probably be needed to meet the increased working pressures of future gun designs, led the Ministry of Defence to evaluate the production of higher quality steels. At that time the competitive processes available for the production of clean, tough steels were vacuum arc remelting (VAR) and electroslag refining (ESR). The costs of the two processes, in terms of ingot steel, were comparable, although it was felt that an ESR plant could be more readily integrated into an existing plant to minimise capital costs. ESR offered the additional advantage that entrainment of slag did not occur. A programme of work was initiated to evaluate the properties of a range of barrels produced from ESR steel[1]. This programme of work culminated in the recommendation and adoption of ESR for the production of high pressure gun barrel designs. From that time ESR steel has been utilized in all experimental gun designs but it is only with the barrel for the Challenger tank that ESR has been specified in production.

ESR offers the capability of producing a product that has improved cleanness, soundness, uniformity of structure, homogeneity, ingot surface and higher manufacturing yields. The reduction in the size and frequency of inclusions gives greatly improved mechanical properties particularly in the transverse direction. The improved soundness, uniformity of structure and homogeneity enable the use of lower forging reductions. In fact, Wagner & Bar Avi (3) demonstrated that 81mm mortar barrels made from cast ESR steel not only met the mechanical property specification for forged gun tubes but withstood the explosive loading of firing. Our own work demonstrated that, although as cast ESR steel exhibited toughness levels comparable or superior to wrought air melt steel, the crack often followed dendritic boundaries, Figure 1a. It is clear that fracture along the dendritic boundaries is an easier fracture path than across the dendrites and, as a consequence, toughness appears to be sensitive to both orientation and structural coarseness in these cast structures, Figure 1b.

The reduction in the size and frequency of inclusions gives greatly improved mechanical properties especially in the transverse direction. This, coupled with the lower forging reductions required, gives a product with more isotropic properties than conventional air melt steel.

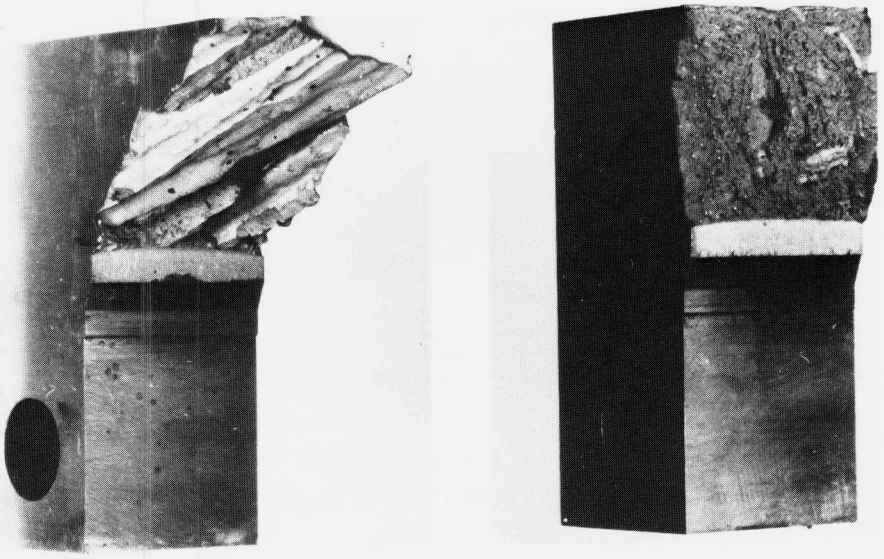

FIGURE 1. Typical fracture surfaces of K_{1c} test pieces of as cast ESR steel.
a Top of ingot.
b Bottom of ingot.

Practical Experience

A survey of results achieved on various development barrels revealed that the anticipated enhancement in properties was not always attained. Toughness levels were often no higher than those achieved with air melt or vacuum degassed steel, Figure 2.

In addition there were often large end to end variations in properties within a forging as well as large variations from forging to forging, Figure 3. Detailed metallurgical examination of sectioned forgings showed that much of the variation was associated with steel cleanness. Changes in sulphur had a particularly large effect, Figure 4. Where variations were associated with a build up in both sulphur and oxygen contents the end to end variations were even more pronounced, Figure 5.

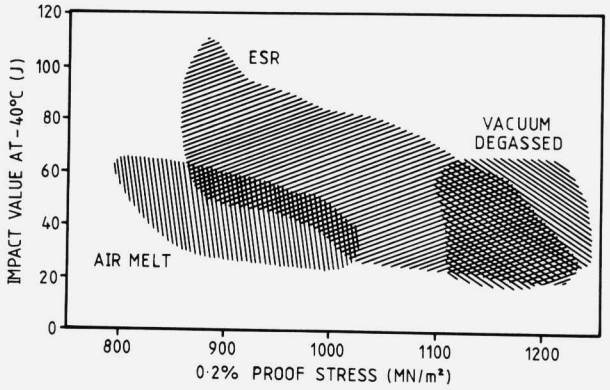

FIGURE 2. The variation of impact toughness with proof strength for ESR, air melt and vacuum degassed steels.

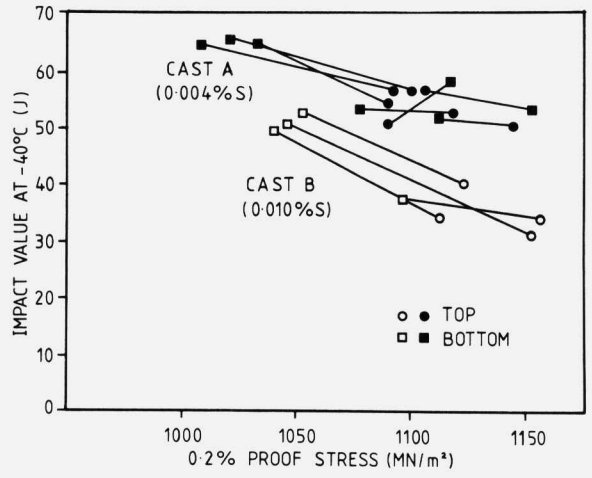

FIGURE 3. The variation of impact toughness with proof strength.

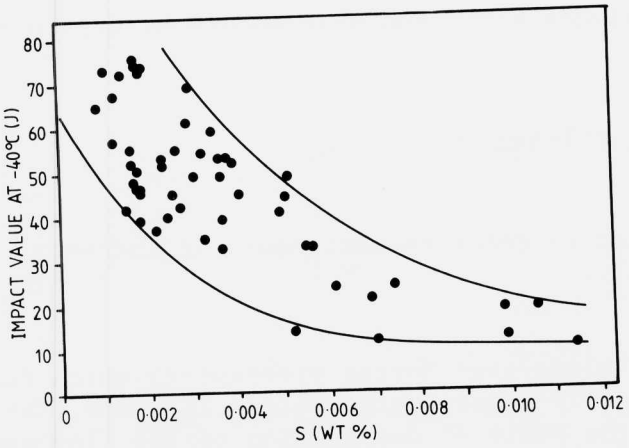

FIGURE 4. The variation of impact toughness with sulphur content.

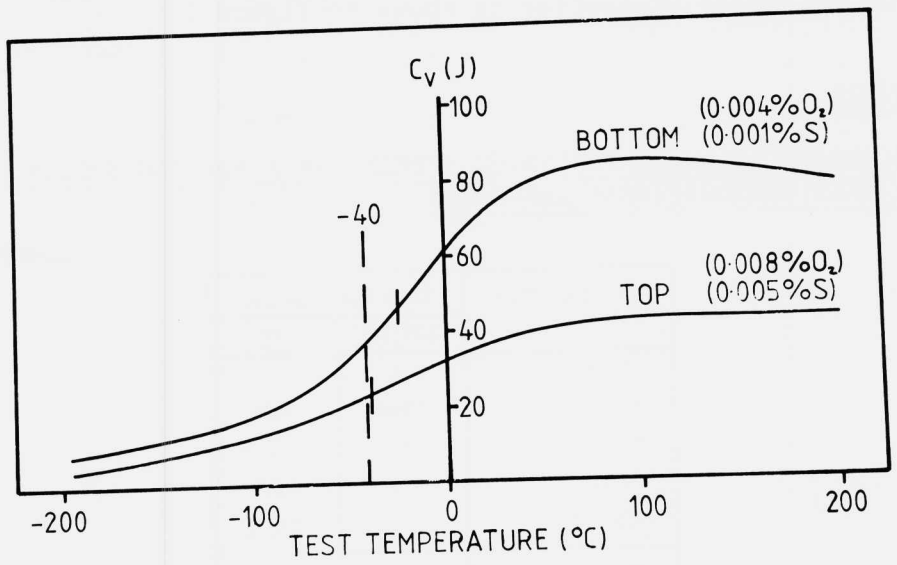

FIGURE 5. Impact transition curves for a forging showing a marked end to end compositional variation (see also Table 1).

All such build ups in sulphur and/or oxygen levels only occurred at the top end of the ESR ingots and were only observed with steel produced by the moving collar process. With this process a desulphurising slag containing 33% lime,

33% alumina and 33% fluorspar is used. The transfer of sulphur between metal and slag occurs by oxygen - sulphur exchange:

$$[S] + (O^{2-}) \rightleftharpoons (S^{2-}) + [O] \qquad (1)$$

where [] and () refer to components in the metal and slag respectively.

It is clear that during processing, which for a 4500kg ingot typically takes approximately 10 hours, there is a change in the state of deoxidation of the slag and a reduction in its desulphurising capacity. As a result of this there is a sulphur gradient up the ingot which was more marked when high, ≈0.012%, sulphur-containing electrodes were used. In severe cases there was also a considerable build up in oxygen levels, which gave rise to high volume fractions of nonmetallic inclusions, Table 1. The pronounced effect this had on impact properties is shown in Figure 5.

TABLE 1.

IDENTIFICATION OF INCLUSION SPECIES IN A FORGING SHOWING A MARKED COMPOSITIONAL VARIATION

INCLUSION TYPE	AREA FRACTION (%)	
	BOTTOM	TOP
Al rich	0·010	–
Si rich	0·004	0·006
Ca rich	0·002	–
MnFeS	0·001	0·010
AlSiMnSFe	–	0·031
TOTAL	0·016	0·047
SULPHUR (Wt%)	0·001	0·005
OXYGEN (Wt%)	0·004	0·008

Remedial Measures

The obvious solution to this problem is to monitor the state of deoxidation of the slag throughout processing and to adjust the slag composition as appropriate. However there are practical problems in this approach. Firstly the analysis of these complex slags is difficult and secondly additions to the molten slag during processing are normally avoided. Some remelters do make small additions of a deoxidant such as aluminium or calcium silicide during remelting but this has to be done with caution to prevent a build up in the deoxidant and entrainment in the remelt product.

The alternative approach, and the one that has been successfully adopted in the UK, is to produce high quality electrodes for remelting. Recent advances in electric arc technology, coupled with ladle treatment, now enable electrodes for remelting to be consistently and economically produced with low sulphur (<0.005%) and low oxygen levels. The use of such clean steel means that fewer impurities are introduced into the ESR process and hence it is easier to maintain the slag condition. Although the use of such steel for electrodes would be expected to be of benefit in both fixed and moving collar ESR processes, the greatest benefit has been observed with the moving collar process. Considerable improvements in impact toughness have been observed, Figure 6, and the results are comparable with those obtained with the fixed mould process which formerly gave a consistently higher quality product.

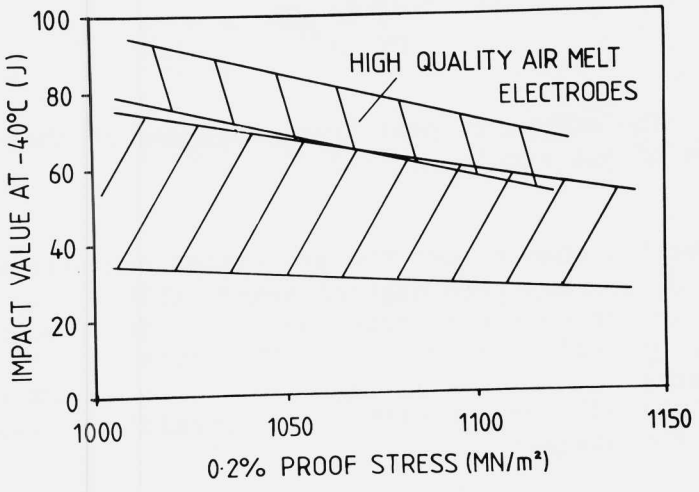

FIGURE 6. The enhancement of the mechanical properties of ESR steel through the use of high quality electrodes.

The use of high quality electrodes and high quality ESR ingots does not however guarantee that the forged product will exhibit good properties. Poor or incorrect heat treatment practices can undo all the good that the steelmaker has done! To achieve the best properties on heat treatment necessitates both good furnace temperature control and uniformity, together with rapid and efficient quenching practices. Poor temperature control or quenching practice can lead to marked property variations along the length of a gun barrel forging. An example of this is shown in Figure 7, where it may be seen that the muzzle end has a high toughness and fails in a ductile manner at -40°C. In contrast the breech end has a low toughness and fails in a brittle manner.

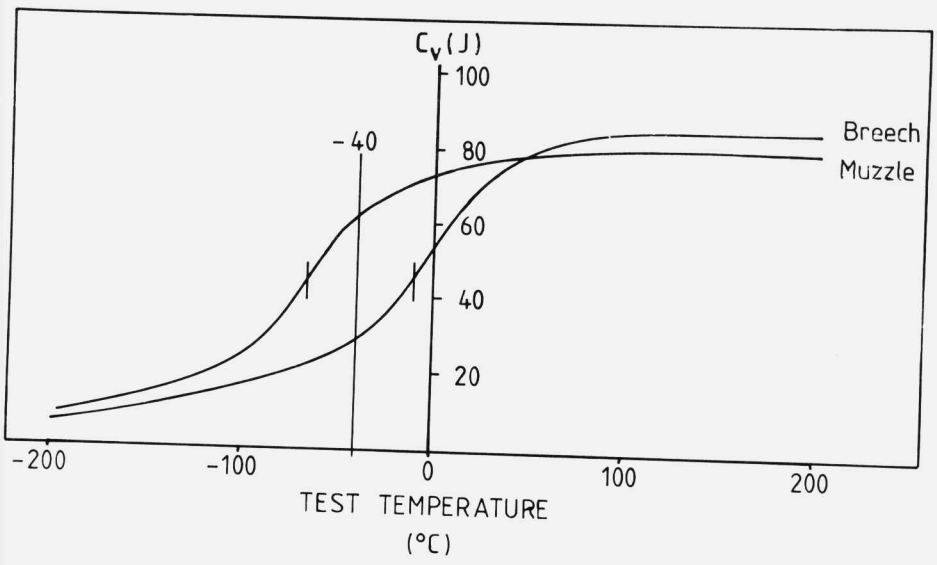

FIGURE 7. The effect of poor heat treatment on the impact properties of gun steel.

To further ensure that the properties achieved with ESR steel are of the expected high standard, it has been found necessary to increase the impact and ductility requirements over those specified for basic electric steel in the current UK specification. A typical requirement for an ESR steel is shown in Table 2 together with the properties previously specified for air melt steel.

TABLE 2.

SPECIFICATION REQUIREMENTS FOR AIR MELT AND ESR STEEL

		AIR MELT	ESR
PROOF STRENGTH	(MN/m^2)	1000 - 1150	1000 - 1150
ELONGATION	(%)	9 (min)	12 (min)
REDUCTION OF AREA	(%)	25 (min)	40 (min)
IMPACT STRENGTH AT -40°C	(J)	25 (min)	40 (min)

Alternative Steelmaking Processes

Figure 2 illustrated that although there was a large spread in results obtained with vacuum degassed steels, property levels comparable to ESR steel could be achieved. A more detailed analysis of the results again showed that a major cause of this variation was the sulphur content, Figure 8. It was found that only those steels containing $<0.003\%S$ gave toughness levels comparable with those obtained with ESR steel at similar strength levels.

Metallographic examination of the high sulphur steels revealed the presence of Type II manganese sulphide inclusions. These inclusions have a low melting point, solidify late in the solidification process in the last regions of liquid to solidify and hence are found at the primary grain boundaries forming in a dendritic, eutectic pattern. In addition the inclusions are very plastic at the normal hot rolling/forging temperatures and readily deform to produce coplanar ribbons. The formation of these coplanar ribbons leads to extremely low transverse toughness levels. Figure 9 illustrates this type of inclusion observed on the fracture surface of a sample exhibiting a low transverse toughness.

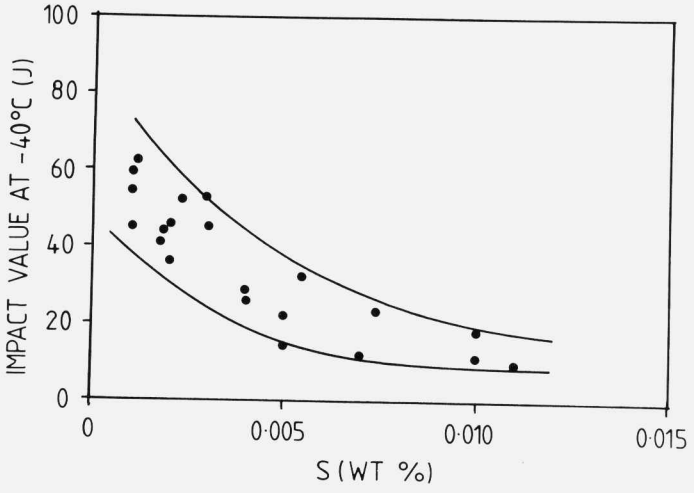

FIGURE 8. The variation of impact toughness with sulphur content for vacuum degassed steel.

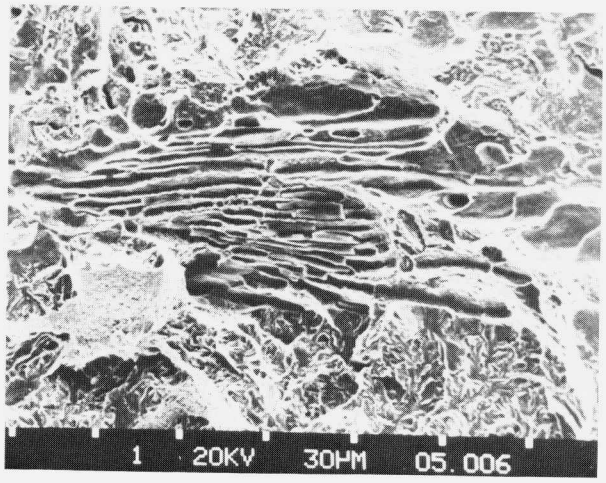

FIGURE 9. Type II manganese sulphide inclusions on fracture surface of impact test piece from a high sulphur, vacuum degassed steel.

For optimum properties from vacuum degassed steel it is essential to use low sulphur levels to prevent the formation of Type II manganese sulphide inclusions. Modern electric arc technology coupled with ladle treatment can now consistently and economically produce steels with $< 0.005\%$S, 0.001 and 0.002% being typical commercial levels for such steels.